

Spring 2022 – Systems Biology of Reproduction
Discussion Outline – Fertilization & Implantation Systems
Michael K. Skinner – Biol 475/575
CUE 418, 10:35-11:50 am, Tuesday & Thursday
April 14, 2022
Week 14

Fertilization & Implantation Systems

Primary Papers:

1. Teperek, et al. (2016) Genome Research 26:1034.
2. Stenhouse, et al. (2022) Recent Advances in Animal Nutrition and Metabolism, Adv Exp Med Biol 1354 :25-48.
3. Vento-Tormo, et al. (2018) Nature 563(7731):347-353.

Discussion

Student 6: Reference 1 above

- What was the experimental design and objectives?
- What impact on the developing embryo was observed?
- Can sperm epigenetic alterations modify the embryo?

Student 7: Reference 2 above

- How do embryos interact with endometrial cells?
- What factors were observed?
- How does implantation and placentation vary between humans, rodents, sheep and pigs?

Student 8: Reference 3 above

- What was the experimental design and technology?
- What maternal-fetal interface interactions were identified?
- What new insights for maternal-fetal interface were found to be critical for placentation and reproductive success?

Sperm is epigenetically programmed to regulate gene transcription in embryos

Marta Teperek,^{1,2,6} Angela Simeone,^{1,2,6} Vincent Gaggioli,^{1,2} Kei Miyamoto,^{1,2} George E. Allen,¹ Serap Erkek,^{3,4,7} Taejoon Kwon,⁵ Edward M. Marcotte,⁵ Philip Zegerman,^{1,2} Charles R. Bradshaw,¹ Antoine H.F.M. Peters,^{3,4} John B. Gurdon,^{1,2} and Jerome Jullien^{1,2}

¹Wellcome Trust/Cancer Research UK Gurdon Institute, University of Cambridge, Cambridge, CB2 1QN, United Kingdom;

²Department of Zoology, University of Cambridge, Cambridge, CB2 3EJ, United Kingdom; ³Friedrich Miescher Institute for Biomedical Research, 4058 Basel, Switzerland; ⁴Faculty of Sciences, University of Basel, 4001 Basel, Switzerland; ⁵Department of Molecular Bioscience, Center for Systems and Synthetic Biology, Institute for Cellular and Molecular Biology, The University of Texas at Austin, Austin, Texas 78712, USA

For a long time, it has been assumed that the only role of sperm at fertilization is to introduce the male genome into the egg. Recently, ideas have emerged that the epigenetic state of the sperm nucleus could influence transcription in the embryo. However, conflicting reports have challenged the existence of epigenetic marks on sperm genes, and there are no functional tests supporting the role of sperm epigenetic marking on embryonic gene expression. Here, we show that sperm is epigenetically programmed to regulate embryonic gene expression. By comparing the development of sperm- and spermatid-derived frog embryos, we show that the programming of sperm for successful development relates to its ability to regulate transcription of a set of developmentally important genes. During spermatid maturation into sperm, these genes lose H3K4me2/3 and retain H3K27me3 marks. Experimental removal of these epigenetic marks at fertilization de-regulates gene expression in the resulting embryos in a paternal chromatin-dependent manner. This demonstrates that epigenetic instructions delivered by the sperm at fertilization are required for correct regulation of gene expression in the future embryos. The epigenetic mechanisms of developmental programming revealed here are likely to relate to the mechanisms involved in transgenerational transmission of acquired traits. Understanding how parental experience can influence development of the progeny has broad potential for improving human health.

[Supplemental material is available for this article.]

Embryos obtained by fertilization develop to adulthood more frequently than those obtained by other methods, such as nuclear transfer (Gurdon et al. 1958; Kimura and Yanagimachi 1995), suggesting that sperm is specially programmed to support normal embryonic development. Several hypotheses were proposed to explain the nature of this programming, including the idea that sperm is programmed for efficient replication after fertilization (Lemaitre et al. 2005) or for supporting proper embryonic transcription (Suzuki et al. 2007; Hammoud et al. 2009; Zheng et al. 2012). The latter hypothesis was proposed following the observation that promoters of developmentally important genes escape global replacement of histones by protamines in mature sperm. In fact, these promoters retain post-translationally modified histones, suggesting that epigenetic marks on sperm chromatin may be transmitted to the embryo at fertilization and could subsequently pattern transcription of embryonic genes (Suzuki et al. 2007; Hammoud et al. 2009; Brykczynska et al. 2010; Wu et al. 2011; Paradowska et al. 2012; Zheng et al. 2012; Ihara et al. 2014; Siklenka et al. 2015). However, the validity of this hypothesis was recently questioned (Carone et al. 2014; Samans et al. 2014).

In this work, we compared the developmental potential of sperm to that of spermatids in order to understand the nature of sperm programming for development in *Xenopus laevis*. The use of spermatids, immediate precursors of sperm, suits such comparisons because (1) spermatids have completed meiosis and have the same DNA content as sperm, and (2) spermatid chromatin structure resembles that of somatic cells (Gaucher et al. 2010). Furthermore, in the mouse, embryos derived from injection of spermatids into unfertilized oocytes develop to adulthood less frequently than embryos derived from injection of sperm, suggesting that developmentally important information is acquired during spermatid to sperm maturation (Kimura and Yanagimachi 1995; Kishigami et al. 2004). Here, we demonstrate that sperm is epigenetically programmed to regulate transcription of several developmentally important embryonic genes.

Results

Sperm-derived embryos develop better than spermatid-derived embryos

We first compared the development of embryos obtained by transplanting somatic cell nuclei (SCNT) with the development of sperm-derived embryos. To minimize the experimental difference

⁶These authors contributed equally to this work.

⁷Present address: EMBL Heidelberg, 69117 Heidelberg, Germany
Corresponding authors: j.jullien@cam.ac.uk, mt446@cam.ac.uk

Article published online before print. Article, supplemental material, and publication date are at <http://www.genome.org/cgi/doi/10.1101/gr.201541.115>. Freely available online through the *Genome Research* Open Access option.

© 2016 Teperek et al. This article, published in *Genome Research*, is available under a Creative Commons License (Attribution 4.0 International), as described at <http://creativecommons.org/licenses/by/4.0/>.

in the way the embryos were generated, both types of embryos were generated by nuclear injection: cloned embryos were obtained by transplanting nuclei of embryonic cells to enucleated eggs (Fig. 1A), and sperm-derived embryos were produced by intra-cytoplasmic injection of sperm (ICSI) to eggs (Fig. 1C). We observed that cloned embryos developed less efficiently to the swimming tadpole stage than sperm-derived embryos (Fig. 1B). This illustrates the better developmental potential of sperm over that of a somatic cell. In this experimental set-up, however, the way the embryos are generated is quite different: the maternal genome is present in sperm-derived embryos, whereas it has been removed in the SCNT embryos. In order to better assess the developmental potential of sperm, we aimed to compare embryos produced in the same way. For that purpose, we generated embryos by injecting permeabilized purified sperm or spermatids (Supplemental Fig. S1) to the cytoplasm of unfertilized eggs (ICSI) (Fig. 1C). In that way, both types of embryos are obtained in the same manner, and their development can be compared. The two types of embryos reached the gastrula stage with a similar frequency. However, sperm-derived embryos developed significantly better to the swimming tadpole stage than spermatid-derived ones (P -value < 0.05) (Fig. 1D,E). This is in agreement with observations made previously in mouse (Kimura and Yanagimachi 1995; Kishigami et al. 2004). Spermatid-derived embryos and cloned embryos exhibit a similar reduction in developmental potential when compared to sperm-derived embryos (Fig. 1B–E), suggesting that the spermatid is as severely impaired to support development as a somatic cell.

In conclusion, embryos can be generated in the same way from sperm or spermatids, and spermatids show reduced developmental potential compared to sperm. Therefore, the comparison of sperm and spermatids was subsequently used to investigate why sperm support better development than other cell types.

Spermatids replicate their DNA as efficiently as sperm

Since it has been shown that sperm, as opposed to other cells, replicate DNA more efficiently (Lemaitre et al. 2005), we hypothesized that the poor embryonic development of spermatid-derived embryos is due to inefficient DNA replication. Egg extracts from *Xenopus* have been widely used to investigate mechanisms of replication (Hutchison et al. 1989; Lemaitre et al. 2001). By incubating nuclei in egg extracts, one can mimic replication events that occur prior to the first embryonic cell division. We measured DNA replication efficiency in sperm and spermatids incubated in egg extracts (Hutchison et al. 1989) by molecular combing analysis (Gaggioli et al. 2013). In this assay, the egg extract is supplemented with modified nucleotide precursors that will be incorporated into replicating DNA (Fig. 2A). Following replication, DNA is stretched on a slide, and both the total (green) and replicated (red) DNA fibers are fluorescently labeled (Fig. 2B). By measuring the extent of replication on several hundreds of DNA fibers, we observed equally efficient DNA replication in both sperm and spermatids (Fig. 2C). We concluded from this analysis that the nature of sperm programming is not related to replication. We then tested whether spermatid-derived embryos are capable of correctly initiating embryonic transcription.

Haploid sperm-derived embryos develop better than haploid spermatid-derived embryos

To rigorously assess the developmental potential and transcriptional ability of sperm and spermatids, and to eliminate the risk

of any potential interference from the maternal nucleus, we used haploid, paternally derived embryos generated by injection of permeabilized sperm or spermatids into enucleated eggs (Fig. 3A; Supplemental Fig. S2; Narbonne et al. 2011). We first confirmed that haploid, sperm-derived embryos developed significantly better to the swimming tadpole stage than haploid, spermatid-derived embryos (P -value < 0.05) (Fig. 3B), recapitulating the results from diploid embryos (Fig. 1E). Previous mammalian experiments comparing developmental potential of sperm and spermatids used diploid biparental embryos (Kimura and Yanagimachi 1995; Kishigami et al. 2004). Our results with paternal haploid embryos directly demonstrate that the sperm nucleus supports better development than the spermatid nucleus, with or without the maternal genome. Furthermore, this experimental set-up allows a specific assessment of transcription originating exclusively from sperm- or spermatid-derived chromatin at the time of embryonic gene activation.

Developmentally important genes are misregulated in spermatid-derived embryos

Since experiments in the mouse suggested that sperm might be better than other cell types at supporting mRNA transcription (Ziyyat and Lefevre 2001; Vassena et al. 2007; Ihara et al. 2014), we tested this hypothesis using haploid, sperm- and spermatid-derived embryos. Embryos were rigorously staged (see Supplemental Experimental Procedures) and collected at gastrulation, before the onset of developmental defects. Gene expression was then analyzed by RNA-seq, using a set of 34,373 transcripts (provided as Supplemental Gene Annotation). Out of 18,340 expressed genes, 255 were differentially expressed in spermatid-derived embryos compared to sperm-derived embryos (FDR < 0.05) (Supplemental Table S1). One hundred of these transcripts showed consistent changes in at least six out of seven experiments, and we will refer to them as “misregulated” (Fig. 3C; Supplemental Table S1). The majority (82/100) were up-regulated in spermatid-derived embryos, and they include transcriptional regulators (e.g., *gata2*, *gata3*, *hes1*, and *fos*) as well as morphogens (e.g., *bmp2*, *bmp7*, or *dhh*) essential for embryonic development. Accordingly, gene enrichment analysis revealed that several development-related terms were significantly enriched in the list of misregulated genes (P -value < 0.05) (Fig. 3D).

The fact that most of the misregulated genes were up-regulated in spermatid-derived embryos raised the possibility that these genes were actively transcribed in spermatids and continued to be transcribed in embryos. Indeed, the spermatid, as opposed to the sperm, is a transcriptionally active cell, and this difference might explain why genes are up-regulated in embryos originating from spermatids rather than sperm. To test this possibility, we compared the expression level of genes in spermatids and in spermatid-derived embryos. We did not observe any correlation between the expression of misregulated genes in spermatid-derived embryos and their expression in spermatids ($r = -0.17$, P -value < 0.05) (Fig. 3E). This suggests that the up-regulation of these genes in spermatid-derived embryos is not the result of transcript carry-over (or ongoing transcription) from spermatid chromatin. Because permeabilized spermatids used to generate embryos are likely to contain additional RNAs, we performed an additional control for the potential effect of spermatid-derived RNAs on embryonic development. We purified total RNA from testis and injected a quantity corresponding to the amount found in one spermatid (50 pg) to embryos generated with sperm. TRIzol was

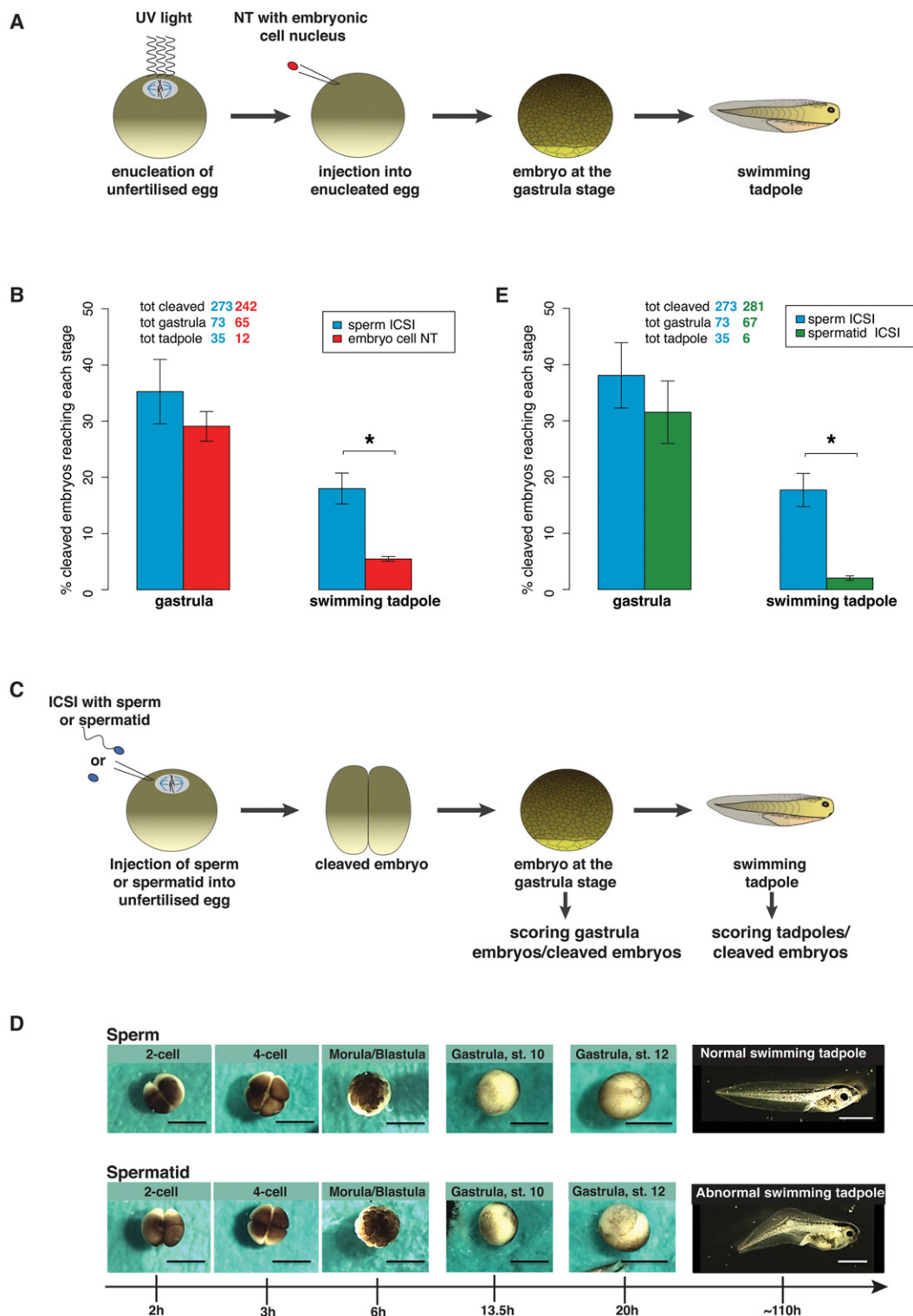


Figure 1. *Xenopus* sperm is better at supporting development than a spermatid or a somatic cell. (A) Experimental design for the generation of cloned embryos. The somatic nucleus of a gastrula cell is transplanted to a UV-enucleated egg. The resulting embryos are scored at the gastrulation and tadpole stage. (B) Scoring of embryos as % of gastrulae and as % of swimming tadpoles to the total number of cleaved embryos. Average of $n = 6$ independent experiments (sperm ICSI), and $n = 3$ independent experiments (embryo cell NT). The total number of embryos analyzed is shown above the graph. Error bars: SEM. (*) P -value < 0.05 (χ^2 test). (C) Experimental design for the generation of sperm- and spermatid-derived embryos. Permeabilized sperm or spermatids are injected to the cytoplasm (ICSI) of an unfertilized egg. The resulting embryos are scored at the gastrulation and tadpole stage. (D) Representative images of sperm- and spermatid-embryos. Scale bars = 1 mm. (E) Scoring of embryos as % of gastrula and as % of swimming tadpoles to the total number of cleaved embryos (average of $n = 6$ independent experiments). The total number of embryos analyzed is shown above the graph. Error bars: SEM. (*) P -value < 0.05 (χ^2 test).

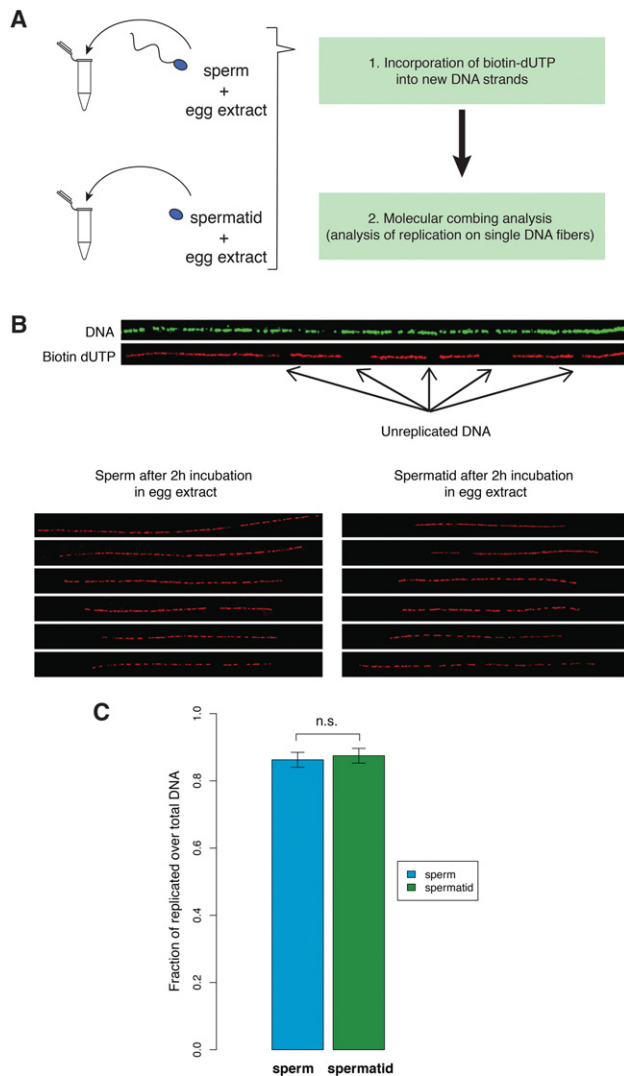


Figure 2. Spermatids are as good as sperm at DNA replication. (A) Sperm and spermatids are separately incubated with egg extracts supplemented with biotin-dUTP. Subsequently, DNA fibers are isolated and subjected to molecular combing, which reveals replication on single DNA fibers. (B) Examples of DNA fibers after immunostaining procedure. Antibody staining against DNA reveals the total length of the fiber (green) and antibody staining against biotin reveals the replicated DNA (red). The *bottom* panels show representative examples of replication staining from sperm and from spermatids incubated in egg extracts. (C) Replication extent measured as the proportion of DNA that incorporated biotin-dUTP to the total fiber length. Results are from at least 125 independent DNA fibers (22,000 kb of DNA for each sample). Error bars: SEM. Samples were not significantly different (P -value = 0.41, KS-test).

used to isolate RNA as it allows the recovery of RNA in a broad range of sizes (El-Khourey et al. 2016). All embryos generated in that way developed normally, indicating that testicular RNAs are not detrimental to embryonic development (Supplemental Fig. S3). Lastly, we have verified that the synthesis of rRNAs is not affected in spermatid-derived embryos. Indeed, in mouse, defect in rRNA synthesis has been proposed to explain the developmental defect of nuclear transfer embryos (Suzuki et al. 2007; Zheng et al. 2012) and could explain the difference in the bulk of RNA synthesis observed between sperm- and spermatid-derived embryos (Bui et al. 2011). We observed that newly synthesized 18S and

28S rRNAs are equally well produced in sperm- and spermatid-derived embryos (Supplemental Fig. S4).

We conclude that the developmental failure of spermatid-derived embryos is not associated with carried over spermatid RNAs or with defects in rRNA expression. Rather, we observe a correlation between developmental defects and misexpression of a set of developmentally important genes in spermatid-derived embryos. We hypothesized that differences in gene expression between sperm- and spermatid-derived embryos might result from epigenetic differences of sperm/spermatid chromatin.

Epigenetic differences between sperm and spermatid chromatin

To investigate potential links between the epigenetic marking of paternal chromatin and embryonic gene expression, we carried out epigenetic profiling of mononucleosomal chromatin from sperm and spermatid using an extensive MNase digestion protocol applied by others to probe for histones stably associated with chromatin in mature sperm in mouse and human (Supplemental Tables S2, S3; Supplemental Fig. S5; Hammoud et al. 2009; Brykczynska et al. 2010). In *Xenopus*, the transition from spermatid to sperm is characterized by histone H3 and H4 retention and partial loss of H2A and H2B (Risley and Eckhardt 1981). We first compared nucleosome occupancy profiles in sperm and spermatids. Similarly to what was observed in other vertebrates (Hammoud et al. 2009; Brykczynska et al. 2010), we observed higher nucleosomal occupancy (MNase-seq) (Fig. 4A) around TSSs (transcriptional start sites) in sperm when compared to spermatids. In this context, the positioned nucleosomes show a similar distribution in sperm and spermatids (Supplemental Fig. S6). Secondly, we analyzed DNA methylation profiles in sperm and spermatids by MBD-seq. DNA methylation was higher around sperm TSSs than spermatid TSSs (Fig. 4B). These differences were observed at the genome-wide level between sperm and spermatids, as well as on the set of misregulated genes (Supplemental Figs. S6, S7). A lower level of nucleosome occupancy and DNA methylation in spermatids compared to sperm could therefore explain the up-regulation of genes in spermatid- compared to sperm-derived embryos.

To further characterize sperm and spermatid chromatin, we performed ChIP-seq analysis of histone marks associated with activation (H3K4me2, H3K4me3) or repression (H3K27me3, H3K9me3) of transcription. We looked for peaks (Fig. 4C; Supplemental Table S4) as well as for the overall methylation levels (Fig. 4D; Supplemental Fig. S8; Supplemental Table S5) around TSSs for each of these modifications. When compared to all genes, the set of misregulated genes was significantly enriched for H3K27me3 in both sperm and spermatids (Fig. 4C). However, since H3K27me3 was present in both sperm and spermatids, it suggests that this repressive mark alone cannot explain the difference in gene expression observed in sperm- and spermatid-derived embryos.

Interestingly, histone marks associated with active transcription (H3K4me2/3) showed an enrichment at promoters of misregulated genes in spermatids but not in sperm (Fig. 4C,D), providing a plausible explanation for the up-regulation of these genes in spermatid-derived embryos.

Coexistence of H3K4me2/3 and H3K27me3 in spermatids correlates with embryonic gene up-regulation

The epigenetic features analyzed (histone marks, DNA methylation, and nucleosome occupancy) can individually provide a

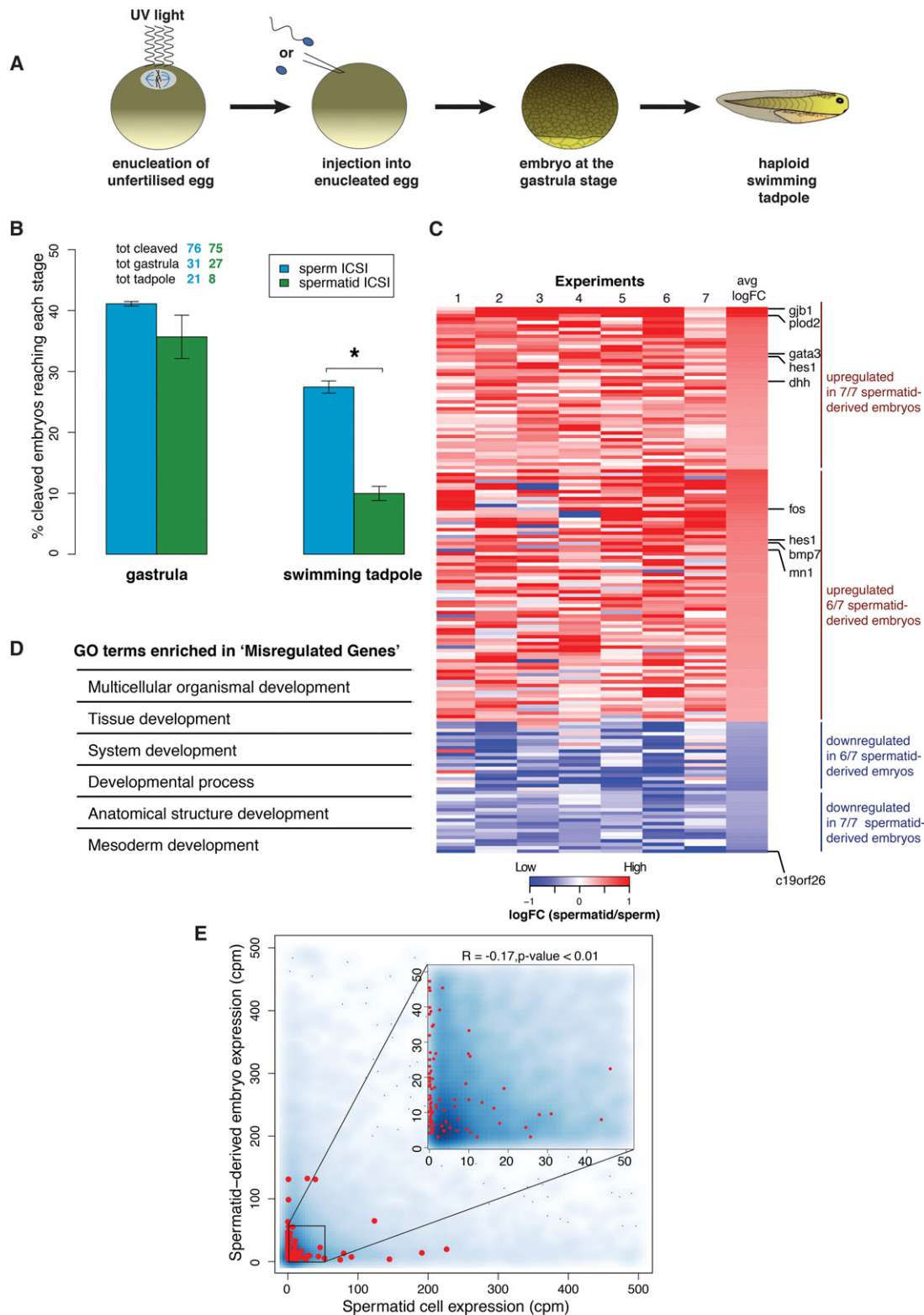


Figure 3. Transcription of developmentally important genes is misregulated in spermatid-derived embryos compared to sperm-derived embryos. (A) Schematic representation of paternally derived haploid embryos generated by UV enucleation of eggs followed by intra-cytoplasmic sperm injection (ICSI). (B) Developmental advantage of sperm over spermatid is maintained in haploid embryos. Embryos were scored as the % of embryos reaching a gastrula stage and a swimming tadpole stage to the total number of cleaved embryos (average of $n = 3$ independent experiments). Numbers of embryos analyzed are indicated above the bars. Error bars: SEM. (*) P -value < 0.05 (χ^2 test). (C) Genes important for development are misregulated (mostly up-regulated) in spermatid-derived embryos. Heat map representing log fold-change in expression levels of the 100 genes (rows) misregulated in spermatid versus sperm gastrula embryos (FDR < 0.05; red: up-regulated; blue: down-regulated in spermatid) across seven independent experiments (columns). (D) Developmentally important gene ontology terms enriched in the list of misregulated genes (P -value < 0.05). (E) Up-regulation of genes in spermatid-derived embryos does not correlate with their transcription in spermatid. Density scatter plot showing gene expression in spermatid-derived embryos versus that in spermatids. No correlation is observed between the two parameters for all genes ($r = 0.06$) as well as for the misregulated genes (red dots, $r = -0.17$).

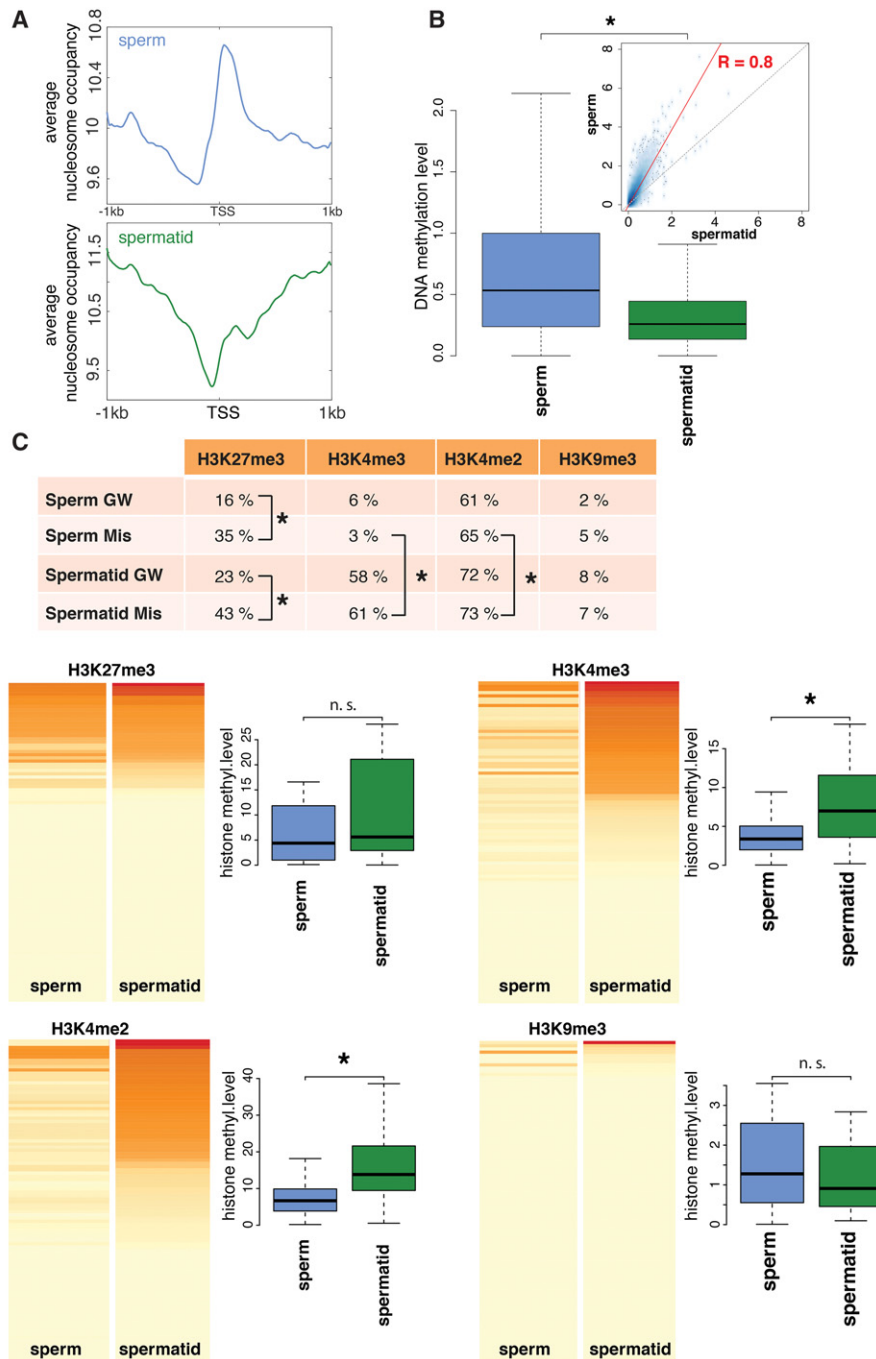


Figure 4. Genes that are misregulated in spermatid-derived embryos have different epigenetic features in sperm and spermatid. (A) Genome-wide average nucleosome occupancy at the TSS of sperm (blue) and spermatid (green) genes. (B) Boxplots showing genome-wide DNA methylation levels at the TSS \pm 1 kb of sperm (blue) and spermatid (green) genes. *Inset* shows correlation between the DNA methylation levels of sperm and spermatid ($R = 0.8$, P -value < 0.05); red line: regression; dotted line: diagonal. (C) Percentage of genes harboring H3K27me3, H3K4me3, H3K4me2, or H3K9me3 peaks genome-wide (GW) and at misregulated genes (Mis). (*) P -value < 0.05 (χ^2 test). (D) Heat maps representing H3K27me3, H3K4me3, H3K4me2, and H3K9me3 overall levels (see Supplemental Material and Supplemental Fig. S8) at misregulated genes in sperm (first column) and spermatid (second column). Each map is sorted according to the signal in spermatid. Boxplots show the distribution of methylation levels across misregulated genes. (*) P -value < 0.05 (KS-test) (Supplemental Table S7).

possible explanation for the observed differences in expression in sperm- and spermatid-derived embryos. However, complex interactions involving more than one epigenetic feature might better explain this differential embryonic gene expression. In or-

der to identify such interactions, we have performed a partial correlation analysis. In this analysis, all the measured parameters are assessed simultaneously to produce maps indicating the way epigenetic features associate with each other and with gene

expression. The aim of such analysis is to extract more general principles describing the paternal epigenetic program underlying gene expression and identify which epigenetic features are likely to have the strongest contribution to embryonic gene expression. We applied the partial correlation analysis to identify links between the measured epigenetic features in sperm and the expression of the misregulated genes in sperm-derived embryos (Fig. 5A), or between the measured epigenetic features in spermatid and their expression in spermatid-derived embryos (Fig. 5B). We observed that sperm H3K4me2/3 and embryonic gene expression were positively associated, whereas sperm H3K27me3, H3K9me3, and DNA methylation are negatively linked to embryonic gene expression (Fig. 5A). Interestingly, activating H3K4me2/3 and repressive H3K27me3 marks in spermatids were positively linked to gene expression in spermatid-derived embryos, and at the same time they were also strongly associated with each other (Fig. 5B). These associations were also observed when performing a similar analysis using an extended set of misregulated genes obtained by relaxing the selection parameters from $FDR \leq 0.05$ (255 genes) to $FDR \leq 0.4$ and $|\log FC| \geq 0.2$ (1116 genes). The use of this extended set increased the predictive power of the analysis and showed stronger links between the features tested within an overall similar network (Supplemental Fig. S9). Therefore, the difference between sperm- and spermatid-derived embryos is best explained by the fact that, in contrast to sperm, where H3K27me3 is overrepresented at genes differentially expressed in haploid embryos, in spermatids H3K27me3 coexists with H3K4me2/3 on these genes,

thereby contributing to their up-regulation in spermatid-derived embryos.

We checked whether the observed distribution of H3K4me2/3 and H3K27me3 on the misregulated genes of *Xenopus* sperm was a conserved feature across species. For that purpose, we investigated how these histone marks were distributed in human sperm (Hammoud et al. 2009) on human orthologs of the *Xenopus* misregulated genes. We observed that, similarly to *Xenopus* sperm, human sperm showed an enrichment for H3K27me3 on misregulated genes (Fig. 5C). Additionally, misregulated genes did not exhibit any enrichment over the genome-wide distribution for H3K4me2 in both species. This indicates a conservation of sperm epigenetic features on these genes in the two species.

We next tested if paternally derived H3K4me2/3 and H3K27me3 were indeed involved in patterning embryonic gene expression.

Paternal H3K4me2/3 and H3K27me3 influence embryonic gene expression

To test the function of epigenetic marks from sperm or spermatid chromatin on the regulation of embryonic transcription, we experimentally removed these marks in embryos (Fig. 6A; Supplemental Fig. S10). mRNAs encoding histone demethylases or control mRNAs were first injected into immature oocytes. After allowing 24 h for the enzymes to be expressed, the oocytes were in vitro-matured into eggs (IVM) and injected with sperm or spermatids

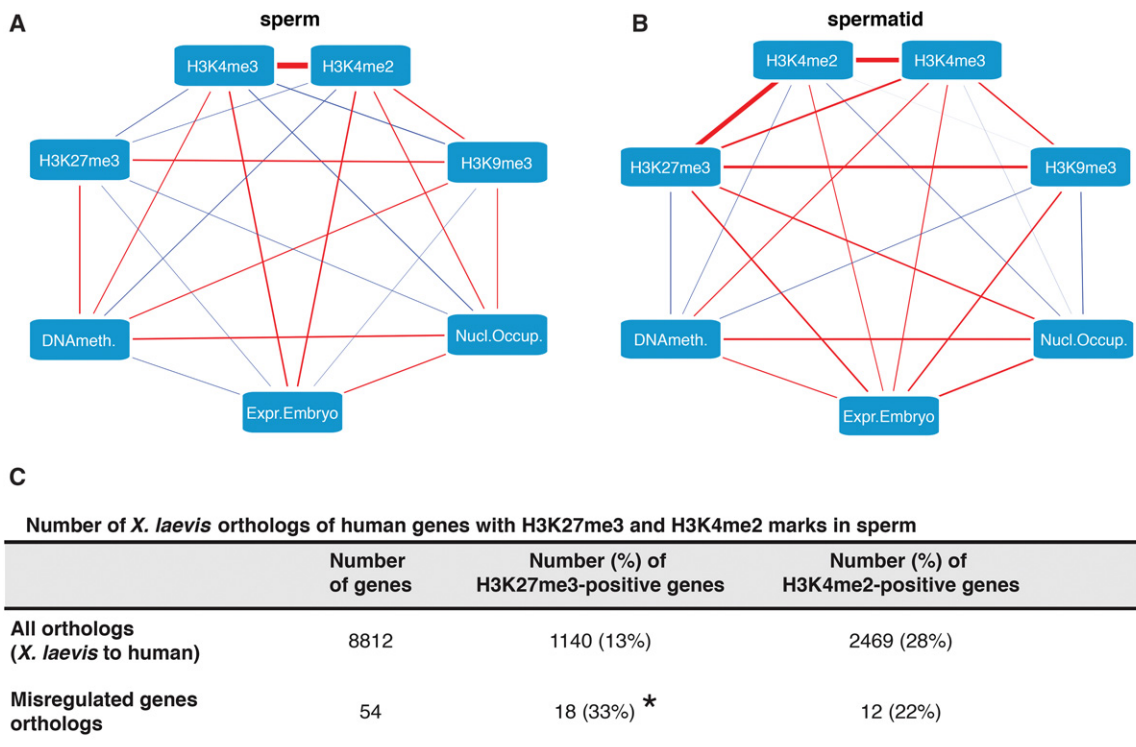


Figure 5. H3K27me3 target genes that lose H3K4me2/3 in sperm compared to spermatids are misregulated in spermatid-derived embryos. (A,B) Differential gene expression between sperm- and spermatid-derived embryos best correlates with differential H3K4me2/3 and H3K27me3 marking in sperm and spermatids. Partial correlation network between all tested epigenetic features of the paternal chromatin (A, sperm; B, spermatid) and gene expression in the corresponding embryos. Edges (lines) represent positive (red) or negative (blue) partial correlations. Edges thickness: strength of the partial correlations. (C) H3K4me2 and H3K27me3 marking on misregulated genes is conserved between *Xenopus* and human sperm. As compared to all orthologs, the misregulated orthologs are enriched for H3K27me3 marks over the genome-wide average in human sperm (χ^2 test, [*] P -value < 0.05). No statistical enrichment for H3K4me2 on misregulated genes as compared to the genome-wide average is observed in human sperm.

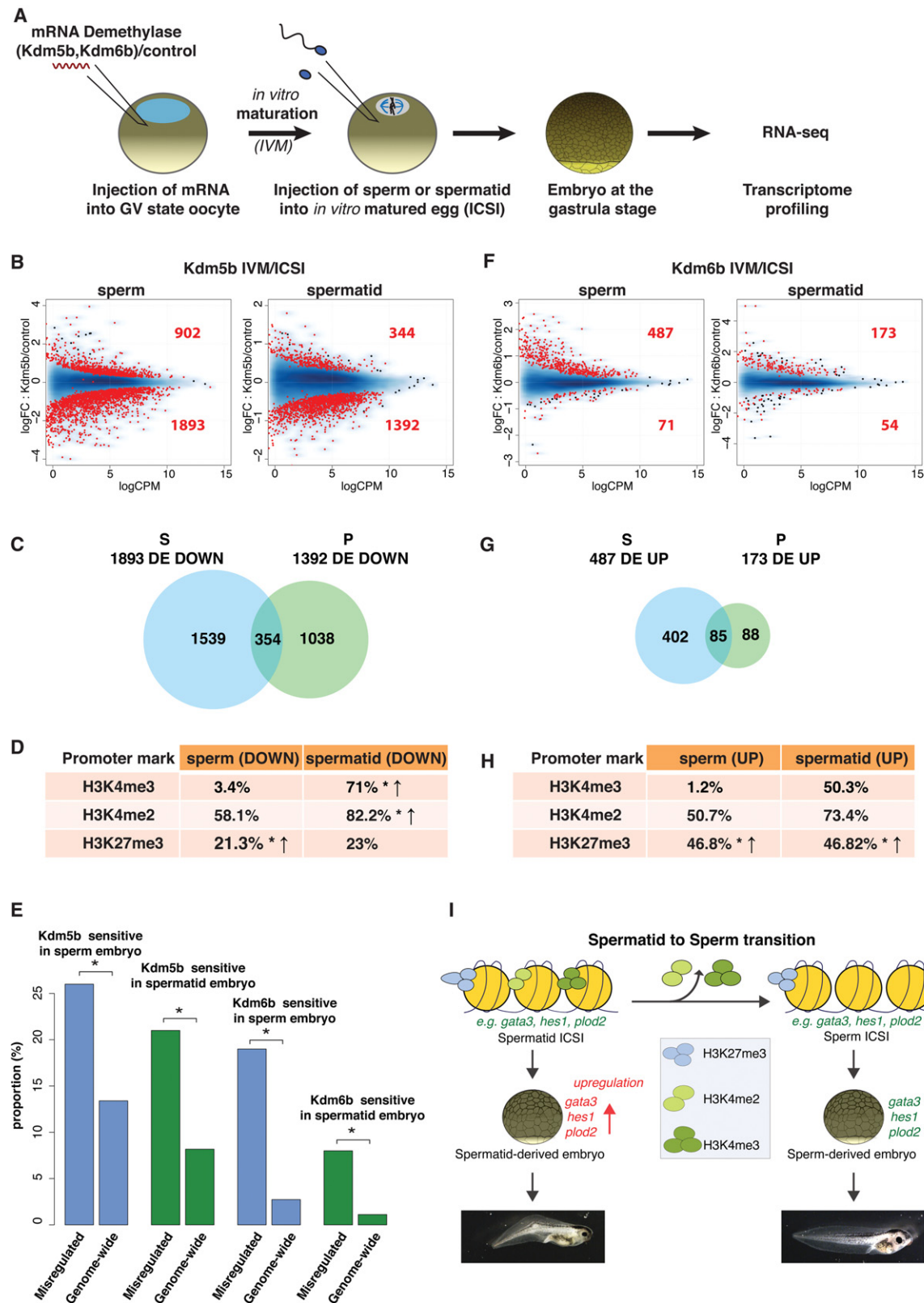


Figure 6. Paternal genome marking by H3K4me2/3 and H3K27me3 is required for gene expression in the embryos. (A) Histone demethylase expression assay. (B) MA plot showing log fold-change (logFC, y-axis) in gene expression between *Kdm5b* (H3K4me2/3 demethylase)- versus control mRNA-injected embryos, against log counts per million (logCPM, x-axis). Red dots: genes differentially expressed (FDR < 0.05); N = 4 independent experiments. (C) Venn diagram of down-regulated genes upon KDM5B expression in sperm- (blue) and spermatid-derived (green) embryos. (D) Percentages of genes down-regulated upon KDM5B expression in embryos that show H3K4me2/3 and H3K27me3 promoter peaks in the paternal cell. (*) *P*-value < 0.05 (χ^2 test); \uparrow : over-represented when compared to genome-wide distribution. (E) Proportion of misregulated genes affected in each demethylase expression assay. (*) *P*-value < 0.05 (χ^2 test). (F) Same as B for KDM6B (H3K27me3 demethylase) expression. (G) Same as C with genes up-regulated upon KDM6B expression. (H) Same as D for genes up-regulated upon KDM6B expression. (I) Model of epigenetic programming of sperm for the regulation of embryonic transcription.

(ICSI). The resulting embryos were collected at the gastrulation stage for RNA-seq analysis. In this protocol, histones from both maternal and paternal chromatin are demethylated when the embryo is generated. By comparing embryos produced with different paternal chromatin (sperm or spermatid), we can evaluate the effect of paternal epigenetic mark removal on embryonic gene expression.

We first expressed the H3K4me2/3 demethylase, KDM5B. As expected, removal of the activating H3K4me2/3 marks led to gene down-regulation: 68% (1893 genes) and 80% (1392 genes) of all differentially expressed (FDR < 0.05) genes were down-regulated in sperm- and spermatid-derived embryos, respectively (Fig. 6B; Supplemental Table S6). Importantly, genes down-regulated in sperm-derived embryos showed only limited overlap with those down-regulated in spermatid-derived embryos (Fig. 6C). This indicates a paternal chromatin-dependent effect of H3K4me2/3 removal on embryonic gene expression. Additionally, among the genes affected by H3K4me2/3 removal in sperm- and spermatid-derived embryos, the misregulated genes are overrepresented, indicating that paternal H3K4me2/3 specifically regulates this set of genes (Fig. 6E). Interestingly, the genes down-regulated in spermatid-derived embryos are enriched for H3K4me2/3 in spermatids (Fig. 6D). These observations are in agreement with the hypothesis that the loss of H3K4me2/3 from H3K27me3 marked genes during the spermatid to sperm maturation is necessary for their proper expression in embryos.

To further validate this hypothesis, we tested the influence of paternal H3K27me3 by overexpressing the H3K27me3 demethylase KDM6B (Fig. 6A). In accordance with its repressive function, removal of H3K27me3 at fertilization led to up-regulation of genes at gastrulation in both sperm- and spermatid-derived embryos. Eighty-seven percent (487 genes) and 76% (173 genes) of differentially expressed genes (FDR < 0.05) were up-regulated in sperm- and spermatid-derived embryos, respectively (Fig. 6F; Supplemental Table S6). Again, there was only a partial overlap between genes affected by KDM6B in sperm- and spermatid-derived embryos (Fig. 6G), indicating that this effect is paternal chromatin-dependent. The affected genes were marked by H3K27me3 in the corresponding paternal cells (Fig. 6H). Additionally, upon H3K27me3 demethylation, about five times more genes were specifically up-regulated in sperm- than in spermatid-derived embryos (402 versus 88 genes). This suggests that the programming of genes for embryonic expression in the paternal chromatin relies on the establishment of an effective H3K27me3-mediated repression at the spermatid to sperm transition. Lastly, the misregulated genes are enriched among the genes affected by the H3K27me3 removal, indicating that paternal H3K27me3 specifically regulates this set of genes (Fig. 6E).

Discussion

Previous work characterizing the epigenetic features of sperm in zebrafish, mouse, and human has revealed the presence of modified histones around genes involved in embryonic development (Hammoud et al. 2009; Brykczynska et al. 2010; Wu et al. 2011). In these species, the presence of activating (H3K4me3) and repressive (H3K27me3) histone marks in sperm correlated with gene expression in the early embryos (Hammoud et al. 2009; Brykczynska et al. 2010; Wu et al. 2011). In this work, we have used a comparison of sperm and its immediate precursor, the spermatid, to investigate the functional relationship between histone marks and gene expression.

Our analysis shows that, similar to what has been observed in mouse (Kimura and Yanagimachi 1995; Kishigami et al. 2004), spermatids are not as good at supporting development as sperm. Second, we tested several hypotheses proposed to explain the developmental advantage of sperm over spermatids. We have ruled out the hypothesis that spermatids are less efficient than sperm at supporting replication. Instead, we found evidence supporting the hypothesis that sperm is programmed to support proper embryonic expression of genes encoding important embryonic regulators (Fig. 3). Importantly, overexpression and knockdown studies of several of these genes have shown embryonic developmental defects reminiscent of what is observed in spermatid-derived embryos (*sfp2* [Lee et al. 2006]; *tbx3* [Weidgang et al. 2013]; *foxa2* [Suri et al. 2004]; *otx2* [Yasuoka et al. 2014]). These observations suggest that misexpression of this set of genes is the cause of the developmental defect observed in spermatid-derived embryos. We also showed that the developmental advantage of sperm over spermatids is maintained in haploid, paternally derived embryos, indicating that the effect observed is independent of the presence of the maternal genome. To our knowledge, this is the first time that these two hypotheses, developmental advantage related to ability to support replication versus transcription, have been rigorously tested.

These analyses allowed us to conclude that sperm is not merely a carrier of DNA, but that it also contributes epigenetic information required for proper embryonic gene expression. We then focused our analysis on the sperm chromatin as it represents the most likely vector of such epigenetic information.

During spermiogenesis in *Xenopus laevis*, core histones H3 and H4 are retained, whereas ~90% of core histones H2A and H2B are lost (Risley and Eckhardt 1981). This leaves *Xenopus* sperm with ~10% of the amount of nucleosomal content of a spermatid. This level of histone retention in sperm is higher than that of mouse (~1%) (Brykczynska et al. 2010), lower than that of zebrafish (~100%) (Wu et al. 2011), and similar to that of human (~10%) (Brykczynska et al. 2010). Nucleosome retention in vertebrates therefore seems to show a degree of variation among species. The epigenetic analysis of *Xenopus* sperm provided here extends the repertoire of characterized higher vertebrate sperm chromatin and identifies conserved chromatin features relevant to developmental programming. In that respect, we observed that the programming of sperm for embryonic gene expression entails a loss of H3K4me2/3 marking at H3K27me3 target genes during spermatid to sperm maturation (Fig. 6I). We showed that the set of genes programmed for embryonic expression during *Xenopus* sperm maturation had similar epigenetic features in *Xenopus* and human sperm (Figs. 4C, 5C). So, despite the existence of a hugely variable degree of histone retention in sperm among species, this points toward the existence of universal mechanisms preparing sperm for participation in the normal development of vertebrate embryos.

To functionally test the role of sperm epigenetic marks on embryonic gene expression, one would ideally like to erase these marks from the sperm nucleus immediately prior to the generation of embryos. Chromatin of mature sperm is highly condensed and inaccessible, making enzymatic treatments to alter the epigenetic marks inefficient. Alternative strategies have been developed to use such enzymes either during the process of spermiogenesis, prior to full maturation of sperm (Siklenka et al. 2015), or at fertilization when the sperm chromatin becomes accessible again (used in this study). In mouse, the former strategy has been used to overexpress the H3K4/H3K9 demethylase KDM1A in germ cells. Embryos generated with sperm from animals overexpressing

KDM1A exhibited developmental defects which were transmitted for several generations in the absence of exogenous KDM1A. This analysis demonstrated the existence of epigenetic instruction delivered by sperm to the embryos and transmitted through several generations. However, the overexpression of KDM1A very early in the process of sperm differentiation leads to numerous abnormalities in sperm—for example, the presence of additional mRNAs (Siklenka et al. 2015). These abnormalities are indirect effects of the overexpression of KDM1A early in the process of sperm differentiation. For that reason, it has been difficult to link the difference in gene expression and associated developmental defects to particular epigenetic changes in sperm. The approach we describe here complements and extends previous analyses. First, by comparing the epigenetic profiles of sperm and spermatids to differential gene expression in sperm- and spermatid-derived embryos, we identified H3K4me2/3 and H3K27me3 as candidate marks responsible for the programming of genes. We then tested this hypothesis by demethylating the chromatin using KDM6B (H3K27 demethylase) or KDM5B (H3K4 demethylase) in embryos generated with sperm or spermatids. Importantly, in our experimental setup, both sperm and spermatids used had been through a normal differentiation process. Removal of H3K4me2/3 at fertilization affects different sets of genes in sperm- and spermatid-derived embryos. Genes affected in sperm-derived embryos are enriched for H3K27me3, whereas genes affected in spermatid-derived embryos are enriched for H3K4me2/3. This indicates the importance of H3K4me2/3 dynamics at the transition from spermatid to sperm for patterning of the future embryonic gene expression. One hypothesis to explain the sensitivity of sperm H3K27me3-marked genes to H3K4me2/3 removal would be that these genes acquire H3K4 methylation following fertilization. Our analysis also suggests a conserved role for these marks in *Xenopus* and mouse (Siklenka et al. 2015). Additionally, we also demonstrated that removal of H3K27me3 at fertilization affects the embryonic expression of genes that are marked by H3K27me3 in sperm/spermatids. Recent reports probing histone modifications distribution in mouse and human sperm suggested that these epigenetic marks occurred mostly on repetitive regions of the genome rather than genes (Carone et al. 2014; Samans et al. 2014). These observations put into question the possibility that such marks would influence gene expression in embryos. By providing a functional test of the need for histone modifications for embryonic gene expression, our analysis, together with that of Siklenka et al., clearly shows that, regardless of their genomic location, sperm-delivered modified histones are important regulators of expression in future embryos (Siklenka et al. 2015).

Further investigations into the nature of sperm programming, especially the requirement of other epigenetic marks and their cross-talk in the patterning of embryonic expression, will provide a better understanding of the transgenerational inheritance of epigenetic traits via gametes and could shed light on the mechanisms underlying male infertility and other diseases in humans.

Methods

All the experiments involving the use of animals were conducted according to the regulatory standards of the funding bodies.

Separation of sperm and spermatids

For each round of sperm and spermatid purification, testes from six adult *Xenopus laevis* males were isolated and manually cleaned from blood vessels and fat bodies in 1 × MMR (100 mM NaCl, 2

mM KCl, 2 mM CaCl₂, 1 mM MgCl₂, 5 mM HEPES, pH 7.4) using forceps and paper tissues. It is crucial to clean the testes well from any nontesticular tissues, as otherwise the cells released from the tissues may negatively affect the final purity of isolated cells. Subsequently, testes were torn into small pieces with forceps and homogenized with 2–3 strokes of a Dounce homogenizer (tissue from one testis at a time). The cell suspension was then filtered to remove tissue debris and cell clumps (CellTrics, cat. 04-0042-2317) and spun down at 800 rcf, 4°C, for 20 min. Supernatant was discarded and the cell pellet was resuspended in 12 mL of 1 × MMR. If any red blood cells were visible at the bottom of the pellet (a result of incomplete removal of blood vessels), only the uncontaminated part of the pellet was recovered, taking extreme care not to disturb the red blood cells. Subsequently, step gradients of iodixanol (Optiprep; Sigma, D1556; 60% iodixanol in water) in 1 × MMR final were manually prepared in prechilled 14 mL ultraclear centrifuge tubes (Beckman Coulter, #344060) in the following order from the bottom to the top of the tube: 4 mL of 30% iodixanol, 1 mL of 20% iodixanol, 5 mL of 12% iodixanol (all in 1 × MMR), and 2 mL of cell suspension in 1 × MMR on top. Gradients were spun down in a prechilled SW40Ti rotor at 7500 rpm (10,000g), 4°C, for 15 min, deceleration without brake (Beckman Coulter Ultracentrifuge, Optima L-100XP). The top interface fraction (between 1 × MMR and 12% iodixanol), containing spermatids, and the pelleted fraction, containing mature sperm, were collected. Collected fractions were diluted six times with 1 × MMR and collected by spinning first at 805 rcf, 4°C, for 20 min and respinning at 3220 rcf, 4°C, for 20 min to pellet remaining cells. Pelleted cells were subjected to nuclei preparation (see below).

Sperm and spermatid nuclei preparation, intra-cytoplasmic sperm injections to nonenucleated and to enucleated eggs and embryo culture

Sperm and spermatid nuclei were permeabilized as described before (Smith et al. 2006) and stored at –80°C. Injections were performed using a Drummond Nanoject microinjector (NanojectII Auto Nanolitre Injector, Biohit, 3-00-206A) and glass capillaries (Biohit, 3-00-203-G/XL) pulled using a Flaming-Brown micropipette puller (settings: heat 700, pull 100, velocity 100, time 10). The cell suspension was sucked into the injection needle filled with mineral oil. Cells were injected in sperm dilution buffer (SDB) (Smith et al. 2006), and cell concentration was adjusted by doing mock injections on a microscope slide to deliver one cell per 4.6 nL injection. The eggs were placed in batches of 20–25 on a blotting paper. If they were to be enucleated, they were placed with the animal pole facing upward, whereas if they were not subjected to enucleation, they were placed on a side (with the marginal zone upward). For enucleation, eggs were treated for 30 sec with a UV mineralite lamp (Gurdon 1960) (this step was omitted for nonenucleated eggs). Jelly was removed by a 5-sec Hanovia lamp treatment. The eggs were immediately injected with sperm or spermatid solution and moved to 1 × MBS (Gurdon 1976) supplemented with 0.2% bovine serum albumin (BSA). The cell suspension in the needle was replaced every 20–25 batches of eggs injected. At the four-cell stage, embryos were sorted (all the non-cleaved embryos or those with irregular cleavage furrows were discarded) and the culture media replaced with 0.1 × MBS, 0.2% BSA. Embryos were cultured in 0.1 × MBS, 0.2% BSA (changed daily) in a 16°C–18°C incubator. Assessment of developmental stages was performed according to Nieuwkoop and Faber (Nieuwkoop and Faber 1994). Using this table, matching gastrula embryos from the various experimental groups were collected at stage 10^{1/2}–11 and processed for gene expression analysis (see Supplemental Data procedures for details).

Interphase egg extract preparation

Eggs were collected in $1 \times$ MMR, de-jellied with $0.2 \times$ MBS, 2% cysteine (pH 7.8–7.9) (Sigma, #W326305) and washed with $0.2 \times$ MMR. Subsequently, eggs were activated for 3 min at room temperature (RT) with $0.2 \times$ MMR supplemented with $0.2 \mu\text{g}/\text{mL}$ calcium ionophore (Sigma, #C7522). Eggs were rinsed with $0.2 \times$ MMR, and subsequently all abnormal or not activated eggs were removed. Eggs were washed with 50 mL of ice-cold extraction buffer (EB) (5 mM KCl, 0.5 mM MgCl_2 , 0.2 mM DTT, 5 mM HEPES, pH 7.5) supplemented with protease inhibitors (PI) (Roche, #11873580001), transferred into centrifugation tubes (Thinwall, Ultra-Clear, 5 mL, $13 \times 51\text{-mm}$ tubes, Beckman, #344057), supplemented with 1 mL of EB buffer with PI and $100 \mu\text{g}/\text{mL}$ of cytochalasin B (Sigma, #C2743), and placed on ice for 10 min. Subsequently, eggs were spun briefly at $350g$ for 1 min at 4°C (SW55Ti rotor, Beckman Coulter Ultracentrifuge, Optima L-100XP), and excess buffer was discarded. Eggs were then spun at $18,000g$ for 10 min at 1°C , the extract was collected with a needle, transferred to a fresh, prechilled tube, supplemented with PI and $10 \mu\text{g}/\text{mL}$ of cytochalasin B, and respun using the same conditions. Extract was collected with a needle and used fresh for the replication assay (see below).

Replication in egg extracts and sample preparation for analysis of DNA fibers

Replication on single DNA fibers was performed as described before (Gaggioli et al. 2013) with slight modifications. Freshly prepared egg extracts were supplemented with $20\times$ energy regeneration mix: 2 mg/mL creatine kinase (Roche, #10127566001), 150 mM creatine phosphate (Roche, #10621714001), 20 mM ATP (Roche, #10519979001), 2 mM EGTA, 20 mM MgCl_2 , and with $20 \mu\text{M}$ biotin-16-dUTP (Roche, #11093070910). Permeabilized cells were added to a final concentration of 200 nuclei/ μL of extract and incubated at RT for 2 h (tapping every 10 min). The reaction was stopped by adding 10 volumes of ice-cold $1 \times$ PBS (phosphate buffer saline: 137 mM NaCl, 2.7 mM KCl, 10 mM $\text{Na}_2\text{HPO}_4 \times 2\text{H}_2\text{O}$, 2 mM KH_2PO_4), and cells were spun down at $1000g$, 4°C , for 7 min. Cells were resuspended in $50 \mu\text{L}$ of $1 \times$ PBS and mixed immediately with $50 \mu\text{L}$ of melted (at 65°C) 2% low melting point agarose (Invitrogen, #16520050) in $1 \times$ PBS. After solidification, the agarose plug was incubated overnight (O/N) at 50°C with 1 mL 0.5M EDTA, pH 8, $100 \mu\text{L}$ 10% sarkosyl (Sigma, #L5125), 1 mg/mL Proteinase K (New England Biolabs, #P8102S), followed by three washes in TE pH 6.5. Subsequently, the plug was incubated twice in TE supplemented with 0.1 mM PMSF (Sigma, #93482) for 30 min at 50°C and washed four times with 1 mL of 50 mM MES (Sigma, #69889), pH 6.35, 1 mM EDTA (1 h at RT each wash). Then, the solution was removed; the plug was melted in $400 \mu\text{L}$ of MES pH 6.35, 1 mM EDTA at 68°C for 20 min, and the agarose was digested with 2 units of β -agarase (New England Biolabs, #M0392S) O/N at 42°C .

Analysis of replication on single DNA fibers

Silanized coverslips were prepared as described before (Labit et al. 2008). Thirty microliters of replicated DNA solution was pipetted onto a silanized coverslip, covered with a nonsilanized coverslip, and incubated for 5 min at RT. Subsequently, the top coverslip was slid away to stretch DNA fibers and the silanized coverslip with stretched fibers was fixed in a 3:1 solution of methanol:glacial acetic acid for 10 min, RT. The fibers were then denatured with 2.5 M HCl (1 h, RT) and dehydrated by washes in 70% ethanol, 90% ethanol, and 100% ethanol (1 min for each wash). Subsequently, the coverslip was dried, washed three times in

PBS, 0.1% Tween (Sigma, #P5927) (5 min for each wash) and blocked in 3% BSA in PBS (1 h, RT). All antibodies were diluted in PBS, 3% BSA, 0.1% Tween. Total DNA was detected simultaneously with replicated DNA with primary antibodies: anti-DNA antibody (Millipore, #MAB3034) 1:300 dilution, and streptavidin-Alexa 594 antibody 1:50 to detect biotin (Invitrogen, #S-11227) for 30 min at 37°C . Primary antibodies were washed away with PBS, 0.1% Tween (four washes) and detected with secondary antibodies diluted 1:50: chicken anti-mouse Alexa 488 (Invitrogen, #A-21200) and biotinylated antibody anti-streptavidin (Vector Labs, #BA-0500) for 30 min, 37°C . After four washes in PBS, 0.1% Tween, a tertiary detection was performed with antibodies diluted 1:50: goat anti-chicken Alexa 488 (Invitrogen, #A-11039) and streptavidin-Alexa 594 for 30 min, 37°C . The coverslip was washed three times with PBS, 0.1% Tween, three times in PBS, mounted on a microscope slide with a mounting medium (50% glycerol in PBS), and sealed with nail polish. Images were acquired with a Zeiss 510 META confocal LSM microscope. Image analysis was performed in ImageJ; the amount of replicated DNA and total DNA was measured individually on single DNA fibers.

RNA extraction and preparation of cDNA library for sequencing

Spermatid (1 million) or a pool of five stage 10.5–11.5 embryos were collected and frozen at -80°C . RNA extractions were performed using a Qiagen RNeasy Mini Kit according to the manufacturer's protocol. RNA was eluted in $50 \mu\text{L}$ of DEPC H_2O and used to generate cDNA sequencing libraries using an Illumina TruSeq Kit (#RS-122-2001), according to the manufacturer's protocol.

mRNA injection to one-cell embryos

Mouse KDM6B (aa1025–1642) or KDM5B (aa1–770) were cloned using the p-Entry cloning system (Invitrogen, #K2400-20 and 11791-020) into a pCS2+ plasmid with a C-terminal HA-tag and NLS-tag. mRNA was synthesized *in vitro* using a MEGAScript SP6 Kit (Ambion, AM1330M) following the manufacturer's instructions. Eggs were *in vitro*-fertilized and de-jellied using a 2% cysteine solution in $0.1 \times$ MMR. Injections into one-cell stage embryos were performed in injection solution (Smith et al. 2006) using a Drummond Nanoject microinjector, delivering 9.2 ng of mRNA per injection (mRNA at 1 mg/mL in DEPC H_2O). Embryos were cultured at 18°C and collected for Western blot analysis at stage 21 (Nieuwkoop and Faber 1994). Western blot analyses were performed on 12% polyacrylamide gels using antibodies against H3K27me3 (Cell Signalling, #9733), H3K9me2/3 (Cell Signalling, #5327), H3K4me2/3 (Abcam, #8580), H4 (Abcam, #31830), and against H3 (Abcam, #18521).

Preparation of ChIP-seq samples

Sperm and spermatids were separated as described above. Chromatin fractionation and chromatin immunoprecipitation (ChIP) were performed as described before (Erkek et al. 2013; Hisano et al. 2013) with slight modifications. Pretreatment of sperm cells with DTT was omitted, and chromatin was digested with 2.5 U of MNase/1 million of cells (Roche, #12533700) for 30 min at 37°C . The following antibodies against histone marks were used in the study: anti-H3K4me2 (Millipore, #07-030), anti-H3K4me3 (Abcam, #ab8580), anti-H3K4me3 (Millipore, #CS200580), anti-H3K27me3 (Millipore, #07-449), anti-H3K27me3 (kind gift from Dr. Thomas Jenuwein), and anti-H3K9me3 (Abcam, #ab8898). Before ChIP, primary antibodies were bound to magnetic beads conjugated with secondary antibody (Invitrogen, #11204D) according to the manufacturer's protocol, and all wash steps in the protocol were carried out with a

magnet, instead of centrifugation. Bound DNA was isolated, separated by electrophoresis, and mononucleosomal bands from sperm and spermatids were excised and subjected to library preparation with a TruSeq DNA Kit (Illumina, #FC-121-2001). For the generation of the input sample, 5%–10% of the MNase-digested chromatin was collected, and the same purification scheme was followed as with the immunoprecipitated chromatin prior to library preparation with a TruSeq DNA Kit (Illumina, #FC-121-2001).

Preparation of MBD-seq samples

Sperm and spermatid chromatin were separated as described above, and 200 ng of digested genomic DNA were used to purify methylated DNA using the Methyl Collector TM Ultra Kit (Active Motif, #55005). The purification was carried out according to the manufacturer's instructions, using the low salt buffer to wash the bead-methyl DNA complexes. The purified methylated DNA and the input DNA were then subjected to library preparation with the TruSeq DNA Kit (Illumina, #FC-121-2001).

Sequencing data analysis

Details of the sequencing data analysis methods used in this study are described in the Supplemental Material.

Data access

All ChIP-seq, RNA-seq, MBD-seq, and MNase-seq data sets from this study have been submitted to the NCBI Gene Expression Omnibus (GEO; <http://www.ncbi.nlm.nih.gov/geo/>) under accession number GSE75164.

Acknowledgments

We thank T. Jenuwein and N. Shukeir for the anti-H3K27me3 antibody; A. Bannister, J. Ahringer, and E. Miska for comments on the manuscript; Gurdon group members for reading the manuscript; and The International *Xenopus laevis* Genome Project Consortium (the Harland, Rokhsar, Taira labs, and others) for providing unpublished genome and gene annotation information. M. T. is supported by WT089613 and by Medical Research Council UK (MR/K011022/1). V.G. and P.Z. are funded by AICR 10-0908. A.S. is supported by MR/K011022/1. K.M. is a Research Fellow at Wolfson College and is supported by the Herchel Smith Postdoctoral Fellowship. E.M.M. is supported by National Institutes of Health, National Science Foundation, Cancer Prevention Research Institute of Texas, and the Welch Foundation (F1515). J.J. and J.B.G. are supported by Wellcome Trust (WT101050/Z/13/Z). S.E. acknowledges Boehringer Ingelheim Fond fellowship. A.H.F.M.P. is supported by the Swiss National Science Foundation (31003A_125386) and the Novartis Research Foundation. All members of the Gurdon Institute acknowledge the core support provided by CRUK C6946/A14492 and WT092096.

Author contributions: M.T. and J.J. conceived the study; M.T., A.S., and J.J. analyzed the experiments and wrote the paper; M.T. performed the experiments; V.G. performed and analyzed replication experiments; A.S. performed all bioinformatics analysis; G.E.A. and A.S. analyzed RNA-seq data; K.M. and J.J. performed in vitro maturation/ICSI experiments; S.E. and A.H.F.M.P. helped with ChIP-seq experiments; T.K. and E.M.M. helped to acquire RNA-seq data and provided the *Xenopus laevis* transcriptome and genome; C.R.B. customized the *Xenopus laevis* genome and transcriptome and performed homology searches; A.S., C.R.B., and G.E.A. wrote the experimental procedures section for ChIP-seq

and RNA-seq. K.M., V.G., A.S., P.Z., and J.B.G. helped with the experimental design and paper writing. J.J. and J.B.G. supervised the research.

References

- Brykczynska U, Hisano M, Erkek S, Ramos L, Oakeley EJ, Roloff TC, Beisel C, Schubeler D, Stadler MB, Peters AH. 2010. Repressive and active histone methylation mark distinct promoters in human and mouse spermatozoa. *Nat Struct Mol Biol* **17**: 679–687.
- Bui HT, Wakayama S, Mizutani E, Park KK, Kim JH, Van Thuan N, Wakayama T. 2011. Essential role of paternal chromatin in the regulation of transcriptional activity during mouse preimplantation development. *Reproduction* **141**: 67–77.
- Carone BR, Hung JH, Hainer SJ, Chou MT, Carone DM, Weng Z, Fazzio TG, Rando OJ. 2014. High-resolution mapping of chromatin packaging in mouse embryonic stem cells and sperm. *Dev Cell* **30**: 11–22.
- El-Khoury V, Pierson S, Kaoma T, Bernardin F, Berchem G. 2016. Assessing cellular and circulating miRNA recovery: the impact of the RNA isolation method and the quantity of input material. *Sci Rep* **6**: 19529.
- Erkek S, Hisano M, Liang CY, Gill M, Murr R, Dieker J, Schubeler D, Vlag J, Stadler MB, Peters AH. 2013. Molecular determinants of nucleosome retention at CpG-rich sequences in mouse spermatozoa. *Nat Struct Mol Biol* **20**: 868–875.
- Gaggioli V, Le Viet B, Germe T, Hyrien O. 2013. DNA topoisomerase II α controls replication origin cluster licensing and firing time in *Xenopus* egg extracts. *Nucleic Acids Res* **41**: 7313–7331.
- Gaucher J, Reynoird N, Montellier E, Boussouar F, Rousseaux S, Khochbin S. 2010. From meiosis to postmeiotic events: the secrets of histone disappearance. *FEBS J* **277**: 599–604.
- Gurdon JB. 1960. The effects of ultraviolet irradiation on uncleaved eggs of *Xenopus laevis*. *Q J Microsc Sci* **101**: 299–311.
- Gurdon JB. 1976. Injected nuclei in frog oocytes: fate, enlargement, and chromatin dispersal. *J Embryol Exp Morphol* **36**: 523–540.
- Gurdon JB, Elsdale TR, Fischberg M. 1958. Sexually mature individuals of *Xenopus laevis* from the transplantation of single somatic nuclei. *Nature* **182**: 64–65.
- Hammoud SS, Nix DA, Zhang H, Purwar J, Carrell DT, Cairns BR. 2009. Distinctive chromatin in human sperm packages genes for embryo development. *Nature* **460**: 473–478.
- Hisano M, Erkek S, Dessus-Babus S, Ramos L, Stadler MB, Peters AH. 2013. Genome-wide chromatin analysis in mature mouse and human spermatozoa. *Nat Protoc* **8**: 2449–2470.
- Hutchison CJ, Brill D, Cox R, Gilbert J, Kill I, Ford CC. 1989. DNA replication and cell cycle control in *Xenopus* egg extracts. *J Cell Sci Suppl* **12**: 197–212.
- Ihara M, Meyer-Ficca ML, Leu NA, Rao S, Li F, Gregory BD, Zalenskaya IA, Schultz RM, Meyer RG. 2014. Paternal poly (ADP-ribose) metabolism modulates retention of inheritable sperm histones and early embryonic gene expression. *PLoS Genet* **10**: e1004317.
- Kimura Y, Yanagimachi R. 1995. Mouse oocytes injected with testicular spermatozoa or round spermatids can develop into normal offspring. *Development* **121**: 2397–2405.
- Kishigami S, Wakayama S, Nguyen VT, Wakayama T. 2004. Similar time restriction for intracytoplasmic sperm injection and round spermatid injection into activated oocytes for efficient offspring production. *Biol Reprod* **70**: 1863–1869.
- Labit H, Goldar A, Guilbaud G, Douarce C, Hyrien O, Marheineke K. 2008. A simple and optimized method of producing silanized surfaces for FISH and replication mapping on combed DNA fibers. *Biotechniques* **45**: 649–652, 654, 656–658.
- Lee HX, Ambrosio AL, Reversade B, De Robertis EM. 2006. Embryonic dorsal-ventral signaling: secreted frizzled-related proteins as inhibitors of tolloid proteinases. *Cell* **124**: 147–159.
- Lemaitre JM, Vassetzky Y, Mechali M. 2001. Analysis of chromatin assembly, chromatin domains, and DNA replication using *Xenopus* systems. In *Mapping protein/DNA interactions by cross-linking*. Institut National de la Santé et de la Recherche Médicale, Paris.
- Lemaitre JM, Danis E, Pasero P, Vassetzky Y, Mechali M. 2005. Mitotic remodeling of the replicon and chromosome structure. *Cell* **123**: 787–801.
- Narbonne P, Simpson DE, Gurdon JB. 2011. Deficient induction response in a *Xenopus* nucleocytoplasmic hybrid. *PLoS Biol* **9**: e1001197.
- Nieuwkoop PD, Faber J. 1994. *Normal table of Xenopus laevis (Daudin): asystematical and chronological survey of the development from the fertilized egg till the end of metamorphosis*. Garland Pub, New York.
- Paradowska AS, Miller D, Spiess AN, Vieweg M, Cerna M, Dvorakova-Hortova K, Bartkuhn M, Schuppe HC, Weidner W, Steger K. 2012.

- Genome-wide identification of promoter binding sites for H4K12ac in human sperm and its relevance for early embryonic development. *Epigenetics* **7**: 1057–1070.
- Risley MS, Eckhardt RA. 1981. H1 histone variants in *Xenopus laevis*. *Dev Biol* **84**: 79–87.
- Samans B, Yang Y, Krebs S, Sarode GV, Blum H, Reichenbach M, Wolf E, Steger K, Dansranjavin T, Schagdarsurengin U. 2014. Uniformity of nucleosome preservation pattern in mammalian sperm and its connection to repetitive DNA elements. *Dev Cell* **30**: 23–35.
- Siklenka K, Erkek S, Godmann M, Lambrot R, McGraw S, Lafleur C, Cohen T, Xia J, Suderman M, Hallett M, et al. 2015. Disruption of histone methylation in developing sperm impairs offspring health transgenerationally. *Science* **350**: aab2006.
- Smith SJ, Fairclough L, Latinkic BV, Sparrow DB, Mohun TJ. 2006. *Xenopus laevis* transgenesis by sperm nuclear injection. *Nat Protoc* **1**: 2195–2203.
- Suri C, Haremak T, Weinstein DC. 2004. Inhibition of mesodermal fate by *Xenopus* HNF3 β /FoxA2. *Dev Biol* **265**: 90–104.
- Suzuki T, Minami N, Kono T, Imai H. 2007. Comparison of the RNA polymerase I-, II- and III-dependent transcript levels between nuclear transfer and *in vitro* fertilized embryos at the blastocyst stage. *J Reprod Dev* **53**: 663–671.
- Vassena R, Han Z, Gao S, Baldwin DA, Schultz RM, Latham KE. 2007. Tough beginnings: alterations in the transcriptome of cloned embryos during the first two cell cycles. *Dev Biol* **304**: 75–89.
- Weidgang CE, Russell R, Tata PR, Kuhl SJ, Illing A, Muller M, Lin Q, Brunner C, Boeckers TM, Bauer K, et al. 2013. TBX3 directs cell-fate decision toward mesoderm. *Stem Cell Rep* **1**: 248–265.
- Wu SF, Zhang H, Cairns BR. 2011. Genes for embryo development are packaged in blocks of multivalent chromatin in zebrafish sperm. *Genome Res* **21**: 578–589.
- Yasuoka Y, Suzuki Y, Takahashi S, Someya H, Sudou N, Haramoto Y, Cho KW, Asashima M, Sugano S, Taira M. 2014. Occupancy of tissue-specific cis-regulatory modules by Otx2 and TLE/Groucho for embryonic head specification. *Nat Commun* **5**: 4322.
- Zheng Z, Jia JL, Bou G, Hu LL, Wang ZD, Shen XH, Shan ZY, Shen JL, Liu ZH, Lei L. 2012. rRNA genes are not fully activated in mouse somatic cell nuclear transfer embryos. *J Biol Chem* **287**: 19949–19960.
- Ziyat A, Lefevre A. 2001. Differential gene expression in pre-implantation embryos from mouse oocytes injected with round spermatids or spermatozoa. *Hum Reprod* **16**: 1449–1456.

Received November 16, 2015; accepted in revised form March 29, 2016.



Sperm is epigenetically programmed to regulate gene transcription in embryos

Marta Teperek, Angela Simeone, Vincent Gaggioli, et al.

Genome Res. 2016 26: 1034-1046 originally published online March 31, 2016

Access the most recent version at doi:[10.1101/gr.201541.115](https://doi.org/10.1101/gr.201541.115)

Supplemental Material <http://genome.cshlp.org/content/suppl/2016/07/10/gr.201541.115.DC1>

References This article cites 33 articles, 6 of which can be accessed free at:
<http://genome.cshlp.org/content/26/8/1034.full.html#ref-list-1>

Open Access Freely available online through the *Genome Research* Open Access option.

Creative Commons License This article, published in *Genome Research*, is available under a Creative Commons License (Attribution 4.0 International), as described at <http://creativecommons.org/licenses/by/4.0/>.

Email Alerting Service Receive free email alerts when new articles cite this article - sign up in the box at the top right corner of the article or [click here](#).

To subscribe to *Genome Research* go to:
<http://genome.cshlp.org/subscriptions>



Insights into the Regulation of Implantation and Placentation in Humans, Rodents, Sheep, and Pigs

2

Claire Stenhouse, Heewon Seo, Guoyao Wu, Gregory A. Johnson, and Fuller W. Bazer

Abstract

Precise cell-specific spatio-temporal molecular signaling cascades regulate the establishment and maintenance of pregnancy. Importantly, the mechanisms regulating uterine receptivity, conceptus apposition and adhesion to the uterine luminal epithelia/superficial glandular epithelia and, in some species, invasion into the endometrial stroma and decidualization of stromal cells, are critical prerequisite events for placentation which is essential for the appropriate regulation of fetoplacental growth for the remainder of pregnancy. Dysregulation of these signaling cascades during this critical stage of pregnancy can lead to pregnancy loss, impaired growth and development of the conceptus, and alterations in the transplacental exchange of gasses and nutrients. While many of these processes are conserved across species, significant variations in the molecular mechanisms governing maternal recognition of pregnancy, conceptus implantation, and placentation exist. This review addresses the complexity of key mechanisms that are critical for the establishment and maintenance of a

successful pregnancy in humans, rodents, sheep, and pigs. Improving understanding of the molecular mechanisms governing these processes is critical to enhancing the fertility and reproductive health of humans and livestock species.

Keywords

Conceptus · Endometrium · Implantation · Placentation · Pregnancy

List of Abbreviations

AKR1C1	Aldo-keto reductase family 1 member C1
BH4	Tetrahydrobiopterin
CE	Chorionic epithelium
CGB	Chorionic gonadotrophin beta
CL	Corpus luteum
CST3	Cystatin C
CTB	Cytotrophoblasts
CTSL	Cathepsin L
CYPs	Cytochrome P450 mixed-function oxidases
E2	Estradiol
ECM	Extracellular Matrix
ESR1	Estradiol receptor
eEVT	Endovascular extravillous trophoblast
EVT	Extravillous trophoblast
FGF	Fibroblast growth factor
FGFR	Fibroblast growth factor receptor
GCH1	GTP cyclohydrolase 1

C. Stenhouse · H. Seo · G. Wu · G. A. Johnson · F. W. Bazer (✉)
Department of Animal Science and Department of Veterinary Integrative Biosciences, Texas A&M University, College Station, TX 77843, USA
e-mail: fbazer@cvm.tamu.edu

GE	Glandular epithelium	TGC	Trophoblast giant cell
GLYCAM1	Glycosylation dependent cell adhesion molecule 1	TGFB	Transforming growth factor beta
GNRH	Gonadotropin-releasing hormone	TIMPs	Tissue inhibitors of matrix metalloproteins
GNRHR	Gonadotropin-releasing hormone receptor	TPA	Tissue-type plasminogen activator
HBEGF	Heparin-binding epidermal growth factor	UF	Uteroferrin
HGF	Hepatocyte growth factor	UPA	Urokinase-type plasminogen activator
HIF2A	Hypoxia inducible factor 2 α	WNT	Wingless-related integration site
HLA	Human leukocyte antigen	20 α -OHP	20 α -Hydroxyprogesterone
ICM	Inner cell mass	20 α HSD	20 α -Hydroxysteroid dehydrogenase
iEVT	Interstitial extravillous trophoblast		
IFND	Interferon delta		
IFNG	Interferon gamma		
IFNT	Interferon tau		
IL1B	Interleukin-1 beta		
IRF	Interferon regulatory factor		
ISG	Interferon stimulated gene		
LE	Luminal epithelium		
LGALS15	Galectin 15		
LH	Luteinizing hormone		
LHCGR	Luteinizing hormone/choriogonadotropin receptor		
MAPK	Mitogen activated protein kinases		
MMP	Matrix metalloproteinases		
MTORC	Mechanistic target of rapamycin		
MUC1	Mucin 1		
OXT	Oxytocin		
OXTR	Oxytocin receptor		
P4	Progesterone		
PA1	Plasminogen activator inhibitor		
PGF	Prostaglandin F2 α		
PGFM	Prostaglandin F2 α metabolite		
PGR	Progesterone receptor		
PI3K	Phosphoinositide-3 kinase		
PRL	Prolactin		
PTGFR	Prostaglandin F2 α receptor		
PTGS2	Prostaglandin synthase 2		
sGE	Superficial glandular epithelium		
SLC	Solute carrier family		
SPP1	Secreted phosphoprotein 1		
STAT1	Signal transducer and activator of transcription 1		
STB	Syncytiotrophoblast		

2.1 Introduction

The establishment and maintenance of pregnancy requires a series of complex and concerted events to maximize the likelihood of a successful outcome of pregnancy (Bazer et al. 2011). This intricate process is reliant upon precise cell-specific spatio-temporal molecular signaling between the developing conceptus (embryo and associated placental membranes) and the uterine endometrium during conceptus elongation, adhesion, apposition, attachment, and formation of a functional placenta. While many of these processes are conserved across species, significant variations in the molecular mechanisms governing maternal recognition of pregnancy, conceptus implantation, and placentation exist. Dysregulation of these signaling cascades during this critical stage of pregnancy can lead to pregnancy loss, impaired growth and development of the conceptus, and alterations in the transplacental exchange of gasses and nutrients (Bazer and Johnson 2014; Wu 2022). This review addresses the complexity of key mechanisms that are critical for the establishment and maintenance of a successful pregnancy in humans, rodents, sheep, and pigs. Improving understanding of the molecular mechanisms governing these processes is critical to enhancing the fertility and reproductive health of humans and livestock species.

2.2 Fertilization and Embryonic Development to the Blastocyst Stage in Mammals

In all mammals, fertilization occurs in the oviduct when oocytes from the mammalian ovary fuse with sperm from the male to produce a one-cell embryo (the zygote) with a diploid (maternal and paternal) set of chromosomes. The zygote and embryo in the early stages of development are within the zona pellucida; a protective membrane composed mostly of glycoproteins (Wassarman 1988). The zygote goes through rapid cell division to the 2-cell, 4-cell, 8-cell, and so on to form a 32- to 64-cell stage embryo known as a morula. Thereafter, in addition to continued proliferation of cells, the cells segregate and differentiate to form either the embryonic disc (also known as the inner cell mass) or trophoctoderm, and those entities surround a blastocoel into which nutrients are transported. The free-floating blastocyst must emerge, a process known as “hatching” from the zona pellucida (Wassarman and Litscher 2008). This involves proteases and glycosidases that allow rupture of the zona pellucida and emergence of the blastocyst so that it can expand in preparation for implantation on the epithelial lining of the uterine lumen.

Here, we will discuss this process in more detail for humans and rodents in which the blastocyst, in a spherical form, invades into the uterine endometrium to gain access to maternal blood for the exchange of nutrients and gases, i.e., carbon dioxide and oxygen. In contrast, blastocysts of sheep and pigs undergo a rapid and unique transformation from a spherical form to a tubular form and then a greatly elongated filamentous form without invading into the endometrium. Blastocysts elongate from 10 mm spheres to 250 mm filamentous forms in sheep and up to 1,000 mm elongated forms in pigs (Bazer 2013). Elongation of the trophoctoderm is essential for creating a large surface area for uptake of nutrients and exchange of gases. The following sections will provide details of species-specific mechanisms for pregnancy recognition signaling, conceptus development, and implantation.

2.3 Pre-Implantation Conceptus Development in Humans, Sheep, Pigs, and Rodents

2.3.1 Pregnancy Recognition Signaling

For pregnancy to be established and maintained, the conceptus (embryo and its extra-embryonic membranes) must provide a hormonal signal for maternal recognition of pregnancy (Spencer and Bazer 2004). The estrous cycle of subprimate species is uterine-dependent because the uterus is the source of prostaglandin $F_{2\alpha}$ (PGF), the luteolytic hormone responsible for functional and structural regression of the ovarian corpus luteum (CL) (Stouffer 1988). With regression of the CL and decreasing concentrations of progesterone (P4) in the circulation, the estrous or menstrual cycle begins anew. In primates, however, the menstrual cycle is uterine-independent as luteolytic PGF is from an intra-ovarian source (Stouffer et al. 2014). While differences in the maternal recognition of pregnancy signals exist among species, they are from conceptus trophoctoderm to maternal uterus or ovarian corpora lutea (CL). These signals from the conceptus are either anti-luteolytic, i.e., they prevent the release of luteolytic PGF from the uterus, or they are luteotrophic and act directly on the CL to prevent luteolysis (Spencer and Bazer 2004).

2.3.2 Pregnancy Recognition Signaling in Humans

Pregnancy recognition signals are required to extend the lifespan of the CL that produces P4, the hormone required for the establishment and maintenance of pregnancy. For primates, the CL is the sole source of P4 until the time of the luteal-placental shift when production of P4 by the placenta is sufficient to support pregnancy (Stouffer and Hearn 1998; Fazleabas et al. 2004). Three to four days following ovulation in primates, morula stage embryos enter the uterus, hatch from the zona pellucida, and initiate

implantation, with trophoblast cells attaching to uterine luminal epithelium (LE) 7–9 Days post-ovulation in humans. In primates, the production of chorionic gonadotrophin beta (CGB) by trophoblast of blastocyst signals maternal recognition of pregnancy and acts via the receptor for Luteinizing Hormone (LHCGR) (Srisuparp et al. 2001). In all primates, CGB is detectable in maternal blood around the time of implantation, with a peak in concentrations during the first trimester, before decreasing during late gestation. The expression of *CGB* mRNA has been detected in both 8-cell embryos and hatched blastocysts from women (Bonduelle et al. 1988; Syrkasheva et al. 2017).

In the human trophoblast, gonadotropin-releasing hormone 1 (luteinizing-releasing hormone) (GNRH1) from the uterus is believed to regulate the production of CGB, as receptors for GNRH1 (GNRHR) are expressed by trophoblast. GNRH agonists and antagonists enhance and suppress secretion of CGB, respectively, suggesting a pivotal regulatory role of GNRH in the production of CGB. Additionally, inhibin, activin, steroids, and P4, from the ovary and/or placenta, may regulate production of CGB. The secretion of CGB is critical for CL maintenance in early pregnancy; however, around the time of the luteal-placental shift in P4 production, the production of CGB decreases. Immunization of primates with modified forms of CGB results in infertility, but the immunized animals continue to exhibit normal menstrual cycles. Further, administration of exogenous CGB increases the production of P4 while extending the lifespan of the CL in women.

2.3.3 Pregnancy Recognition Signaling in Rodents

Laboratory rodents are spontaneously ovulating, non-seasonal, polyestrous mammals, with short-generation intervals, making them valuable and extensively utilized animal models for studies of conceptus growth and development. Rodents have estrous cycles of 4–5 days in length that include proestrus (12–14 h), estrus (25–27 h),

metestrus (6–8 h), and diestrus (55–57 h) (Freeman et al. 1974; Soares et al. 2007). The CL of cyclic rats and mice, initially secrete P4 for two days. Pulses of prolactin from the anterior pituitary gland are produced following vaginal stimulation to allow the CL to become fully functional and produce P4. Newly formed CL are maintained in rats through metestrus of the following cycle, after which time the luteal cells undergo apoptosis, blood vessels degenerate, and leukocytes infiltrate the CL to remove cellular debris. In cyclic rodents, P4 secreted by the CL is metabolized by aldo-keto reductase family 1 member C1 (AKR1C1; also known as 20 α -hydroxysteroid dehydrogenase [20 α -HSD]) to 20 α -hydroxyprogesterone (20 α -OHP). The uterine decidual reaction required for the establishment of pregnancy is not induced by 20 α -OHP. The secretion of 20 α -OHP by the CL declines during diestrus, until the onset of proestrus when estrus and ovulation begin a new cycle.

The CL must continue to produce P4 until Day 17 of the 20–22 Days gestation period in rats, mice, and hamsters. The production of P4 is necessary for implantation, induction of the uterine decidual reaction, placentation, and a successful pregnancy (Soares et al. 2007). Two endocrine events are critical for the establishment and maintenance of pregnancy. Mating induces diurnal and nocturnal surges the secretion of prolactin (PRL) from lactotroph cells in the anterior pituitary. This increases the expression of LHCGR on luteal cells and suppresses AKR1C1 (20 α -HSD) activity in the CL that prevents the conversion of P4 to 20 α -OHP (Gunn et al. 1983; Soares et al. 2007). Second, maintenance of pregnancy beyond Day 12 in rodents is reliant upon implantation, conceptus development, and the production of lactogenic hormones by both the uterine decidua and placenta (Soares 2004). Prolactin and placental lactogen are members of the lactogenic family of hormones, which act in a luteotrophic manner in mice and rats to ensure CL maintenance and its continued secretion of P4 required for the establishment and maintenance of pregnancy to full term (Soares et al. 2006, 2007).

2.3.4 Pregnancy Recognition Signaling in Sheep

In sheep, regulation of the estrous cycle is dependent upon the production of PGF by the uterine epithelia (Bazer et al. 1994; Thatcher et al. 1995). P4 acts upon the uterine epithelia during diestrus to increase phospholipid stores and expression of prostaglandin synthase 2 (PTGS2), both of which are necessary for mobilization of arachidonic acid by phospholipase A2 and conversion of arachidonic acid by PTGS2 to PGF. Importantly, P4 acts upon the uterus to down-regulate the expression of the progesterone receptors (PGR) which increases the expression of receptors for estradiol (ESR1) and oxytocin (OXTR) in uterine LE and superficial glandular epithelia (sGE) initially, and later in glandular epithelia (GE) and stromal cells (Spencer and Bazer 2004). These alterations in uterine epithelial gene expression are critical events in activation of the luteolytic mechanism for the production of luteolytic pulses of PGF by the uterus in sheep. Estradiol (E2), acting via ESR1, induces expression of phospholipase A2 that mobilizes arachidonic acid for conversion to PGF. The posterior pituitary and CL release pulses of OXT which binds to the OXTR to induce the pulsatile release of PGF. The pulsatile production of PGF induces regression of CL by Day 16 of the estrous cycle.

In ruminants, the signal for maternal recognition of pregnancy is interferon tau (IFNT) (Bazer 2013). IFNT, a Type I interferon, is produced by the mononuclear trophoctoderm cells of the conceptus during the peri-implantation period of pregnancy as the conceptus undergoes morphological transition from spherical, to tubular, and filamentous forms (Bazer et al. 2018). Secretion of ovine IFNT begins on about Day 10 and increases to Day 16, then decreases to Day 21 after which production ceases and the IFNT gene is no longer expressed by the conceptus. In summation, IFNT silences transcription of ESR1 to preclude estrogen receptor α interactions with SP1 and/or AP-1 that otherwise stimulate oxytocin receptor expression in uterine LE/sGE to

abrogate the oxytocin-dependent pulsatile release of luteolytic PGF (Fig. 2.1) [reviewed by (Bazer et al. 2015b)]. Thus, the CL is maintained to produce P4, the hormone of pregnancy (Fleming et al. 2006). Interferon tau also has potent antiviral, antiproliferative, and immunomodulatory activities characteristic of other Type I interferons (Bazer et al. 2015b).

The loss of expression of PGR in uterine epithelia cells on Days 12–13 of pregnancy is essential for activation of key events required for the establishment of pregnancy (Bazer et al. 2009). The loss of PGR by endometrial epithelia is required for implantation that is dependent on the loss of expression of some genes, such as mucin 1 (MUC1), on the surface of uterine LE, that would otherwise block implantation. In addition to down-regulation of expression of PGR and ESR1 by uterine epithelia being a prerequisite for uterine receptivity to conceptus implantation, this is also critical for up-regulation of the expression of many genes including those for secretory proteins and nutrient transporters for transport of glucose and amino acids into the uterine lumen to support growth and development of the conceptus. Down-regulation of PGR in uterine epithelia allows P4 to act on PGR-positive uterine stromal cells, upregulating the expression of progesterone receptors, i.e., fibroblast growth factor 7 (FGF7) and -10 (FGF10), and hepatocyte growth factor (HGF). The progesterone receptors exert paracrine effects on uterine epithelia and conceptus trophoctoderm which express receptors for FGF7 and FGF10 (*FGFR2IIIb*) and HGF (MET; protooncogene *MET*) (Igarashi et al. 1998; Chen et al. 2000a, b). Whilst the expression of many IFNT-stimulated genes (ISGs) are known to be induced by P4 and stimulated by IFNs (Bazer et al. 2008), it is not known if progesterone receptors and IFNs act on uterine epithelial cells via non-classical cell signaling pathways, independent of PGR and signal transducer and activator of transcription 1 (STAT1) to alter gene expression and uterine receptivity to implantation [reviewed by (Bazer et al. 2015b)]. Type I IFNs may bind to the same receptor, but activate unique cell-specific

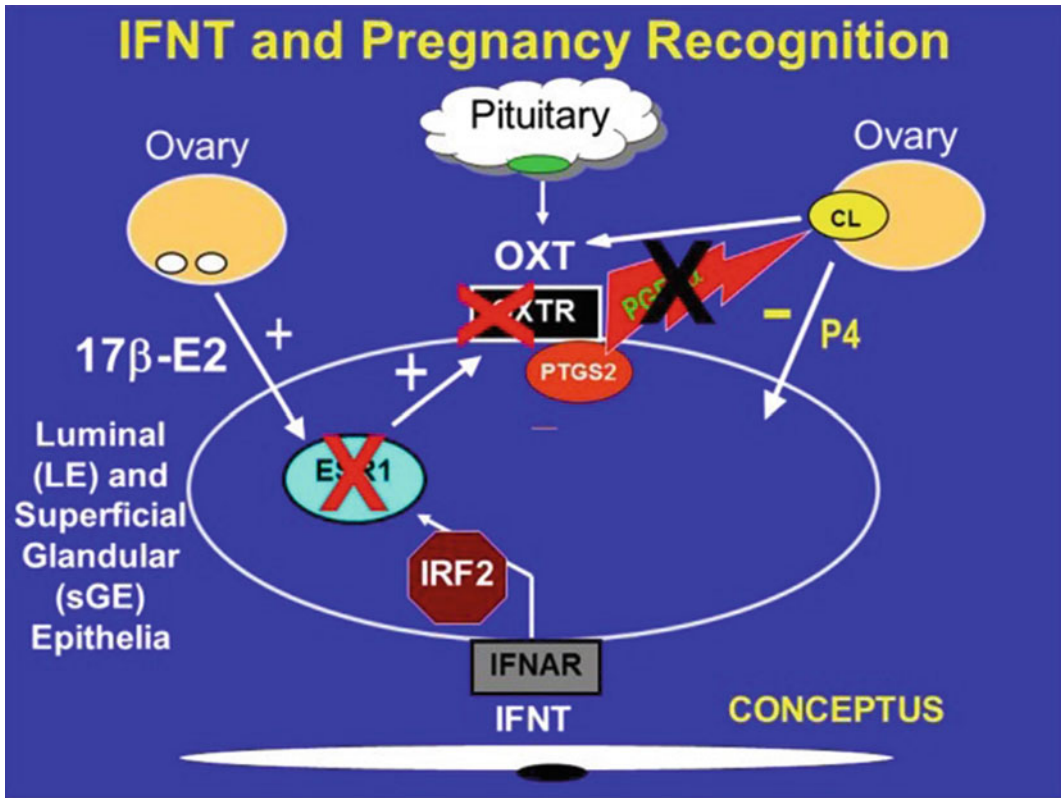


Fig. 2.1 Interferon tau (IFNT) is the pregnancy recognition hormone in sheep and other ruminants. It acts to silence expression of estrogen receptor alpha (ESR1) and, in turn, oxytocin receptor (OXTR) to prevent development of the luteolytic mechanism which requires oxytocin (OXT) from the corpus luteum (CL) and posterior

pituitary to induce luteolytic pulses of prostaglandin $F_{2\alpha}$ (PGF). Thus, IFNT blocks the ability of the uterus to develop the luteolytic mechanism but does not inhibit prostaglandin synthase 2 (PTGS2) or the basal production of PGF during pregnancy. Adapted from the Open Access article of Bazer (2013)

signaling pathways that differentially effect gene expression in uterine LE, sGE, GE, and stromal cells [reviewed by (Bazer et al. 2015b)].

In sheep, IFNT up-regulates IRF2 in uterine LE and sGE and this inhibits expression of classical ISGs such as STAT1 and interferon regulatory factor 9 (IRF9) in those cells (Choi et al. 2001; Bazer et al. 2015b). However, there is a growing number of P4-induced and IFNT-stimulated genes being discovered to be expressed uterine LE/sGE that lack both PGR and STAT1 and are critical for implantation and conceptus development. Those genes include wingless-type MMTV integration site family member 7A (WNT7A), galectin 15 (LGALS15),

cathepsin L (CTSL), cystatin C (CST3), solute carrier family 2 member 1 (SLC2A1), solute carrier family 7 member 1 (SLC7A1), solute carrier family 7 member 2 (SLC7A2), and hypoxia inducible factor 2 α (HIF2A).

2.3.5 Pregnancy Recognition Signaling in Pigs

After stimulation of the uterine endometrium by P4 for 10–12 days, luteolysis occurs during late diestrus and early proestrus, there is an accumulation of phospholipids and necessary enzymes for production of PGF in a pulsatile

manner (Bazer 1989). It is not until Days 12–13 of the estrous cycle that porcine CL are sufficiently responsive to luteolytic PGF because until that time they express few receptors for PGF (PTGFR). The posterior pituitary and CL produce OXT which binds to uterine OXTR to elicit pulsatile release of PGF. In contrast to other species, the porcine CL has a very low abundance of both OXT and vasopressin; therefore, the role(s), if any, of these neuropeptides in luteolysis in pigs is not known. Further, the uterine endometrium is a source of OXT in pigs, although its potential roles in regulating the estrous cycle or aspects of pregnancy are not known. However, administration of exogenous OXT to gilts decreases the inter-estrous interval if administered between Days 10 and 16 post-estrus. This finding is not observed when OXT is administered to hysterectomized gilts with intact ovaries, suggesting that any effect of OXT on length of the estrous cycle is uterine-dependent. Both OXTR and lysine vasopressin receptors are expressed by cells of the porcine endometrium, but the endometrium only responds to OXT with increased secretion of PGF. Further, both OXT and vasopressin stimulate calcium-calmodulin kinase and protein kinase C signaling pathways in the porcine endometrium. Increased pulsatile secretion of PGF occurs between Days 14 and 18 of the estrous cycle as OXT increases the activity of phospholipase C and the hydrolysis of phosphatidylinositol (Bazer et al. 1984). Increases in intracellular calcium and diacylglycerol activate protein kinase C and calcium-calmodulin kinase which, in turn, activate phospholipase A₂ and the release of arachidonic acid, ultimately leading to the pulsatile production of PGF. During luteolysis, concentrations of OXT increase in maternal blood. Interestingly, the OXT-induced increases in circulating concentrations of prostaglandin F₂α metabolite (PGFM) are lower in pregnant than cyclic gilts or gilts induced into pseudo-pregnancy by injection of exogenous E2 from Day 11 to Day 15 post-estrus. Concentrations of PGFM in blood of pregnant gilts increase beginning on Day 12. In addition, inhibition of prostaglandin synthesis results in pregnancy failure. Collectively these findings suggest an

important role of prostaglandins in the establishment of pregnancy in pigs.

Porcine blastocysts hatch from the zona pellucida and expand before undergoing a rapid morphological transition to large spherical, tubular, and filamentous forms between Days 10 and 12 of pregnancy as they become conceptuses. These rapidly elongating conceptuses achieve a length of 800–1000 mm between Days 12 and 15 of pregnancy (Bazer and Johnson 2014), with the trophectoderm secreting many critical molecules for the establishment of pregnancy including estrogens, interleukin 1B, interferon gamma (IFNG), and interferon delta (IFND). In the absence of a conceptus, the uterine endometrium secretes PGF in an endocrine manner into its venous drainage to be transported through the maternal vasculature to the ovary where it can exert its luteolytic effect on the CL. In contrast, in pregnant gilts, the conceptus produces E2 from around Days 11–12 until Day 15 of pregnancy that is the maternal recognition signal. E2 acts on uterine epithelia to direct secretion of PGF away from the uterine vasculature and into the uterine lumen (exocrine secretion) where it is sequestered and metabolized, thereby preventing luteolysis (Fig. 2.2).

The conceptus estrogens not only act as the signal for maternal recognition in pigs, but also modulate uterine gene expression responsible for endometrial remodeling for implantation between Days 13 and 25 of gestation (Johnson et al. 2009). There is a report (Meyer et al. 2019) that silencing expression of the aromatase (CYP19A1) gene, utilizing CRISPR/Cas9 genome editing technology, did not prevent elongation and implantation of pig conceptuses or maintenance of CL through the peri-implantation period, but the pregnancies failed around Day 30 of gestation. Therefore, further investigation to ascertain the regulatory role of estrogens in the establishment of pregnancy in the pig should be performed.

The following critical events must be tightly regulated to allow the establishment and maintenance of pregnancy in the pig: (i) the conceptus must secrete estrogens to act as the maternal recognition of pregnancy signal; (ii) the uterine LE and GE must provide, through nutrient

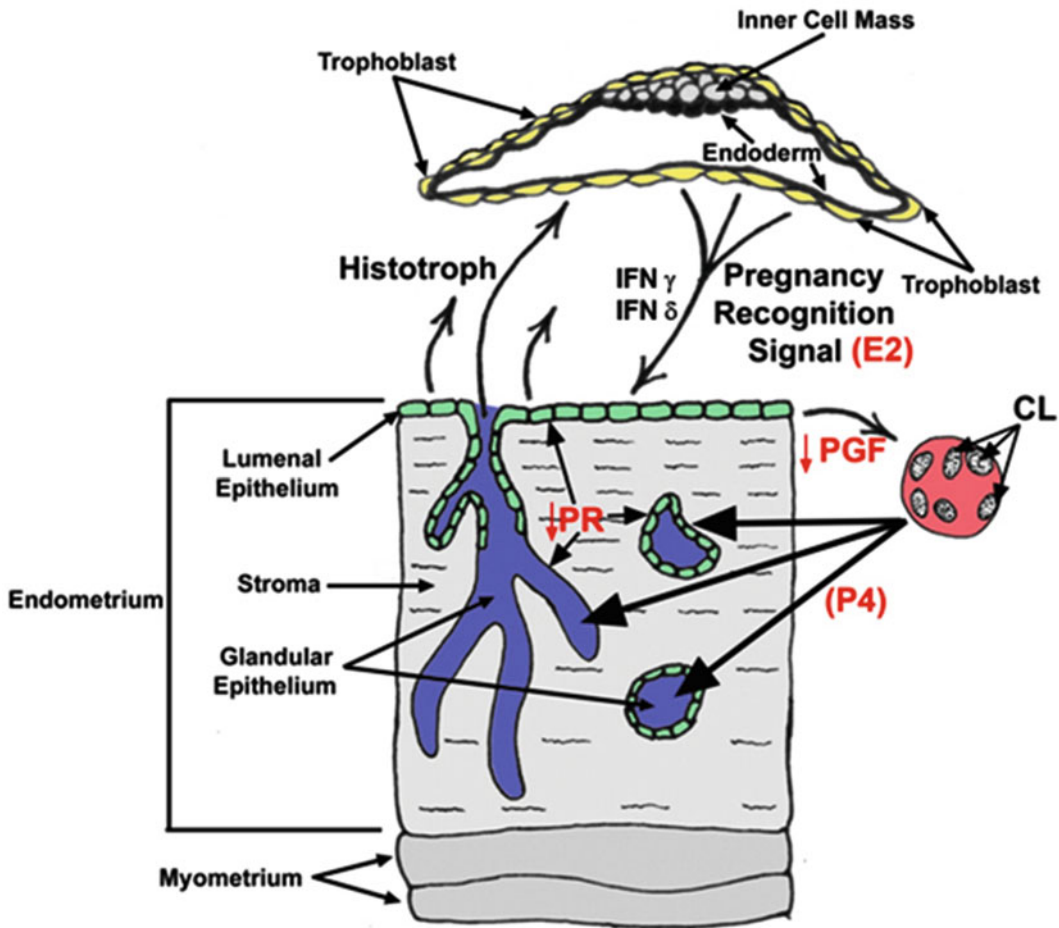


Fig. 2.2 The theory of pregnancy recognition in the pig is based on evidence that estradiol (E2), as the pregnancy recognition signal, which redirects secretion of prostaglandin $F_{2\alpha}$ (PGF) away from endocrine secretion into the uterine vasculature and into exocrine secretion into the uterine lumen, allowing metabolism to PGE or its inactive metabolite. The roles of interferon delta and gamma in

early pregnancy are not yet fully understood. This figure also illustrates that there is down-regulation of expression of receptors for progesterone (PR) in uterine epithelia; therefore, progesterone (P4) acts on uterine stromal cells to regulate expression of genes associated with the secretion of histotroph into the uterine lumen. Adapted from Bazer and Johnson (2014)

transport and secretions, nutrient rich histotroph to support attachment, development, and growth of the conceptus; and (iii) cellular remodeling at the uterine LE:trophectoderm required for implantation and the initiation of placentation. In addition to the critical role of P4 and E2, the spatio-temporal changes in gene expression in both the trophectoderm and endometrium are regulated by interleukin-1 beta (IL1B), the interferons (IFND and IFNG), transforming growth factor beta (TGFβ) and fibroblast growth

factor 7 (FGF7). Interferons appear to have a crucial role in the establishment of pregnancy across mammalian species, with reports of up-regulation of interferon stimulated gene expression in response to conceptus secreted IFNs in many species. Significant antiviral activity is present in Day 14 uterine flushings from pregnancy pigs, with IFNG accounting for approximately 75% of this activity, suggesting a pivotal role for this interferon in the establishment of pregnancy. The pig is unique in that conceptus

produced estrogens induce expression of IRF2 only in uterine LE (Joyce et al. 2007). Considering this, it could be speculated that IFND and IFNG work synergistically to induce classical interferon responsive genes only in uterine GE and stromal cells which do not express IRF2, while uterine LE in direct contact with conceptus trophoctoderm is induced to express novel genes, e.g., nutrient transporters for glucose and amino acids that enhance conceptus development.

Uterine histotroph in pigs is composed of secretions from uterine epithelia and molecules that are selectively transported into the uterine lumen (Bazer et al. 2018). In addition to glucose, fructose, amino acids, and other micromolecules, it contains a very complex mixture of peptides that proteins that include: uteroferrin, now known as ACP5 (phosphatase, acid, type 5, tartrate resistant) which transports iron to the conceptus for erythropoiesis and stimulates hematopoiesis; retinol binding protein, plasmin/trypsin inhibitor, leucine aminopeptidase, glucose phosphate isomerase, serine protease inhibitors, lysozyme, various proteases, hexosaminidase, phospholipases, prostaglandin synthases, insulin-like growth factors 1 and 2, insulin-like growth factor binding proteins, high molecular weight glycoproteins, colony stimulating factor 1, secreted phosphoprotein 1 (SPP1), integrins, FGF7, FGF10, HGF, stanniocalcins, and transforming growth factors beta-1, -2 and -3, nitric oxide synthase, GTP cyclohydrolase 1 (GCH1), tetrahydrobiopterin (BH4), and interleukins 1 and 4. The roles of many of these proteins remain to be determined. Nevertheless, they contribute to a uterine microenvironment that supports growth and development of the conceptus.

2.4 Implantation of Blastocysts in Humans, Sheep, Pigs, and Rodents

2.4.1 Implantation of Blastocysts in Mammals

Implantation of the blastocyst in mammals is the process of attachment of trophoctoderm to uterine luminal epithelium (LE) and, in some

species, invasion of the blastocyst into the uterine endometrium. Implantation is a prerequisite for placentation that begins later in gestation (McGowen et al. 2014). The two primary classifications of implantation in mammals are based on the extent to which the blastocyst invades into the uterine endometrium. Central-type or superficial implantation (pig, horse, sheep, and cow) does involve attachment of trophoctoderm to the uterine LE, but not invasion into the endometrium. Interstitial attachment involves invasion and embedding of the blastocyst entirely within the uterine endometrium (rodents and primates). The implantation cascade has up to five stages: (1) shedding of the zona pellucida from the blastocyst; (2) pre-contact and orientation of the blastocyst; (3) apposition of trophoctoderm and uterine LE; (4) adhesion of trophoctoderm to uterine LE; and (5) invasion of the blastocyst into the endometrium in species with interstitial implantation.

2.4.2 Implantation in Humans

There is a well-defined “window of implantation” in women during which the uterus is receptive to the blastocyst for the initiation of implantation (Su and Fazleabas 2015; Kim and Kim 2017). That window of implantation is during the mid-secretory phase of the menstrual cycle, specifically cycle Days 20–24 (6–10 Days after ovulation). Markers of uterine receptivity to implantation in humans include: (1) pinopods or uterodomes that are hairlike microvilli of epithelial cells which transiently fuse to form a single flowerlike membrane projection only on the luminal surface of endometrial epithelial cells during the window of implantation; (2) epithelial plaques that are an endometrial response in primates to implantation of the blastocyst involving transformation of uterine LE and sGE epithelia as they undergo hypertrophy, hyperplasia, and form a rounded acinar multicellular pad; (3) down-regulation of expression of receptors for estradiol (ESR1) and progesterone (PGR) in uterine epithelia; (4) decrease in expression of MUC1 by uterine LE; (5) expression of the integrins $\alpha 1\beta 1$,

$\alpha 4\beta 1$, and $\alpha v\beta 3$ by uterine LE/sGE; (6) increased expression and secretion of SPP1 by uterine epithelia; and (7) expression of heparin-binding epidermal growth factor (HBEGF) by uterine LE and the surface of pinopods. Implantation occurs in three stages. First, the blastocyst comes into apposition with the uterine LE, then trophoblast attaches to the uterine LE, and finally the invasive trophoblast cells cross the endometrial epithelial basement membrane and invade into the uterine endometrium.

Trophoblast cells penetrate the uterine LE via gaps between cells to reach the basement membrane, but without destroying the uterine LE (Carson et al. 2000). Formation of thin folds of trophoblast cells between uterine LE is followed by degradation of the basement membrane and extracellular matrix (ECM), allowing trophoblast cells to be in close contact with the endometrial stromal cells. Activated matrix metalloproteinases (MMPs) play a primary role in degrading matrices during this process, and various integrins guide the invading trophoblast through different layers of cells and matrices within the endometrium. Next, trophoblast cells that migrate into the endometrium and continue to proliferate, differentiate, and fuse to become the multinucleated syncytiotrophoblasts (STB). The other trophoblast cells, those that surround the inner cell mass, are mononuclear cytotrophoblasts (CTB). STB cells guide invasion of the blastocyst into the endometrium until it is completely embedded within the endometrial stroma, 8 days after ovulation. The site of entry of the invading blastocyst is covered by fibrin that also supports growth of endometrial epithelial cells to cover the site of implantation.

The STB layer has fluid-filled spaces known as lacunae separated by trabeculae, resembling a sponge. As the STB contacts maternal blood vessels, maternal blood is trapped within the lacunae for transfer of oxygen and nutrients to the developing conceptus. CTB grow into the trabeculae formed by invading STB to form primary chorionic villi that initiate placentation. The uterine stroma at the site of implantation undergoes decidualization to form three areas of the decidua in humans during pregnancy. The

area of decidua directly beneath the site of implantation is the decidua basalis, the region that overlies the developing conceptus and separates it from the uterine cavity is the decidua capsularis, and the remaining decidua is the decidua parietalis. The decidua basalis and the decidua capsularis are invaded by trophoblast cells and chorionic villi of the conceptus, but only the decidua basalis supports formation of the discoid placenta in mid- to late-pregnancy as the rest of the decidua degenerates later in pregnancy.

2.4.3 Implantation in Rodents

As for humans, there is a “window of implantation” in mice when the uterus is receptive to supporting growth, attachment, and implantation of the blastocyst. P4 and E2 are critical for implantation in mice as they regulate proliferation and/or differentiation of uterine cells in a time and cell-specific manner that is required for uterine receptivity to implantation of the blastocyst (Cockburn and Rossant 2010; McGowen et al. 2014; Aplin and Ruane 2017; Matsumoto 2017). E2 from preovulatory follicles induces proliferation of uterine epithelial cells and then, post-ovulation, P4 from the CL induces proliferation of stromal cells from Day 3. The uterus becomes receptive to implantation on Day 4 in response to an acute increase in E2. Attachment of blastocyst trophoblast to uterine LE on Day 4 of pregnancy results in proliferation of stromal cells surrounding the implanting blastocyst and then the stromal cells undergo full decidualization. The receptive phase of the uterus for implantation is only approximately 24 h, therefore the processes governing implantation must be tightly regulated to ensure implantation occurs during this short time.

Blastocysts are found in uterine crypts on the anti-mesometrial side of the uterine lumen, and the uterine lumen then closes to confine the blastocyst to a limited space within the uterine lumen called the implantation chamber (Fig. 2.3). The tight space formed by the implantation chamber restricts blastocyst

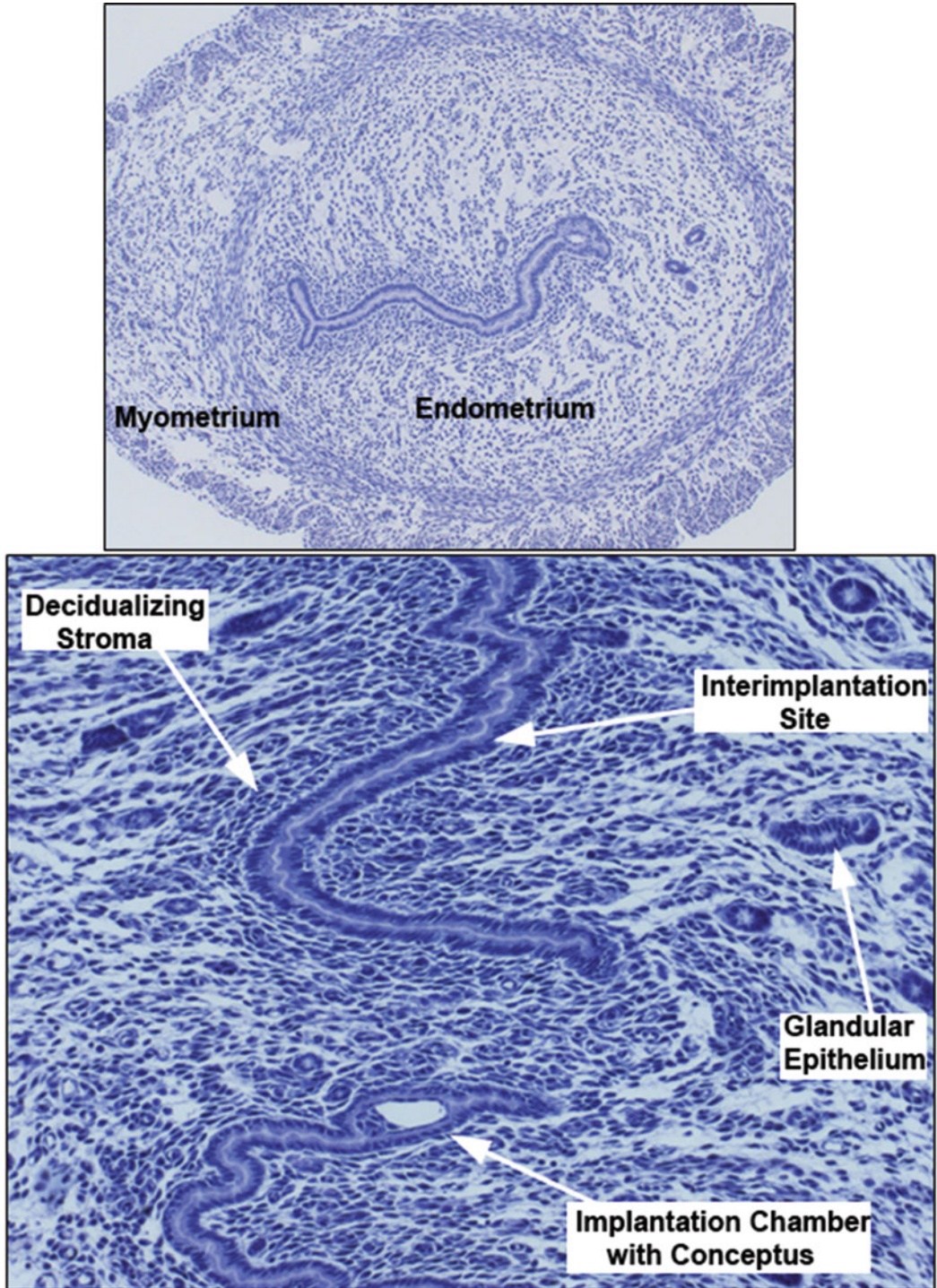


Fig. 2.3 Attachment of the mouse blastocyst to the uterine luminal epithelium (LE). Shown are mouse blastocysts within implantation chambers at the initiation of implantation. Closure of the uterine lumen at interimplantation sites brings the blastocyst into close apposition to the uterine LE, and interaction of the blastocyst with the LE elicits the beginning of a decidual response within the uterine stroma. Decidualization begins

following blastocyst adhesion, but prior to LE degradation for implantation into the uterine wall. Pregnancies were produced using delayed implantation so that the presence of implantation chambers could be accurately predicted. Unpublished work of Kramer AC, Erikson DW, McLendon BA, Seo H, Hyashi K, Spencer TE, Bazer FW, Burghardt RC, Johnson GA

movement and facilitates close apposition of the apical surfaces of trophoblast cells to endometrial LE cells. The integrity of the implantation chamber is maintained via closure of the lumen surrounding the chamber. The mechanisms regulating the closure of the uterine lumen at inter-implantation sites in mice are not completely understood, but likely involve absorption of fluid within the uterine lumen, mediated by aquaporins expressed by the endometrium (Richard et al. 2003; Beall et al. 2007; Chan et al. 2009; De Oliveira et al. 2020). The next phase involves invasion of the blastocyst into the uterine endometrium, which is mediated by expression of genes required for remodeling the endometrium. MMPs are zinc-dependent endopeptidases that breakdown ECM proteins. The MMPs most important to invasion are those with gelatinase activity (MMP2 and MMP9). MMP9 breaks down collagen type IV of the endometrial basal membrane. Serine proteases, including urokinase-type plasminogen activator (UPA) and tissue-type plasminogen activator (TPA) convert plasminogen to plasmin that accounts for proteolytic degradation of the ECM during implantation. During the invasion phase of blastocyst implantation, uterine decidual cells express transforming growth factor beta (TGFB) that plays a key regulatory role to limit the extent of invasion by increasing expression of tissue inhibitors of MMPs (TIMPs) and plasminogen activator inhibitor (PAI). Decorin, a TGFB binding proteoglycan, inhibits proliferation, migration, and invasiveness of human extravillous trophoblast cells and limits migration of mouse trophoblast cells via a mechanism that appears to be inhibitory to plasminogen activator activity (Strickland et al. 1976).

2.4.4 Implantation in Sheep

After fertilization of a sheep oocyte within the oviduct, the resulting one-cell zygote undergoes cleavage divisions to the 8–16 cell stage when activation of the embryonic transcriptome occurs (Johnson et al. 2018). The 32- to 64-cell morula remains enclosed in the zona pellucida and

leaves the oviduct to enter the uterus on Day 3 or 4 of pregnancy to continue to develop to a blastocyst by Day 6 of gestation. The blastocyst includes the embryonic disc that will give rise to the embryo/fetus with ectoderm, endoderm, and mesoderm, trophoblast that will form the chorion of the placenta, a blastocoel or primitive gut, and extra-embryonic endoderm and mesoderm. The sheep blastocyst hatches from the zona pellucida between Days 8 and 9 of gestation and expands to 400–900 μm in diameter (Spencer et al. 2004). The hatched blastocyst then undergoes a rapid morphological transition called elongation to first a tubular form (10–22 mm) on Day 12, followed by rapid growth and elongation to filamentous forms of 100 mm in length on Day 14, and 250 mm in length on Day 16 before trophoblast extends into the contralateral uterine horn between Days 18 and 20 of pregnancy (Spencer et al. 2004). Prior to conceptus attachment, the conceptus is reliant entirely on the secretions of water, amino acids, hexose sugars, ions, growth factors, hormones, enzymes, cytokines, mitogens, and vitamins (collectively referred to as histotroph) by the uterine LE, sGE, and GE (Bazer et al. 2015a). Conceptus elongation rapidly increases the surface area of contact between trophoblast and uterine LE for exchange of nutrients and gasses, maximizing paracrine effects of the conceptus to prevent regression of the CL (luteolysis), and signaling pregnancy recognition via IFNT.

Implantation in sheep occurs as the trophoblast of the filamentous conceptus apposes and then adheres to uterine LE by Day 14 of pregnancy (Johnson et al. 2018). Apposition begins near the inner cell mass and moves toward the ends of the elongated conceptus. By Day 16, the conceptus trophoblast is firmly attached to uterine LE with significant interdigitation between microvilli on uterine LE, and conceptus trophoblast cells. There are also papillae of trophoblast that extend into the mouths of uterine glands to take up nutrients and exchange gasses, e.g., oxygen and carbon dioxide. Attachment of the conceptus to both the caruncular and intercaruncular regions of the endometrium is complete by Day 22 of pregnancy. Attachment

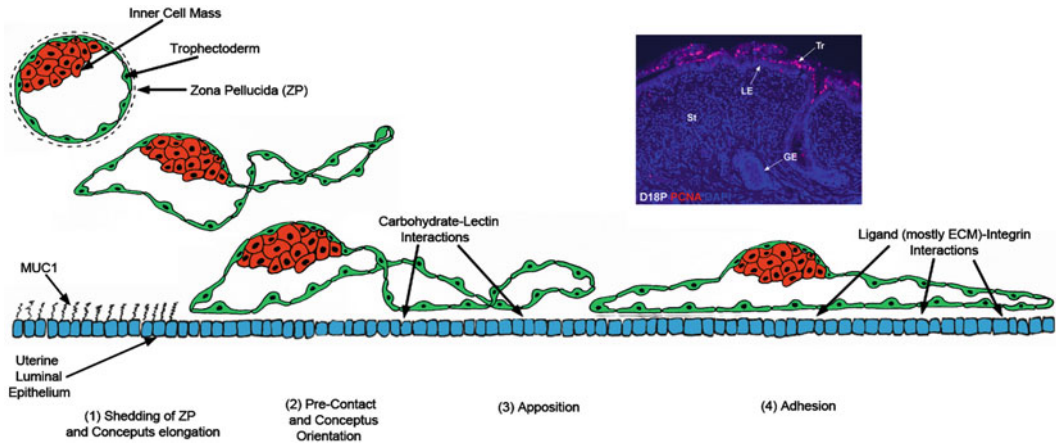


Fig. 2.4 The initial stages of implantation are common across species and are characterized as the “Adhesion Cascade for Implantation”. The phases of this adhesion cascade in pigs include (1) elongation of the conceptus trophoctoderm and shedding of the zona pellucida; (2) down-regulation of MUC1 at the apical surface of uterine LE to expose potential, but not yet identified, low affinity carbohydrate-lectin binding molecules to mediate pre-contact and conceptus trophoctoderm orientation to the uterine LE; (3) low affinity contacts are then replaced by a more stable and extensive repertoire of adhesive interactions between integrins and maternal ECM to

mediate apposition of trophoctoderm to LE; and (4) integrin receptors expressed at the apical surface of uterine LE cells bind to Arg-Gly-Asp (RGD) and non-RGD amino acid sequence-containing ECM molecules and bridge to another complement of potential integrin receptors expressed at the apical surface of conceptus trophoctoderm cells to mediate conceptus trophoctoderm adhesion. Immunofluorescence staining for PCNA (red) illustrates that the conceptus trophoctoderm (Tr) proliferates, but the uterine luminal epithelium (LE) does not proliferate during the peri-implantation period of sheep

and the adhesion cascade for implantation in sheep involves down-regulation of MUC1 across the entire endometrial surface to unmask glycosylation dependent cell adhesion molecule 1 (GLYCAM1), LGALS15, and SPP1 for interactions with lectins and integrins (Fig. 2.4). Initial attachment is likely mediated by GLYCAM1 and LGALS15, and firm attachment is likely mediated by SPP1. Integrins are constitutively present on uterine LE and conceptus trophoctoderm during the peri-implantation period when expression of LGALS15 is induced by P4 and further increased by IFNT, and expression of SPP1 is induced by P4 (Johnson et al. 2000, 2014).

2.4.5 Implantation in Pigs

Pig embryos enter the uterus at the four-cell stage, reach the blastocyst stage by Day 5 of pregnancy, hatch from the zona pellucida between Days 6 and 7, and expand to 2–6 mm

diameter spherical embryo by Day 10 of gestation (Fig. 2.5) (Bazer and Johnson 2014). Pig blastocysts then undergo rapid morphological transition from spherical to tubular and elongated filamentous forms between Days 10 and 12 of pregnancy at a rate of about 0.25 mm/h between the early spherical blastocyst stage and 4–9 mm diameter spherical blastocyst stage. The rate of conceptus elongation significantly increases to 30–45 mm/h from the 10 mm blastocyst to the 200 mm long filamentous conceptus due to increased cellular hypertrophy. As the mitotic index of spherical blastocysts is greater than for tubular blastocysts, but cellular hyperplasia does not account for initial elongation of pig blastocysts. Once the blastocyst reaches 10 mm in diameter, the conceptus begins to undergo the rapid morphological changes in both trophoctoderm and extra-embryonic endoderm. A dense band of cells (the elongation zone) containing both endoderm and trophoctoderm extends from the inner cell mass (ICM) to the tip of the ovoid

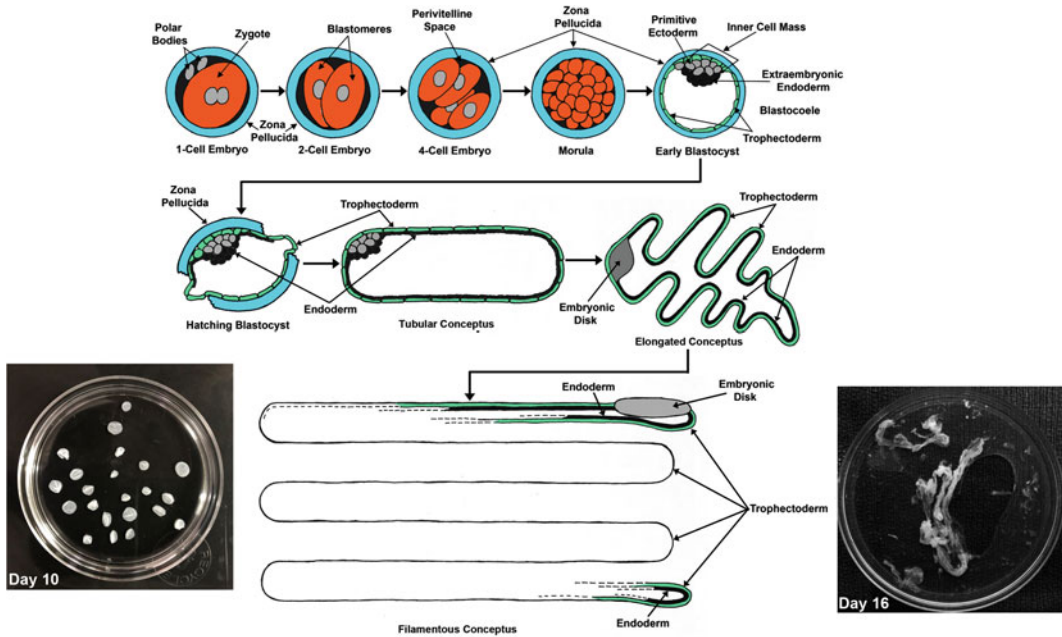


Fig. 2.5 Pig embryos undergo cell divisions, enter the uterus at about the 4-cell stage, hatch from the zona pellucida around Day 7, reach the expanded blastocyst stage around Day 10 and then change rapidly in morphology from spherical to tubular to filamentous forms to achieve maximum area of surface contact between the trophoblast and uterine luminal epithelium. The insets are of spherical blastocysts from Day 10 and filamentous conceptuses on Day 16 of pregnancy. As

spherical pig blastocysts expand there are increases in proliferation and migration of trophoblast and extraembryonic endoderm cells toward the inner cell mass (ICM). This process of elongation of the conceptus results in central-type implantation initially and then the development of true epitheliochorial placenta later in gestation. Reprinted from the freely available article of Johnson et al. (2018)

blastocyst. Following formation of the elongation zone, additional rapid elongation of the 100–200 mm long pig conceptus occurs to form a conceptus of 800–1,000 mm in length by Day 16 of pregnancy. These morphological changes primarily occur due to alterations in microfilaments and junctional complexes of trophoblast cells and formation of filopodia by endodermal cells. The second period of elongation involves cellular hyperplasia and each conceptus within the litter achieves maximum surface area for contact between trophoblast and uterine LE to facilitate uptake of nutrients from uterine LE and GE. Increasing surface area of the conceptus;uterine interface is a critical adaptation in the pig, which exhibits a minimally invasive epitheliochorial placentation, to maximize nutrient and oxygen transport to the fetal-placental tissues.

Increased cellular density of both extraembryonic endoderm and trophoblast in tubular blastocysts results in the formation of a thin cell-dense band approximately 1–2 mm wide extending from and in the same plane as the embryonic disc to the end of the trophoblast. The endoderm cells outside this thin band are sparsely populated and make cellular contact only through filopodia. The dense band of extraembryonic endoderm and trophoblast forms the elongation zone that decreases in width as elongation progresses but continues to extend along the entire length of the conceptus trophoblast. Histologically, it has been demonstrated that the trophoblast cells present in the elongation zone are columnar in shape as compared to cuboidal trophoblast cells in areas peripheral to the elongation zone. This structural modification is associated with changes in length

and orientation of microfilaments as early as the 10 mm stage of blastocyst development. Within the elongation zone, extension of filopodia from extra-embryonic endodermal cells in conjunction with alterations in microfilaments and junctional complexes of trophoblast cells allows the movement and redistribution of cells toward the ends of tubular blastocysts. While the actin cytoskeleton initially exhibits a pericellular distribution, this later becomes a continuous actin-rich lateral border with stress fibers along the basal surface in the filamentous conceptus. The actin cytoskeleton, in association with myosin II, has a crucial function in generating the force required for conceptus elongation as constricted regions along the length of filamentous conceptuses contain polarized trophoblast cells with a distinct F-actin array. The orientation of microfilaments within the trophoblast changes from horizontal to parallel relative to the lateral cell borders likely due to a complex cellular response to torsional forces generated by the elongation process and mediated through transmembrane integrin receptors and the focal adhesions they assemble. Heterodimeric transmembrane integrin receptors [e.g., ITGA5:ITGB1 ($\alpha 5\beta 1$)] are the major components of focal adhesions. They transmit diverse signals between the ECM components, such as SPP1 and the actin cytoskeleton, to regulate cellular growth, proliferation, survival, and migration. Additionally, these focal adhesions alter gene expression and the morphology of trophoblast and extra-embryonic endoderm in elongating pig conceptuses. The process of conceptus elongation likely involves several cell signaling pathways with serine-threonine kinases such as insulin growth factor 2 acting via receptor tyrosine kinases, integrin heterodimer-ECM complexes (e.g., SPP1-ITGA5:ITGB1 and/or SPP1-ITGA5:ITGB1), and arginine acting simultaneously and independently to stimulate mechanistic target of rapamycin 1 (mTORC1) and/or mTORC2 required for proliferation, migration, cytoskeletal reorganization, and adhesion of trophoblast cells to uterine LE.

2.5 Overview of Placentation/Placental Growth and Function in Humans, Sheep, Pigs, and Rodents

The primary functions of the placenta are transplacental exchange of gases, micronutrients (amino acids, glucose) and macromolecules (proteins), production of hormones, and production of cytokines and other regulatory molecules that affect growth and development of the conceptus. Placental efficiency is achieved as maternal and fetal-placental vasculatures are brought into close apposition to allow for transplacental exchange of molecules while maintaining separation of the maternal and fetal circulatory systems. Endometrial and placental tissues are remodeled to achieve areas with reduced interhaemal distances regardless of whether the placenta is epitheliochorial, synepitheliochorial, endotheliochorial, or hemochorial to maximize transplacental exchange of gasses, micronutrients, and macronutrients.

2.5.1 Placentation in Humans

Following implantation of the human blastocyst, the primary syncytium invades into the uterine stroma and forms fluid-filled spaces called lacunae that enlarge and merge to form a system of trabeculae (Soares et al. 2018; Turco and Moffett 2019). The syncytium erodes into the uterine glands to become bathed in their secretions. Trophoblast cells beneath the syncytium are CTB cells that proliferate and form villi that penetrate through the STB to form primary villi with a CTB core and outer STB. The villi undergo further proliferation and branching, and the lacunae become the intervillous space. CTB cells penetrate through the primary syncytium and merge laterally to surround the conceptus in a continuous CTB shell between the villi and the decidua. The blastocyst then has three layers: inner chorionic plate in contact with the intervillous space; villi separated by the intervillous

space; and the CTB shell in contact with the decidua. On Days 17–18 of pregnancy, extra-embryonic mesenchymal cells penetrate through the villous core to form secondary villi and soon thereafter fetal capillaries develop within the core of tertiary villi. The villous tree continues to enlarge through branching from the chorionic plate to form a system of vascularized villous trees. The CTB shell is in contact with uterine decidual cells and individual CTB cells invade into decidua as extravillous trophoblast via a process similar to that for an epithelial-mesenchymal transition.

The STB of placental villi are in direct contact with uterine gland secretions and maternal blood flowing into the intervillous space for maternal/fetal exchange of gases and nutrients supporting growth of the conceptus. The STB microvilli express receptors for growth factors and hormones and transporters for amino acids and glucose. They also secrete hormones and proteins into the maternal circulation to influence physiological and metabolic adaptations to pregnancy. The STB provides a protective immunological barrier as it does not express human leukocyte antigen (HLA) molecules that would otherwise subject it to immunological rejection.

With advancing development of the placenta, the CTB shell becomes discontinuous and CTB cells form columns that emerge from the anchoring villi in contact with the decidua. These extravillous trophoblast (EVT) cells migrate into the decidua along two differentiation pathways: the interstitial EVT (iEVT) cells migrate through the decidual stroma toward the maternal spiral arteries, while the endovascular trophoblast EVT (eEVT) cells migrate into the spiral arteries to displace endothelial cells and ensure maximum dilation and blood flow. The iEVT invade as far as the inner one-third of the myometrium and fuse to form a bed of placental giant cells. After the arterial transformation occurs, the eEVT move in a retrograde manner down the artery to form a plug that prevents blood flow into the intervillous space until the full hemochorial circulation is established. As a result of trophoblast plug, the placenta develops in a low oxygen

environment during the first trimester. In humans, the yolk and allantoic sacs undergo regression. Therefore, the chorioamniotic placenta contains an abundance of amniotic fluid in which the fetus develops. The human placenta is hemochorial as the chorion is in direct contact with maternal blood for transplacental transport of nutrients and exchange of oxygen and carbon dioxide.

2.5.2 Placentation in Rodents

During implantation, trophoblast attachment to uterine LE induces differentiation of uterine stromal cells into decidual cells followed by complete penetration of the blastocyst into the decidualized uterine stroma (Picut et al. 2009; Soares et al. 2018; Furukawa et al. 2019). As hemochorial placentation progresses in rodents, there is the maternal interface and the fetal interface determined by the extent to which extra-embryonic mesenchyme and associated vasculature penetrate into the trophoblast compartment. The region that includes trophoblast and extra-embryonic mesenchyme forms the labyrinth zone of the placenta in mice and rats. Labyrinth and villous trophoblast compartments include layers of STB. Trophoblast cells extend beyond the trophoblast-extra-embryonic mesenchyme admixture are at the maternal boundary and arranged into the junctional zone and extravillous trophoblast columns, respectively. As gestation advances, invasive trophoblast cells arise from the junctional zone to form extravillous trophoblast columns that migrate into the uterine parenchyma. There are two types of invasive trophoblast cells, interstitial and endovascular. Interstitial invasive trophoblast cells coalesce between the uterine vasculature, whereas endovascular invasive trophoblasts infiltrate uterine blood vessels, especially arteries/arterioles, and replace the vascular endothelium as in humans. During invasive trophoblast cell differentiation, there are changes in expression of integrins that alter interactions with surrounding ECM. As endovascular invasive trophoblast cells differentiate, they acquire an

endothelial cell phenotype. For rats, there is deep intrauterine trophoblast cell invasion, but it is nominal for trophoblast cells migrating into the mouse uterine parenchyma. Cellular constituents of the maternal uterine interface, including decidual cells, endometrial glands, and immune/inflammatory cell populations, influence behavior of trophoblast cells.

Rodents have a chorioallantoic placenta and its formation is highly dependent of the ectoplacental cone that is a critical generative zone. The ectoplacental cone trophoblast is considered cytotrophoblastic and develops from the polar trophoblast covering the embryonic disc. Mesenchyme invades the ectoplacental cone leading to a division between the main functional exchange area, the labyrinth, and the superficial zone, the remnant of the ectoplacental cone, and the trophospongium or basal zone. There is maternal blood flow through the ectoplacental area before the labyrinth is formed to derive nutrition from the maternal circulation. During and after labyrinth formation, the trophospongium undergoes differentiation into secondary giant cell formation (primary giant cells are derived from the mural trophoblast developing in relation to the yolk sac) and are restricted to the zone immediately facing maternal tissues. Most of the trophospongium differentiates into islands of glycogen cells surrounded by basophilic trophoblast in contact with maternal blood.

The fully formed placenta includes the transient yolk sac, amnion, and chorioallantois with functions described previously. In addition, outside the placental membranes and between the chorion and metrial gland, there is the labyrinth, trophospongiosum or basal zone, and uterine decidua. The labyrinth is the largest layer of the placenta and the site for most, if not all, nutrient and gas exchange between the maternal and fetal-placental vasculatures. The basal zone forms just below the labyrinth zone and is composed of spongiotrophoblasts, glycogen cells, and (secondary) trophoblastic giant cells. The primary trophoblastic giant cells derive from the mural trophoctoderm and are important for implantation. The secondary trophoblastic giant cells form from the ectoplacental cone and

represent the main components of the basal zone. The basal zone is a site of production of steroids and peptide hormones required for the maintenance of pregnancy, storage of glycogen, and establishment of an immunological barrier to the maternal immune system. Metrial glands are located in the mesometrial triangle of the pregnant uterus from gestational Day 8 to parturition.

The uterine metrial gland is a distinct structure in the uterus that is composed of granulated metrial gland cells, endometrial stromal cells, trophoblast cells, blood vessels, and fibroblasts. Granulated metrial gland cells are hallmark cells of the metrial gland derived from bone marrow. They are perforin-positive, natural killer cells that proliferate in the pregnant uterus and encircle newly formed blood vessels in the mesometrial triangle, producing proteases that destroy basement membranes and vascular endothelial growth factor to stimulate endothelial cell proliferation. The metrial gland cells promote angiogenesis and remodel the uterine vasculature at the point of entry of blood vessels into the uterus.

2.5.3 Placentation in Sheep

Implantation is a prerequisite for placentation, and both are critical for a successful pregnancy. Conceptus attachment and adhesion to uterine LE/sGE first requires removal of large mucins from the glycocalyx that block direct physical interactions between carbohydrates and lectins at the apical surfaces of the opposing uterine LE and conceptus trophoctoderm (Bazer et al. 2012; Johnson et al. 2018). These low affinity contacts are replaced by firm focal adhesions between integrins and ECM proteins like SPP1. Sheep have a synepitheliochorial placenta in which fusion of conceptus trophoctoderm with uterine LE occurs and then the uterine LE is degraded. Both mononuclear trophoctoderm cells and multinucleated trophoblast giant cells (TGCs) are present in the trophoctoderm of ruminant placentae. The mononuclear cells constitute the majority of the trophoctoderm cells and TGCs differentiate from the mononuclear trophoctoderm cells in concert with

trophectoderm outgrowth during conceptus elongation (Seo et al. 2019; Seo et al. 2020a). TGCs first appear between Days 14 and 16 of gestation in sheep conceptuses and comprise 15–20% of the trophoctoderm during the apposition and attachment phases of implantation. TGCs migrate to LE and remove LE cells that are undergoing apoptosis to form multinucleated syncytia. The syncytia of sheep subsequently enlarge through continued TGC migration and fusion to form syncytial plaques. The syncytial plaques form the epithelial interface between endometrial caruncles and placental cotyledons that comprise the placentomes. Syncytial plaques are a consistent feature in placentomes throughout pregnancy in sheep.

Fetal fluids (allantoic and amniotic fluids) are of maternal origin via active transport of water, as well as other molecules, across the placenta and into the allantoic sac for distribution to other components of the conceptus including the fetus and amniotic sac. The driving force for expansion of the allantois, and in turn the chorioallantois, is the rapid accumulation of water in the allantoic sac from about 1 ml on Day 18 to 90 ml on Day 40 and then from Day 70 (32 ml) to Day

140 (438 ml) of the 147 day period of gestation. Similarly, amniotic fluid volume increases throughout gestation in sheep from 2 ml on Day 30 to over 700 ml on Day 140 of gestation. Amniotic fluid buoys the fetus to allow it to develop symmetrically, prevents fetal skin from adhering to the amnion and it is swallowed by the fetus in the last one-third of gestation to provide water, minerals, and other nutrients.

Development of placentomes begins to occur Days 25–30 of gestation (Fig. 2.6). The highly branched villous placental structures termed cotyledons protrude into crypts in the maternal endometrial caruncles (aglandular areas of endometrium consisting of stroma covered by a single layer of epithelium). As the cotyledonary chorioallantoic villi interdigitate extensively with endometrial caruncles there is, within the placentomes, opposing vascular beds that provide a large surface area for active transfer of nutrients and gases from maternal blood to the fetal-placental vasculature. Consequently, there is a high correlation between the placentomal mass and fetal weight at birth. In contrast, there is epitheliochorial attachment to uterine LE in inter-

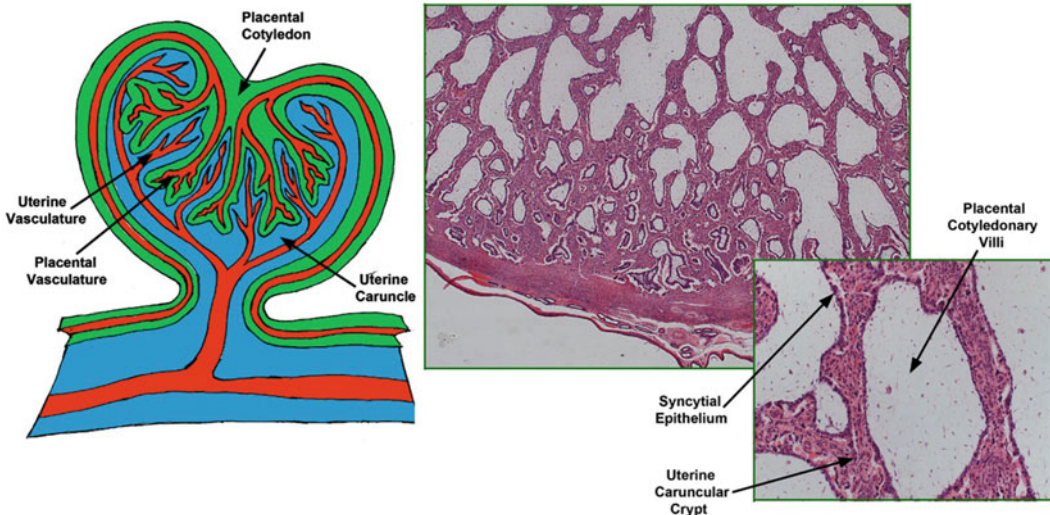


Fig. 2.6 Overview of placental development in the sheep. Illustration describing placentome structure that indicates the uterine caruncle in blue, placental cotyledon in green, and the network of blood vessels in red. Collectively, this is the placentome that provides sites for the exchange of gases and micronutrients such as glucose

and amino acids between the vascular systems of the fetal-placental tissues and maternal vascular system. The figure on the right is a histological section of a placentome with the various cellular components of the placentome. Reprinted from the freely available article of Johnson et al. (2018)

placentomal regions of the placenta. The interplacentomal chorioallantois contains areolae that are in direct apposition to openings of the mouths of uterine glands for direct uptake of components of histotroph secreted by or transported by uterine GE. The components of histotroph are transported across the areolae and into the fetal-placental vasculature via fluid-phase pinocytosis.

2.5.4 Placentation in Pigs

The elongated conceptuses in pigs expand through the accumulation of water initially within the yolk sac and then the allantois of the chorioallantoic placenta as described for sheep (Knight et al. 1977; Bazer and Johnson 2014). The yolk sac derives from an evagination of the embryonic foregut and accumulates fluid that first brings the trophoblast into apposition with the uterine wall (between Days 17 and 22 of gestation in pigs) for absorption of nutrients. After Day 22, the yolk sac becomes a vestigial structure. The allantoic sac forms as an evagination of the hindgut and expands rapidly as it fills with allantoic fluid between Days 18 (1 ml) and 30 (250 to 300 ml) of gestation to fill the extra-embryonic coelom and establish the chorioallantoic placenta. Allantoic fluid then decreases to about 50 ml on Day 40 of gestation and then increases again to around 450 ml on Day 55 of gestation. By Day 70 of gestation in pigs, development of the epitheliochorial placenta is considered complete based on placental weight, surface area, and numbers of placental areolae. Amniotic fluid serves the protective roles for the embryo/fetus in pigs as described for sheep. Amniotic fluid volume increases from around 2 ml on Day 20 to 200 ml on Day 70 of gestation and then decreases to term.

The chorioallantoic placenta attaches directly to uterine LE for hematrophic and histotrophic support of conceptus growth and development. Given the non-invasive nature of the pig placenta, it is critical to increase the surface area available at the uterine (endometrial)-placental (chorioallantoic) interface to minimize the distance between maternal and placental micro-vasculatures,

thereby optimizing the transport of nutrients and gasses from maternal to placental blood vessels for eventual utilization by the embryo/fetus. To do this, extensive remodeling occurs at the uterine-placental interface by the formation of chorionic (placental) ridges that correspond with endometrial invaginations that result in extensive folding (Fig. 2.7). The interface between the endometrium and chorion in pigs begins to undergo folding between Days 20 and Day 25 of pregnancy. By Day 30 of pregnancy the chorioallantoic and endometrial surfaces interlock into folds composed of endometrial ridges and chorioallantoic troughs (Friess et al. 1980). These folds proceed to increase in length until Day 35 of gestation, followed by a second increase in length between Days 50 and 60 of gestation (Seo et al. 2020b). As the growth rate of the placenta decreases, the fetus undergoes a period of exponential growth (Marrable 1971). It is critical that the depth of the folds increases between Days 65 and 105 of gestation, to increase the surface area available for nutrient transport to accommodate the high nutritional demands of the exponentially growing fetus (Vallet and Freking 2007). The morphological folding characteristic of the epitheliochorial placentation in pigs is likely the result of mechanotransduction and mechanosensation at the interface between the endometrium and the chorion. It has been proposed that dilation of subepithelial uterine blood vessels delivers increased blood flow that pushes upward on the interface between the uterine LE and the placental chorioallantois. These protrusive forces from growing uterine blood vessels trigger integrin adhesion complex assembly and actin polymerization between the uterine LE and chorionic epithelium (CE) at the bottoms of the chorioallantoic troughs, and uterine fibroblasts differentiate into contractile myofibroblasts that pull the connective tissue downward and inward to sculpt folds at the uterine-placental interface (Seo et al. 2020b). The folding increases the surface area of the uterine-placental interface for each conceptus in the litter of piglets. Indentation of uterine LE and CE by underlying capillaries reduces the diffusion distance between the maternal and fetal-placental vasculatures. Indeed, placental and

uterine capillaries lie immediately beneath the uterine LE and the chorionic epithelium, minimizing the distance between maternal and fetal blood vessels (Dantzer and Leiser 1994). In summary, the lateral sides and tops of the chorioallantoic ridges are designed for gaseous exchange, whereas the base of the chorioallantoic troughs is designed for the transport of blood-borne nutrients, i.e., hemotroph (Friess et al. 1980). The precise cell-specific spatio-temporal regulation of nutrient transporters is essential for the regulation of fetal growth and development. For example, at Day 60 of gestation the glucose transporter SLC2A1 is expressed by the uterine

LE and in the CE but not by the tall columnar CE cells at the tips of the uterine-placental folds and the areolae (Kramer et al. 2020). In contrast, at Day 60 of gestation, the glucose transporter SLC2A3 is expressed by the CE of the areolae and the LE cells in close proximity to the tall columnar cells of the CE, and SLC2A8, a glucose and fructose transporter, is expressed by the tall columnar cells of the CE and by the areolae. Together, these findings suggest that differential expression of transporters for glucose across the uterine-chorionic folds is critical for the transportation of glucose from maternal circulation to the fetus.

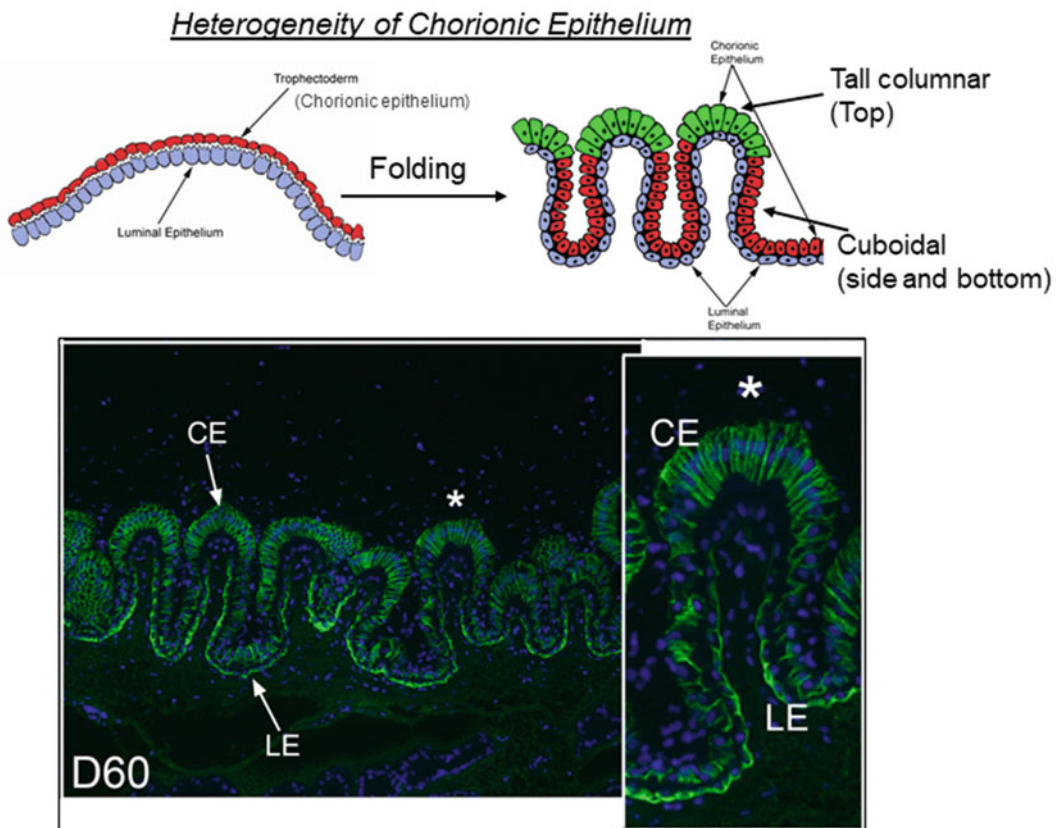


Fig. 2.7 Overview of placental development in the pig. An illustration depicting the uterine-placental interface during implantation (top left panel) and placentation (top right panel). Green and red colors indicate heterogeneity of gene expression within the chorionic epithelium. Immunofluorescence staining for $\alpha 2\beta 1$ integrin by uterine

epithelia on Day 60 of pregnancy is shown (bottom panel). The asterisk indicates a fold or villus with the apposition of uterine luminal epithelium (LE) and chorionic epithelium (CE) that significantly increases the surface area for exchange of nutrients and gases between the fetal-placental and maternal vascular systems

Progressive interdigitation of microvilli on trophoderm and uterine LE eventually occurs over the entire uterine-placental interface, except at the openings of uterine glands. At openings of the mouths of uterine glands, the CE forms areolae to transport components of histotroph into the fetal-placental vasculature via fluid-phase pinocytosis. Areolae are initially observed as small white circular discs with a prominent peripheral thickening of 1 mm in diameter (Friess et al. 1981), but quickly develop to cover the openings of the uterine gland(s). The cavity that forms collects the secretions of the uterine glands, and the columnar chorionic epithelial cells that line the placental border of this cavity form a seal between the uterine LE and the walls of the placental areola to prevent dissipation of histotroph into inter-areolar regions of the placenta (Fig. 2.8). The allantoic vasculature that receives the histotroph is clearly discernible from the vasculature that supplies inter-areolar

regions of the placenta (Leiser and Dantzer 1994). The endometrial vasculature that supplies the areola develops more slowly than the endometrial vasculature of inter-areolar regions, presumably due to a less intimate association with the trophoderm. This prevents direct physical interaction between the trophoderm and endometrium and decreases the influence of paracrine products that are secreted by the trophoderm. As the placenta grows, areolar diameter increases and a stretching of the areolar capillary network leads to a progressively widening size. During the early stages of placentation, the placental surface of the areolae is flat, but as placentation progresses the flat surface becomes more complex with formation of ridges and papilla-like structures lined by a columnar chorionic epithelium (Amoroso 1952). The balloon shape of the areola implies that there is an interior pressure against the chorioallantoic surface of the areola delivered by the continuous

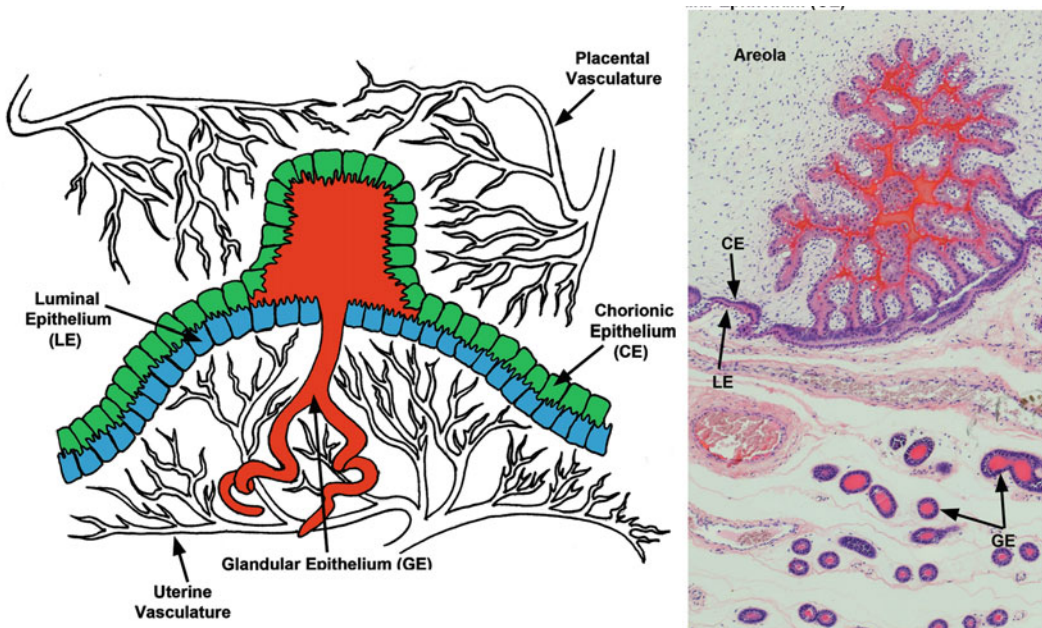


Fig. 2.8 Areolae structure in the pig. Illustration depicting an areola that exists in placentae of species such as pigs, horses, sheep, cattle, and goats for the transport of secretions from uterine glands into the fetal-placental vasculature via fluid-phase pinocytosis. Nutrients and gases are transported from the maternal capillaries into the placental capillaries. The hematoxylin and eosin stained

image in the right panel illustrates the uterine-placental interface of mature placentation in the pig, with the areola having a critical function for histotrophic support of the fetus. The red staining indicates the synthesis, secretion, and transport of histotroph by the glands and into the lumen of the areola

accumulation of histotroph from the uterine glands. Indeed, the cavity of an areola is a small reservoir for the histotroph that is potentially secreted by the much larger uterine glands (Leiser and Dantzer 1994). There are some 2,500 areolae per placenta in pigs and a correlation between areolar number and fetal weight has been suggested.

Uteroferrin (UF, also known as acid phosphatase 5, tartrate resistant, ACP5) secreted by uterine GE is taken up by placental areolae by fluid-phase pinocytosis and released into the fetal-placental circulation. UF transports iron required for the synthesis of hemoglobin in the fetal liver, and it is a hematopoietic growth factor, regulating both the differentiation and proliferation of hematopoietic stem cells and their colonization in the yolk sac, liver, spleen, and bone marrow (Bazer et al. 1991; Ying et al. 2014).

2.6 Summary and Conclusions

In this review, we have summarized some of the critical molecular signaling and morphological events that are crucial for the establishment of a successful pregnancy. Whilst many of these processes are conserved, there are key differences across species. It is important to consider these species-specific differences when designing an experiment to investigate the mechanisms controlling implantation and placentation, placental transport of minerals and nutrients, and when extrapolating the findings from studies of one species to another species. While each animal model has its own merits, it is important to note that no animal model truly recapitulates human pregnancy. Comparative studies of the mechanisms governing implantation and placentation across species are critical for the discovery of improved strategies to enhance reproductive health and fertility in both humans and livestock species.

Conflicts of Interest The authors have no conflicts of interest to declare.

References

- Amoroso E (1952) Placentation. In: Parkes A (ed) Marshall's physiology of reproduction. Little Brown & Co, Boston, MA, USA, pp 127–311
- Aplin JD, Ruane PT (2017) Embryo—epithelium interactions during implantation at a glance. *J Cell Sci* 130:15–22
- Bazer F (1989) Establishment of pregnancy in sheep and pigs. *Reprod Fertil Dev* 1:237–242
- Bazer FW (2013) Pregnancy recognition signaling mechanisms in ruminants and pigs. *J Anim Sci Biotechnol* 4:1–10
- Bazer FW, Johnson GA (2014) Pig blastocyst-uterine interactions. *Differentiation* 87:52–65
- Bazer FW, Marengo SR, Geisert RD, Thatcher WW (1984) Exocrine versus endocrine secretion of prostaglandin f2a in the control of pregnancy in swine. *Anim Reprod Sci* 7:115–132
- Bazer FW, Worthington-White D, Fliss MFV, Gross S (1991) Uteroferrin: a progesterone-induced hematopoietic growth factor of uterine origin. *Exp Hematol* 19:910–915
- Bazer FW, Ott TL, Spencer TE (1994) Pregnancy recognition in ruminants, pigs and horses: signals from the trophoblast. *Theriogenology* 41:79–94
- Bazer FW, Burghardt RC, Johnson GA, Spencer TE, Wu G (2008) Interferons and progesterone for establishment and maintenance of pregnancy: interactions among novel cell signaling pathways. *Reprod Biol* 8:179–211
- Bazer FW, Spencer TE, Johnson GA (2009) Interferons and uterine receptivity. *Semin Reprod Med* 27:90–102
- Bazer FW, Wu G, Johnson GA, Kim J, Song G (2011) Uterine histotroph and conceptus development: Select nutrients and secreted phosphoprotein 1 affect mechanistic target of rapamycin cell signaling in ewes. *Biol Reprod* 85:1094–1107
- Bazer FW, Spencer TE, Thatcher WW (2012) Growth and development of the ovine conceptus. *J Anim Sci* 90:159–170
- Bazer FW, Wang X, Johnson GA, Wu G (2015a) Select nutrients and their effects on conceptus development in mammals. *Anim Nutr* 1:85–95
- Bazer FW, Ying W, Wang X, Dunlap KA, Zhou B, Johnson GA (2015b) The many faces of interferon tau. *Amino Acids* 47:449–460
- Bazer FW, Burghardt RC, Johnson GA, Spencer TE, Wu G (2018) Mechanisms for the establishment and maintenance of pregnancy: Synergies from scientific collaborations. *Biol Reprod* 99:225–241
- Beall MH, Wang S, Yang B, Chaudhri N, Amidi F, Ross MG (2007) Placental and membrane aquaporin water channels: correlation with amniotic fluid volume and composition. *Placenta* 28:421–428
- Bonduelle ML, Dodd R, Liebaers I, Van Steirteghem A, Williamson R, Akhurst R (1988) Chorionic

- gonadotrophin- β mRNA, a trophoblast marker, is expressed in human 8-cell embryos derived from tripronucleate zygotes. *Hum Reprod* 3:909–914
- Carson DD, Bagchi I, Dey SK, Enders AC, Fazleabas AT, Lessey BA, Yoshinaga K (2000) Embryo implantation. *Dev Biol* 223:217–237
- Chan HC, Ruan YC, He Q, Chen MH, Chen H, Xu WM, Chen WY, Xie C, Zhang XH, Zhou Z (2009) The cystic fibrosis transmembrane conductance regulator in reproductive health and disease. *J Physiol* 587:2187–2195
- Chen C, Spencer TE, Bazer FW (2000) Fibroblast growth factor-10: a stromal mediator of epithelial function in the ovine uterus. *Biol Reprod* 63:959–966
- Chen C, Spencer TE, Bazer FW (2000) Expression of hepatocyte growth factor and its receptor c-met in the ovine uterus. *Biol Reprod* 62:1844–1850
- Choi Y, Johnson GA, Burghardt RC, Berghman LR, Joyce MM, Taylor KM, Stewart MD, Bazer FW, Spencer TE (2001) Interferon regulatory factor-two restricts expression of interferon-stimulated genes to the endometrial Stroma and glandular epithelium of the ovine uterus. *Biol Reprod* 65:1038–1049
- Cockburn K, Rossant J (2010) Making the blastocyst: lessons from the mouse. *J Clin Invest* 120:995–1003
- Dantzer V, Leiser R (1994) Initial vascularisation in the pig placenta: I. Demonstration of nonglandular areas by histology and corrosion cases. *Anat Rec* 238:177–190
- De Oliveira V, Schaefer J, Abu-Rafea B, Vilos GA, Vilos AG, Bhattacharya M, Radovick S, Babwah AV (2020) Uterine aquaporin expression is dynamically regulated by estradiol and progesterone and ovarian stimulation disrupts embryo implantation without affecting luminal closure. *Mol Hum Reprod* 26:154–166
- Fazleabas AT, Kim JJ, Strakova Z (2004) Implantation: embryonic signals and the modulation of the uterine environment—a review. *Placenta* 25:S26–S31
- Fleming JGW, Spencer TE, Safe SH, Bazer FW (2006) Estrogen regulates transcription of the ovine oxytocin receptor gene through GC-rich SPI promoter elements. *Endocrinology* 147:899–911
- Freeman ME, Smith MS, Nazian SJ, Neill JD (1974) Ovarian and hypothalamic control of the daily surges of prolactin secretion during Pseudopregnancy in the rat. *Endocrinology* 94:875–882
- Friess AE, Sinowatz F, Skolek-Winnisch R, Träutner W (1981) The placenta of the pig II the ultrasound of the areolae. *Anat Embryol (berl)* 163:43–53
- Friess AE, Sinowatz F, Skolek-Winnisch R, Trautner W (1980) The placenta of the Pig I. Finestructural changes of the placental barrier during pregnancy. *Anat Embryol (berl)* 158:179–191
- Furukawa S, Tsuji N, Sugiyama A (2019) Morphology and physiology of rat placenta for toxicological evaluation. *J Toxicol Pathol* 32:1–17
- Gunnet JW, Freeman ME (1983) The Mating-induced release of prolactin: a unique neuroendocrine response. *Endocr Rev* 4:44–61
- Igarashi M, Finch PW, Aaronson SA (1998) Characterization of recombinant human fibroblast growth factor (FGF)-10 reveals functional similarities with keratinocyte growth factor (FGF-7). *J Biol Chem* 273:13230–13235
- Johnson GA, Spencer TE, Burghardt RC, Taylor KM, Gray CA, Bazer FW (2000) Progesterone modulation of osteopontin gene expression in the ovine uterus. *Biol Reprod* 62:1315–1321
- Johnson GA, Bazer FW, Burghardt RC, Spencer TE, Wu G, Bayless KJ (2009) Conceptus-uterus interactions in pigs: endometrial gene expression in response to estrogens and interferons from conceptuses. *Soc Reprod Fertil Suppl* 66:321–332
- Johnson GA, Burghardt RC, Bazer FW (2014) Osteopontin: a leading candidate adhesion molecule for implantation in pigs and sheep. *J Anim Sci Biotechnol* 5:1–14
- Johnson GA, Bazer FW, Burghardt RC, Wu G, Seo H, Kramer AC, McLendon BA (2018) Cellular events during ovine implantation and impact for gestation. *Anim Reprod* 15:843–855
- Joyce MM, Burghardt JR, Burghardt RC, Hooper RN, Jaeger LA, Spencer TE, Bazer FW, Johnson GA (2007) Pig conceptuses increase uterine interferon-regulatory factor 1 (IRF1), but restrict expression to stroma through estrogen-induced IRF2 in luminal epithelium. *Biol Reprod* 77:292–302
- Kim S, Kim J (2017) A review of mechanisms of implantation. *Dev Reprod* 21:351–359
- Knight JW, Bazer FW, Thatcher WW, Franke DE, Wallace D (1977) Conceptus development in intact and unilaterally Hysterectomized-Ovariectomized gilts: interrelations among hormonal status, placental development, fetal fluids and fetal growth. *J Anim Sci* 44:620–637
- Kramer AC, Steinhauser CB, Gao H, Seo H, McLendon BA, Burghardt RC, Wu G, Bazer FW, Johnson GA (2020) Steroids regulate SLC2A1 and SLC2A3 to deliver glucose into Trophoctoderm for metabolism via glycolysis. *Endocrinology* 161:1–19
- Marrable AW (1971) The embryonic pig: a chronological account. Pitman Medical, London
- Matsumoto H (2017) Molecular and cellular events during blastocyst implantation in the receptive uterus: clues from mouse models. *J Reprod Dev* 63:445–454
- McGowen MR, Erez O, Romero R, Wildman DE (2014) The evolution of embryo implantation. *Int J Dev Biol* 58:155–161
- Meyer AE, Pfeiffer CA, Brooks KE, Spate LD, Benne JA, Cecil R, Samuel MS, Murphy CN, Behura S, Mclean MK, Ciernia LA, Smith MF, Whitworth KM, Wells KD, Spencer TE, Prather RS, Geisert RD (2019) New perspective on conceptus estrogens in maternal recognition and pregnancy establishment in the pig. *Biol Reprod* 101:148–161
- Picut CA, Swanson CL, Parker RF, Scully KL, Parker GA (2009) The metrial gland in the rat and its similarities to granular cell tumors. *Toxicol Pathol* 37:474–480

- Richard C, Gao J, Brown N, Reese J (2003) Aquaporin water channel genes are differentially expressed and regulated by ovarian steroids during the periimplantation period in the mouse. *Endocrinology* 144:1533–1541
- Seo H, Bazer FW, Burghardt RC, Johnson GA (2019) Immunohistochemical examination of trophoblast syncytialization during early placentation in sheep. *Int J Mol Sci* 20:1–13
- Seo H, Frank JW, Burghardt RC, Bazer FW, Johnson GA (2020a) Integrins and OPN localize to adhesion complexes during placentation in sheep. *Reproduction* 160:521–532
- Seo H, Li X, Wu G, Bazer FW, Burghardt RC, Bayless KJ, Johnson GA (2020b) Mechanotransduction drives morphogenesis to develop folding during placental development in pigs. *Placenta* 90:62–70
- Soares MJ (2004) The prolactin and growth hormone families: pregnancy-specific hormones/cytokines at the maternal-fetal interface. *Reprod Biol Endocrinol* 2:1–15
- Soares MJ, Alam SMK, Konno T, Ho-chen JK, Ain R (2006) The prolactin family and pregnancy-dependent adaptations. *Anim Sci J* 77:1–9
- Soares MJ, Konno T, Alam SMK (2007) The prolactin family: effectors of pregnancy-dependent adaptations. *Trends Endocrinol Metab* 18:114–121
- Soares MJ, Varberg KM, Iqbal K (2018) Hemochorial placentation: development, function, and adaptations. *Biol Reprod* 99:196–211
- Spencer TE, Bazer FW (2004) Conceptus signals for establishing and maintenance of pregnancy. *Reprod Biol Endocrinol* 2:1–15
- Spencer TE, Johnson GA, Bazer FW, Burghardt RC (2004) Focus on Implantation Implantation mechanisms: insights from the sheep. *Reproduction* 128:657–668
- Srisuparp S, Strakova Z, Fazleabas AT (2001) The role of chorionic gonadotropin (CG) in blastocyst implantation. *Arch Med Res* 32:627–634
- Stouffer RL (1988) Perspectives on the corpus luteum of the menstrual cycle and early pregnancy. *Semin Reprod Endocrinol* 6:103–113
- Stouffer RL, Bishop CV, Bogan RL, Xu F, Hennebold JD (2014) Endocrine and local control of the primate corpus Luteum. *Reprod Biol* 13:259–271
- Stouffer RL, Hearn JP (1998) Endocrinology of the transition from menstrual cyclicity to establishment of pregnancy in primates. In: Bazer FW (ed) *Endocrinology of Pregnancy*. Humana Press
- Strickland S, Reich E, Sherman MI (1976) Plasminogen activator in early embryogenesis: enzyme production by trophoblast and parietal endoderm. *Cell* 9:231–240
- Su R-W, Fazleabas AT (2015) Implantation and establishment of pregnancy in human and nonhuman primates. *Adv Anatomy, Embryol Cell Biol* 216:189–213
- Syrkasheva AG, Dolgushina NV, Romanov AY, Burmenskaya OV, Makarova NP, Ibragimova EO, Kalinina EA, Sukhikh GT (2017) Cell and genetic predictors of human blastocyst hatching success in assisted reproduction. *Zygote* 25:631–636
- Thatcher W, Meyer MD, Danet-Desnoyers G (1995) Maternal recognition of pregnancy. *J Reprod Fertil Suppl* 49:15–28
- Turco MY, Moffett A (2019) Development of the Human Placenta. *Development* 146:1–14
- Vallet JL, Freking BA (2007) Differences in placental structure during gestation associated with large and small pig fetuses. *J Anim Sci* 85:3267–3275
- Wassarman PM (1988) Zona Pellucida Glycoproteins. *Annu Rev Biochem* 57:415–442
- Wassarman PM, Litscher ES (2008) Mammalian fertilization: the egg's multifunctional zona pellucida. *Int J Dev Biol* 52:665–676
- Wu G (2022) Nutrition and metabolism: Foundations for animal growth, development, reproduction, and health. *Adv Exp Med Biol* 1354:1–24
- Ying W, Wang H, Bazer FW, Zhou B (2014) Pregnancy-secreted acid phosphatase, uteroferrin, enhances fetal erythropoiesis. *Endocrinology* 155:4521–4530

Single-cell reconstruction of the early maternal–fetal interface in humans

Roser Vento-Tormo^{1,2,13}, Mirjana Efreмова^{1,13}, Rachel A. Botting³, Margherita Y. Turco^{2,4,5}, Miquel Vento-Tormo⁶, Kerstin B. Meyer¹, Jong-Eun Park¹, Emily Stephenson³, Krzysztof Polański¹, Angela Goncalves^{1,7}, Lucy Gardner^{2,4}, Staffan Holmqvist⁸, Johan Henriksson¹, Angela Zou¹, Andrew M. Sharkey^{2,4}, Ben Millar³, Barbara Innes³, Laura Wood¹, Anna Wilbrey-Clark¹, Rebecca P. Payne³, Martin A. Ivarsson⁴, Steve Lisgo⁹, Andrew Filby³, David H. Rowitch⁸, Judith N. Bulmer³, Gavin J. Wright¹, Michael J. T. Stubbington¹, Muzlifah Haniffa^{1,3,10,14*}, Ashley Moffett^{2,4,14*} & Sarah A. Teichmann^{1,11,12,14*}

During early human pregnancy the uterine mucosa transforms into the decidua, into which the fetal placenta implants and where placental trophoblast cells intermingle and communicate with maternal cells. Trophoblast–decidual interactions underlie common diseases of pregnancy, including pre-eclampsia and stillbirth. Here we profile the transcriptomes of about 70,000 single cells from first-trimester placentas with matched maternal blood and decidual cells. The cellular composition of human decidua reveals subsets of perivascular and stromal cells that are located in distinct decidual layers. There are three major subsets of decidual natural killer cells that have distinctive immunomodulatory and chemokine profiles. We develop a repository of ligand–receptor complexes and a statistical tool to predict the cell–type specificity of cell–cell communication via these molecular interactions. Our data identify many regulatory interactions that prevent harmful innate or adaptive immune responses in this environment. Our single-cell atlas of the maternal–fetal interface reveals the cellular organization of the decidua and placenta, and the interactions that are critical for placentation and reproductive success.

During early pregnancy, the uterine mucosal lining—the endometrium—is transformed into the decidua under the influence of progesterone. Decidualization results from a complex and well-orchestrated differentiation program that involves all cellular elements of the mucosa: stromal, glandular and immune cells, the last of which include the distinctive decidual natural killer (dNK) cells^{1,2}. The blastocyst implants into the decidua, and initially—before arterial connections are established—uterine glands are the source of histotrophic nutrition in the placenta^{3,4}. After implantation, placental extravillous trophoblast cells (EVT) invade through the decidua and move towards the spiral arteries, where they destroy the smooth muscle media and transform the arteries into high conductance vessels⁵. Balanced regulation of EVT invasion is critical to pregnancy success: to ensure correct allocation of resources to mother and baby, arteries must be sufficiently transformed but excessive invasion must be prevented⁶. The pivotal regulatory role of the decidua is obvious from the life-threatening, uncontrolled trophoblast invasion that occurs when the decidua is absent, as when the placenta implants on a previous Caesarean section scar⁷.

EVT have a unique human leukocyte antigen (HLA) profile: they do not express the dominant T cell ligands, class I HLA-A and HLA-B, or class II molecules^{8,9} but do express HLA-G and HLA-E and polymorphic HLA-C class I molecules. These trophoblast HLA ligands have receptors that are expressed by the dominant decidual immune cells (that is, dNKs), including maternal killer immunoglobulin-like receptors (KIRs) some of which bind to HLA-C molecules^{10,11}. Certain combinations of maternal KIRs and fetal HLA-C genetic variants are

associated with pregnancy disorders such as pre-eclampsia, in which trophoblast invasion is deficient¹². However, detailed understanding of the cellular interactions in the decidua that support early pregnancy is lacking.

In this study, we used single-cell transcriptomics to comprehensively resolve the cell states that are involved in maternal–fetal communication in the decidua, during early pregnancy when the placenta is established. We then used a computational framework to predict cell-type-specific ligand–receptor complexes and present a new database of the curated complexes (www.CellPhoneDB.org/). By integrating these predictions with spatial *in situ* analysis, we construct a detailed molecular and cellular map of the human decidual–placental interface.

Maternal and fetal cells in early pregnancy

We combined droplet-based encapsulation (using the 10x Genomics Chromium system)¹³ and plate-based Smart-seq2¹⁴ single-cell transcriptome profiles from the maternal–fetal interface (11 deciduas and 5 placentas from 6–14 gestational weeks) and six matched peripheral blood mononuclear cells (Fig. 1a, b, Supplementary Tables 1, 2, Extended Data Fig. 1). After computational quality control and integration of transcriptomes from both technologies, we performed graph-based clustering (see Methods) of the combined dataset and used cluster-specific marker genes to annotate the clusters (Fig. 1c, Extended Data Figs. 2, 3a–d, Supplementary Table 2). We studied T cell composition and clonal expansion using full-length transcriptomes from

¹Wellcome Sanger Institute, Cambridge, UK. ²Centre for Trophoblast Research, University of Cambridge, Cambridge, UK. ³Institute of Cellular Medicine, Newcastle University, Newcastle upon Tyne, UK. ⁴Department of Pathology, University of Cambridge, Cambridge, UK. ⁵Department of Physiology, Development and Neuroscience, University of Cambridge, Cambridge, UK. ⁶YDEVs software development, Valencia, Spain. ⁷German Cancer Research Center (DKFZ), Heidelberg, Germany. ⁸Department of Paediatrics, Wellcome - MRC Cambridge Stem Cell Institute, University of Cambridge, Cambridge, UK. ⁹Human Developmental Biology Resource, Institute of Genetic Medicine, Newcastle University, Newcastle upon Tyne, UK. ¹⁰Department of Dermatology and NIHR Newcastle Biomedical Research Centre, Newcastle Hospitals NHS Foundation Trust, Newcastle upon Tyne, UK. ¹¹Theory of Condensed Matter Group, The Cavendish Laboratory, University of Cambridge, Cambridge, UK. ¹²European Molecular Biology Laboratory, European Bioinformatics Institute (EMBL-EBI), Cambridge, UK. ¹³These authors contributed equally: Roser Vento-Tormo, Mirjana Efreмова. ¹⁴These authors jointly supervised this work: Muzlifah Haniffa, Ashley Moffett, Sarah A. Teichmann. *e-mail: m.a.haniffa@newcastle.ac.uk; am485@cam.ac.uk; st9@sanger.ac.uk

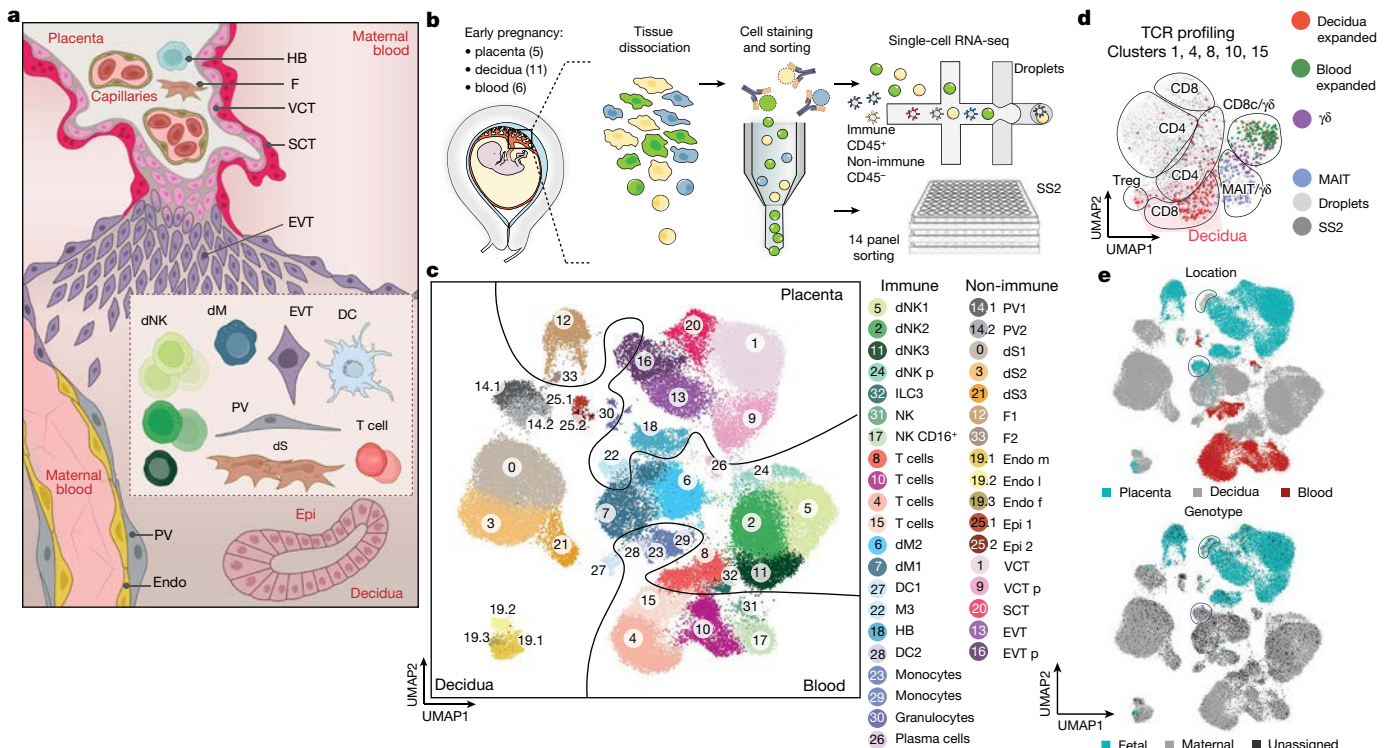


Fig. 1 | Identification of cell types at the maternal–fetal interface.

a, Diagram illustrating the decidual–placental interface in early pregnancy. DC, dendritic cells; dM, decidual macrophages; dS, decidual stromal cells; Endo, endothelial cells; Epi, epithelial glandular cells; F, fibroblasts; HB, Hofbauer cells; PV, perivascular cells; SCT, syncytiotrophoblast; VCT, villous cytotrophoblast; EVT, extravillous trophoblast. **b**, Workflow for single-cell transcriptome profiling of decidua, placenta and maternal peripheral blood mononuclear cells. Numbers in parentheses indicate number of individuals analysed. **c**, Placental and decidual cell clusters

Smart-seq2 and reconstructed the T cell receptor sequences from this data, which showed expansion of CD8 T cells in the decidua (Fig. 1d).

We aligned single-cell RNA-sequencing (scRNA-seq) reads from each cell with overlapping single nucleotide polymorphisms called from maternal and fetal genomic DNA to assign cells as fetal or maternal (Fig. 1e, Extended Data Fig. 3e). As expected, decidual samples contained mostly maternal cells with a few fetal *HLA-G*⁺ EVT. Fetal cells dominate the placental samples, with the exception of maternal macrophages (M3 cluster) that express *CD14*, *S100A9*, *CD163*, *CD68* and *CSF1R* (Extended Data Fig. 3f). These are probably derived from blood monocytes incorporated into the syncytium¹⁵.

Cell communication predicted by CellPhoneDB

To systematically study the interactions between fetal and maternal cells in the decidual–placental interface, we developed a repository (www.CellPhoneDB.org) of ligand–receptor interacting pairs that accounts for their subunit architecture, representing heteromeric complexes accurately (Extended Data Fig. 4a). Both secreted and cell-surface molecules are considered; the repository therefore encompasses ligand–receptor interactions mediated by the diffusion of secreted molecules. Our repository forms the basis of a computational approach to identify biologically relevant ligand–receptor complexes. We consider the expression levels of ligands and receptors within each cell type, and use empirical shuffling to calculate which ligand–receptor pairs display significant cell-type specificity (Extended Data Fig. 4b, see Methods). This predicts molecular interactions between cell populations via specific protein complexes, and generates a potential cell–cell communication network in the decidua and placenta (Extended Data Fig. 4c–e, Supplementary Tables 3, 4).

from 10x Genomics and Smart-seq2 (SS2) scRNA-seq analysis visualized by UMAP. Colours indicate cell type or state. $n = 11$ deciduas, $n = 5$ placentas and $n = 6$ blood samples. **f**, fetal; ILC, innate lymphocyte cells; l, lymphatic; m, maternal; p, proliferative; M3, maternal macrophages. **d**, UMAP visualization of T cell clonal expansion and clusters by integrating Smart-seq2 and 10x Genomics T cell data from clusters 4, 8, 10 and 15 from **c**. TCR, T cell receptor. MAIT, mucosal-associated invariant T cell. **e**, Origin of droplet cells in **c** by tissue (above) or genotype (below). Purple circle, maternal cells in placenta; green circle, fetal cells in decidua.

Trophoblast differentiation by scRNA-seq

To investigate maternal–fetal interactions at the decidual–placental interface, we first analysed fetal trophoblast cells isolated from placental and decidual samples: the latter contain invasive EVT (Extended Data Fig. 5a, b). Consistent with previous results^{16,17}, we resolved two distinct trophoblast differentiation pathways (Fig. 2a). As expected, decidual EVT are at the end of the trajectory, have high levels of expression of *HLA-G* and no longer express cell-cycle genes (Extended Data Fig. 5c). For villous cytotrophoblast cells, CellPhoneDB predicts interactions of receptors involved in cellular proliferation and differentiation (*EGFR*, *NRP2* and *MET*) with their corresponding ligands expressed by other cells in the placenta. *HBEGF*, potentially interacting with *EGFR*, is expressed by Hofbauer cells, and *PGF* and *HGF*—the respective ligands of *NRP2* and *MET*—are expressed by different placental fibroblast subsets (Fig. 2b, Supplementary Table 5).

By contrast, during EVT differentiation there is upregulation of receptors involved in immunomodulation, cellular adhesion and invasion, the ligands of which are expressed by decidual cells (Fig. 2b). For example, *ACKR2* is a decoy receptor for inflammatory cytokines that are produced by maternal immune cells¹⁸ and *CXCR6* is a chemokine receptor that binds to *CXCL16* expressed by the maternal macrophages. Expression of *TGFB1*—the function of which is to suppress immune responses¹⁹ and activate epithelial–mesenchymal transitions—and its receptor increases as EVT differentiate. Components involved in the epithelial–mesenchymal-transition program are upregulated at the end of the trajectory²⁰ (Extended Data Fig. 5d); these include *PAPPA* and *PAPPA2*, which encode metalloproteinases that are known to be involved in cellular invasion. In pregnancy, a decreased level of *PAPPA* is a biomarker for pre-eclampsia and fetal growth restriction, which are associated with defective EVT invasion²¹.

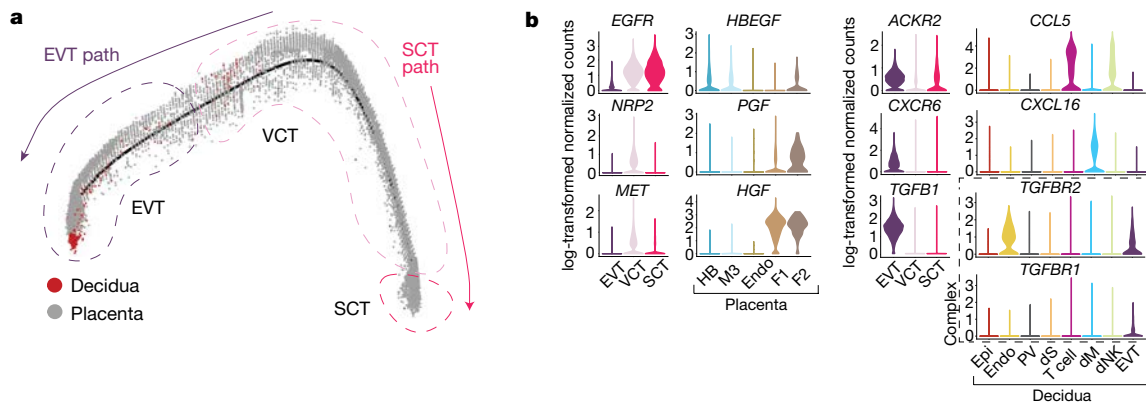


Fig. 2 | Ligand-receptor expression during EVT differentiation. **a**, Pseudotime ordering of trophoblast cells reveals EVT and SCT pathways. Enriched EPCAM⁺ and HLA-G⁺ cells on placental and decidua isolates are included. $n = 11$ deciduas and $n = 5$ placentas. **b**, Violin plots showing log-transformed, normalized expression levels for selected

ligand-receptor pairs that change during pseudotime and are predicted to be significant by CellPhoneDB (*EGFR*, *HBEFG*, *NRP2*, *PGF*, *MET*, *HGF*, *ACKR2*, *CCL5*, *CXCR6*, *CXCL16*, *TGFB1*, *TGFB2* and *TGFB1*). Cells from Fig. 1c are used for the violin plots.

Stromal cells in the two decidual layers

EVT initially invade through the surface epithelium into the decidua compacta. Beneath this is the decidua spongiosa that contains hypersecretory glands, which provide histotrophic nutrition to the early conceptus. Markers that distinguish the different decidual fibroblast populations identify two clusters of perivascular cells (referred to as PV1 and PV2) that share expression of the smooth muscle marker (*MGP*) and are distinguished by different levels of *MCAM*, which is higher in PV1, and *MMP11*, which is higher in PV2 (Fig. 3a, Supplementary Table 6). There are three clusters of stromal cells (labelled dS1, dS2 and dS3), all of which express the WNT inhibitor *DKK1*. dS1 shares the expression of *ACTA2* and *TAGLN* with PV1 and

PV2, and lacks expression of the classical decidual markers prolactin (*PRL*) and *IGFBP1*. By contrast, dS2 and dS3 express *IGFBP1*, *IGFBP2* and *IGFBP6* and share markers with two subsets of decidualized stromal cells that have recently been described in vitro²². The dS3 subset expresses *PRL* as well as genes involved in steroid biosynthesis (for example, *CYP11A1*) (Extended Data Fig. 6a).

To locate the different perivascular and stromal populations in situ, we used immunohistochemistry as well as multiplexed single-molecule fluorescent in situ hybridization (smFISH) for selected markers on serial sections of decidua parietalis. These experiments confirm that cells that express *ACTA2* and *MCAM* are present in the smooth muscle media of the spiral arteries²³ and show that *MMP11* is also

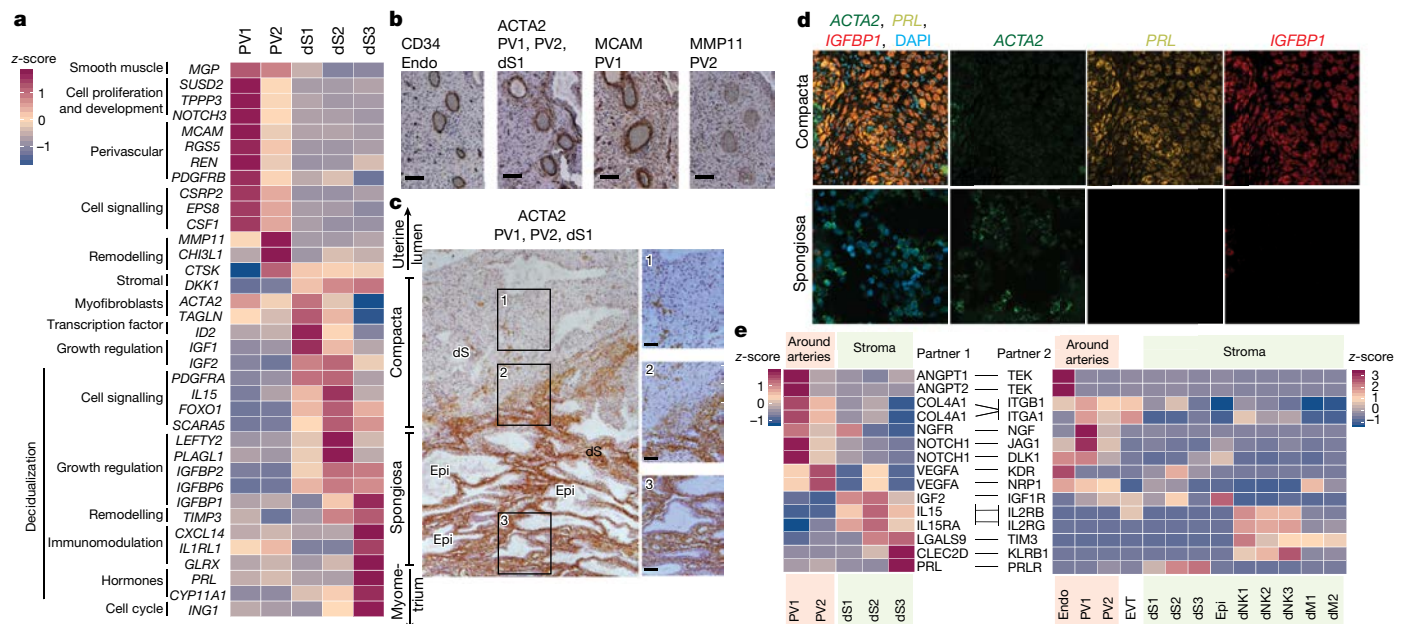


Fig. 3 | Stromal distribution in the two distinct decidual layers. **a**, Heat map showing relative expression (z-score) of selected genes for perivascular and decidual stromal cells ($n = 11$ deciduas; adjusted P value < 0.1; Wilcoxon rank-sum test with Bonferroni correction). **b**, Immunohistochemistry of a spiral artery in serial sections of the decidua, stained for CD34 (endothelial cells), *ACTA2* (PV cells and dS1 cells), *MCAM* (PV1 cells) and *MMP11* (PV2 cells) ($n = 2$ biological replicates). Scale bar, 100 μ m. **c**, Immunohistochemistry of decidua sections stained for *ACTA2*, which distinguishes between *ACTA2*⁺ dS1 in decidua spongiosa and *ACTA2*⁻ dS2 and dS3 in decidua compacta ($n = 3$

biological replicates). Right panels are a higher magnification of the respectively numbered inset. Scale bar, 50 μ m. **d**, Multiplexed smFISH of decidua parietalis showing two decidual layers. *ACTA2*⁺ dS1 in decidua spongiosa (40 \times objective); *IGFBP1*⁺ and *PRL*⁺ dS2 and dS3 confined to decidua compacta (20 \times objective) ($n = 2$ biological replicates). **e**, Heat map shows selected significant ligand-receptor interactions ($n = 6$ deciduas, P value < 0.05, permutation test, see Methods) between PV cells and dS cells (left) and decidual cells (right) ($n = 11$ deciduas). Assays were carried out at the mRNA level, but are extrapolated to protein interactions.

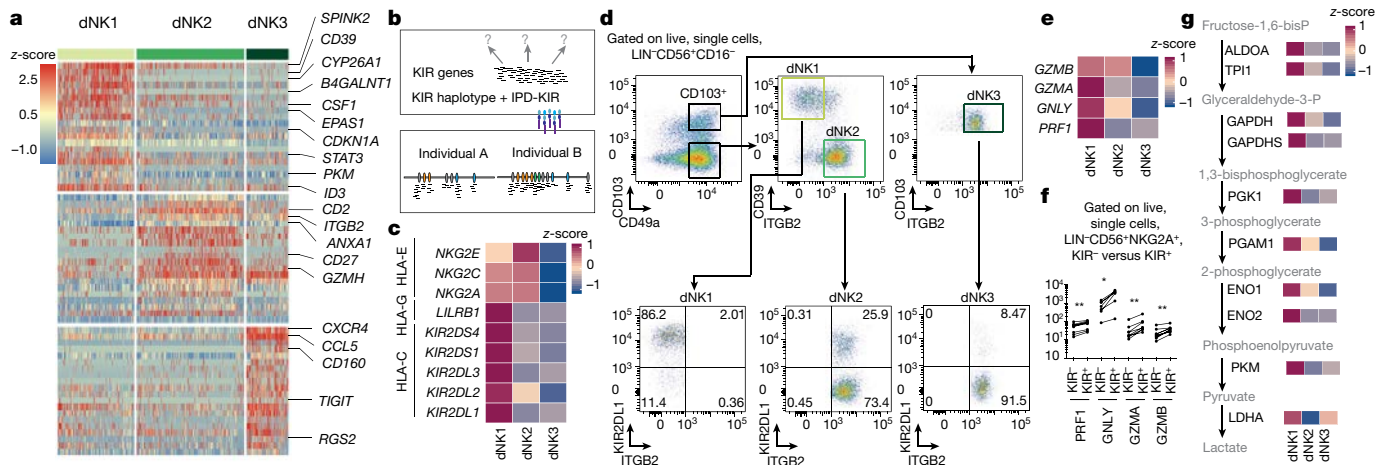


Fig. 4 | Three dNK populations. **a**, Heat map showing relative expression (z-score) of markers defining the three dNK subsets ($n = 11$ deciduas; percentage 1 > 10%, percentage 2 < 60%; refers to the percentage of cells with expression above 0 in the corresponding cluster and all other clusters; P value < 0.1 after Bonferroni correction, Wilcoxon rank-sum test). **b**, Workflow for KIRid method (see <https://github.com/Teichlab/KIRid>). IPD-KIR, database for human KIR (available at <https://www.ebi.ac.uk/ipd/kir/>). **c**, z-scores of KIR receptors (mean expression levels). Expression values were generated using Smart-seq2 data and the KIRid approach ($n = 5$ deciduas). **d**, FACS gating strategy to identify dNK subsets

present, which demonstrates that both PV1 and PV2 are perivascular (Fig. 3b). *ACTA2*⁺ dS1 cells are present between glands in the decidua spongiosa, whereas *IGFBP1*⁺ and *PRL*⁺ dS2 and dS3 cells are located in decidua compacta (Fig. 3c, d, Extended Data Fig. 7). *CYP11A1* is also expressed more abundantly in decidua compacta than in decidua spongiosa (Extended Data Fig. 6b).

Our CellPhoneDB tool predicts that the cognate receptors for angiogenic factors that are expressed by PV1 and PV2 (for example, *ANGPT1* and *VEGFA*) are located in the endothelium (Fig. 3e). EVT first invade the decidua compacta, where dS2 and dS3 express high levels of *LGALS9* and *CLEC2D*. These molecules could interact with their respective inhibitory receptors *TIM3* (also known as *HAVCR2*) and *KLRB1*—which are expressed by subsets of dNKs—enabling the stroma to suppress inflammatory reactions in the decidua.

Three decidual NK cell states

We identified three main dNK subsets (dNK1, dNK2 and dNK3), which all co-express the tissue-resident markers *CD49A* (also known as *ITGA1*) and *CD9* (Extended Data Fig. 8a). dNK1 cells express *CD39* (also known as *ENTPD1*), *CYP26A1* and *B4GALNT1*, whereas the defining markers of dNK2 cells are *ANXA1* and *ITGB2*; the latter is shared with dNK3 cells (Fig. 4a, Supplementary Table 7). dNK3 cells express *CD160*, *KLRB1* and *CD103* (also known as *ITGAE*), but not the innate lymphocyte cell marker *CD127* (also known as *IL7R*) (Extended Data Fig. 8a).

Genes of the KIR family are polymorphic and highly homologous, which makes the quantification of mRNA expression of individual KIR genes challenging¹². We therefore developed ‘KIRid’, a method that uses full-length transcript Smart-seq2 data to map the single-cell reads of each donor to the corresponding donor-specific reference of KIR alleles (Fig. 4b, see Methods). We find that dNK1 cells express higher levels of KIRs that can bind to HLA-C molecules: inhibitory *KIR2DL1*, *KIR2DL2* and *KIR2DL3* and activating *KIR2DS1* and *KIR2DS4* (Fig. 4c, Supplementary Table 8). *LILRB1*, the receptor with high affinity for the dimeric form of HLA-G molecules, is expressed only by the dNK1 subset. Both dNK1 and dNK2—but not dNK3—express activating *NKG2C* (also known as *KLRC2*) and *NKG2E* (also known as *KLRC3*) as well as inhibitory *NKG2A* (also known as *KLRC1*) receptors for HLA-E molecules (Fig. 4c). These

(representative sample from $n = 6$ individuals; Supplementary Table 9). **e**, z-scores of expression of granule molecules *PRF1*, *GNLY*, *GZMA* and *GZMB* in dNK subsets ($n = 11$ individuals). **f**, Flow cytometry to compare staining of granule components in *NKG2A*⁺*KIR*⁺ versus *NKG2A*⁺*KIR*⁻ dNK cells (*PRF1* $n = 9$ individuals; *GNLY* $n = 7$ individuals; *GZMA* $n = 8$ individuals; *GZMB* $n = 10$ individuals; Supplementary Table 9). Non-parametric paired Wilcoxon test. * $P < 0.05$, ** $P < 0.01$. **g**, Right, z-scores of glycolysis enzymes (mean mRNA expression). Left, only differentially expressed enzymes are shown in the glycolysis pathway ($n = 11$ deciduas; P value < 0.1 after Bonferroni correction, Wilcoxon rank-sum test).

results predict a likely function of dNK1 in the recognition and response to EVT.

To investigate these three dNK populations further, we analysed six decidual samples by flow cytometry using *CD49A* (expressed by resident dNKs), combined with markers for each dNK subset predicted from our transcriptomics data (*CD39*, *ITGB2*, *CD103* and *KIR2DL1*) (Fig. 4d, Extended Data Fig. 8b). We confirmed the presence of the three dNK populations by flow cytometry and the preferential expression of *KIR2DL1* in dNK1 (Fig. 4d, Supplementary Table 9). We analysed the morphology of dNK subsets by Giemsa staining of cells isolated by flow cytometric sorting (Extended Data Fig. 8c). dNK1 contains more cytoplasmic granules than dNK2 and dNK3, which is consistent with our scRNA-seq data that show higher levels of expression of *PRF1*, *GNLY*, *GZMA* and *GZMB* RNA in this subset (Fig. 4e). Higher levels of expression of the granule proteins (*PRF1*, *GNLY*, *GZMA* and *GZMB*) are found in *KIR*⁺ compared to *KIR*⁻ dNK cells by flow cytometry (Fig. 4f). dNK1 cells also express high levels of enzymes involved in glycolysis (Fig. 4g). Thus, dNK1 cells are characterized by active glycolytic metabolism, and show higher expression of KIR genes (*KIR2DS1*, *KIR2DS4*, *KIR2DL1*, *KIR2DL2* and *KIR2DL3*), *LILRB1* and cytoplasmic granule proteins, suggesting that it is dNK1 cells that particularly interact with EVT.

First pregnancies are associated with lower proportions of dNK cells that express *LILRB1*²⁴, lower birth weights and increased occurrence of disorders such as pre-eclampsia²⁵. Metabolomic programming of mature ‘memory’ natural killer cells also occurs in chronic human cytomegalovirus infection²⁶. Together, these findings are consistent with the ‘priming’ of dNK1 cells during a first pregnancy so they can respond more effectively to the implanting placenta in subsequent pregnancies.

Immunomodulation during early pregnancy

We next used CellPhoneDB to identify the expression of cytokines and chemokines by dNKs, and to predict their interactions with other cells at the maternal–fetal interface (Fig. 5a, Extended Data Fig. 9a). However, contrary to previous studies^{24,27}, we find no evidence for substantial *VEGFA* or *IFNG* expression by dNKs in vivo—probably because these studies used dNK cells cultured with IL-2 or IL-15 in vitro.

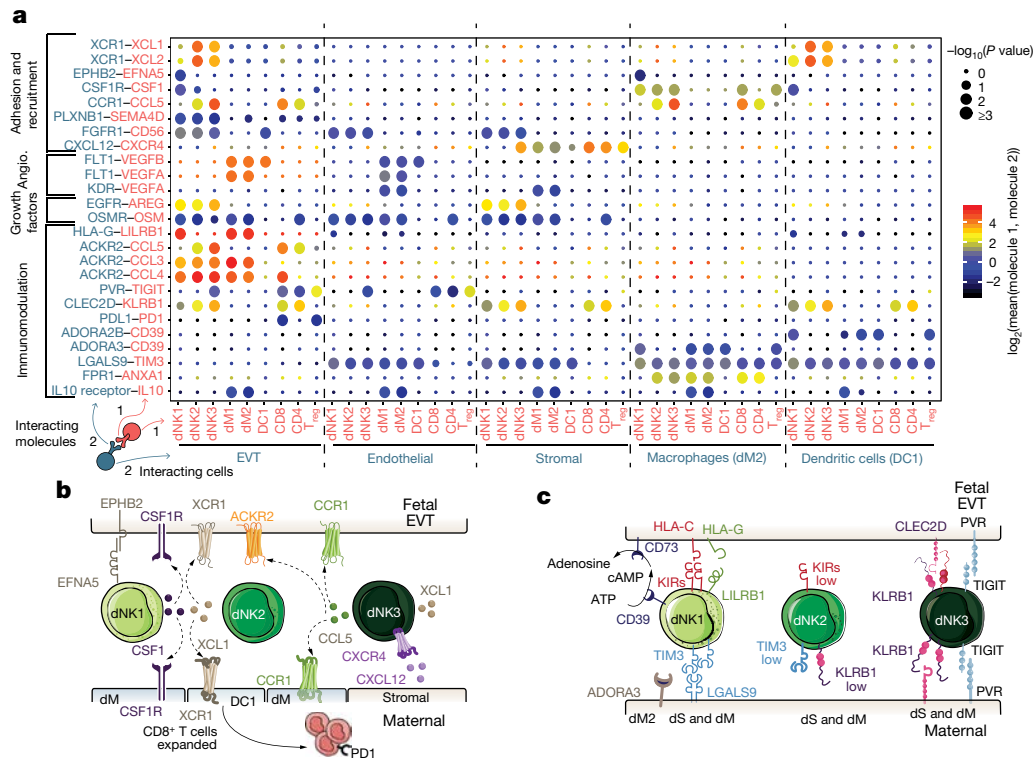


Fig. 5 | Multiple regulatory immune responses at the site of placentation. a, Overview of selected ligand–receptor interactions; *P* values indicated by circle size, scale on right (permutation test, see Methods). The means of the average expression level of interacting molecule 1 in cluster 1 and interacting molecule 2 in cluster 2 are indicated by colour. Only droplet data were used ($n = 6$ deciduals).

dNK1 cells express higher levels of *CSF1*, the receptor of which (*CSF1R*) is expressed by EVT and macrophages (Fig. 5a, b). Secretion of *CSF1* by dNK cells and interaction with the *CSF1R* on EVT have previously been described^{28,29}, and we now pinpoint this interaction specifically to the dNK1 subset. By contrast, dNK2 and dNK3 express high levels of *XCL1*, and *CCL5* is highly expressed by dNK3 (Fig. 5a, b, Extended Data Fig. 9b). *CCR1*, the receptor for *CCL5*, is expressed by EVT, which suggests a role for dNK3 in regulating EVT invasion³⁰. The expression pattern of the *XCL1–XCR1* ligand–receptor complex suggests functional interactions between dNK2 and dNK3 and both EVT and conventional DC1 (labelled as DC1). DC1 recruitment, which is mediated by natural killer cells, occurs in tumour microenvironments³¹. We find an increased proportion of DC1 compared to DC2—which possibly leads to the expansion of decidual CD8⁺ T cells (Fig. 1d)—but co-expression of *PD1* (also known as *PDCD1*) suggests that local T cell activation is limited.

Our results collectively suggest that in the decidua microenvironment all damaging maternal T or natural killer cell responses to fetal trophoblast cells are prevented. There is high expression of *PDL1* (also known as *CD274*) in EVT, which we confirmed in situ by using immunohistochemistry on serial sections of decidua basalis (the site of trophoblast invasion) stained for *PDL1* and *HLA-G* (Extended Data Fig. 9c). We also identified putative inhibitory interactions between dNKs and EVT, in addition to the previously discussed receptor–ligand complexes between *KIR2DL1*, *KIR2DL2* or *KIR2DL3* and *HLA-C*. These include *KLRB1* and *TIGIT*, which are highly expressed by dNK3 cells, potentially binding *CLEC2D* and *PVR*, which are expressed by EVT (Fig. 5a).

We predict that the immune microenvironment of the decidua prevents inflammatory responses that could potentially be triggered by trophoblast invasion and destruction of the smooth muscle media of the spiral arteries by trophoblast (Fig. 5c). Subsets of decidual macrophages

express immunomodulatory molecules such as *IL10*, the receptor of which is expressed by EVT and by maternal endothelial, stromal and myeloid cells. dNK1 cells express high levels of *SPINK2*, and dNK2 and dNK3 cells express high levels of *ANXA1*. Both of these genes encode proteins that have anti-inflammatory roles, such as inhibiting kallikreins³². The dNK1 subset expresses *CD39* (which is encoded by *NT5E*), which—together with *CD73* (which is encoded by *NT5E*)—converts ATP to adenosine to prevent immune activation³³ (Fig. 5c, Extended Data Fig. 9b). Expression of *CD73* is high in epithelial glands and EVT, and the adenosine receptor (*ADORA3*) is present in macrophages (Fig. 5c, Extended Data Fig. 9b). *KIR2DL1*⁺ dNK1 cells are in close physical contact with *HLA-G*⁺ EVT (Extended Data Fig. 9d), which suggests that together they could convert extracellular ATP—an inflammatory signal released upon cell death—to adenosine³⁴.

Discussion

Reproductive success depends on events that occur during placentation in the first-trimester decidua³⁵. Other scRNA-seq studies of uterine cells in pregnancy have analysed cells at the end of gestation^{16,36} or are restricted to fetal placental populations¹⁷. To our knowledge, our study is the first comprehensive single-cell transcriptomics atlas of the maternal–fetal interface between 6–14 weeks of gestation (Extended Data Fig. 10). Similar to previous scRNA-seq analyses^{36–39}, we predict possible ligand–receptor interactions; we have developed an open repository for this purpose (www.CellPhoneDB.org/). This database accounts for the multimeric nature of ligands and receptors and is integrated with a statistical framework that predicts enriched cellular interactions between two cell types.

We show the differentiation trajectory of trophoblast cells to either villous syncytiotrophoblast (which is involved in nutrient exchange) or EVT (which invade and remodel the spiral arteries), and predict the ligand–receptor interactions that are likely to control these processes.

Our findings also suggest an environment in which any adaptive or innate immune responses that are harmful to the placenta or to the uterus are minimized. This is critical for the compromise that is needed to define the territorial boundary between mother and fetus. This environment has notable parallels with that around tumours, where inflammatory and adaptive immune responses are also dampened⁴⁰. dNK cells comprise about 70% of immune cells in the first-trimester decidua^{41,42}; we define three major subsets of dNK cells and predict that their likely function is to mediate the extent of trophoblast invasion, in addition to coordinating multiple immunomodulatory pathways that involve myeloid cells, T cells and stromal cells. Maternal immune responses are restrained by diverse classes of signalling molecules: cell-surface expression of checkpoint inhibitors such as PD1, PDL1 or TIGIT, tethered ligand–receptor complexes, secreted proteins, and small molecules such as adenosine or steroid hormones. We also show that the dNK1 subset expresses receptors for trophoblast HLA-C, HLA-E and HLA-G molecules, and can be primed metabolically through increased expression of glycolytic enzymes. The increased expression of glycolytic enzymes in dNK1 cells (which represents metabolic priming) suggests that these cells could be responsible for the different reproductive outcomes found in first compared to subsequent pregnancies.

In summary, we identify many molecular and cellular mechanisms that operate to generate a physiologically peaceful decidual environment. This cell atlas of the early maternal–fetal interface provides an essential resource for understanding normal and pathological pregnancies.

Online content

Any methods, additional references, Nature Research reporting summaries, source data, statements of data availability and associated accession codes are available at <https://doi.org/10.1038/s41586-018-0698-6>.

Received: 30 March 2018; Accepted: 15 October 2018;

Published online: 14 November 2018

- Ramathal, C. Y., Bagchi, I. C., Taylor, R. N. & Bagchi, M. K. Endometrial decidualization: of mice and men. *Semin. Reprod. Med.* **28**, 17–26 (2010).
- Koopman, L. A. et al. Human decidual natural killer cells are a unique NK cell subset with immunomodulatory potential. *J. Exp. Med.* **198**, 1201–1212 (2003).
- Burton, G. J., Watson, A. L., Hempstock, J., Skepper, J. N. & Jauniaux, E. Uterine glands provide histiotrophic nutrition for the human fetus during the first trimester of pregnancy. *J. Clin. Endocrinol. Metab.* **87**, 2954–2959 (2002).
- Hempstock, J., Cindrova-Davies, T., Jauniaux, E. & Burton, G. J. Endometrial glands as a source of nutrients, growth factors and cytokines during the first trimester of human pregnancy: a morphological and immunohistochemical study. *Reprod. Biol. Endocrinol.* **2**, 58 (2004).
- Burton, G. J., Woods, A. W., Jauniaux, E. & Kingdom, J. C. P. Rheological and physiological consequences of conversion of the maternal spiral arteries for uteroplacental blood flow during human pregnancy. *Placenta* **30**, 473–482 (2009).
- Fisher, S. J. Why is placental abnormal in preeclampsia? *Am. J. Obstet. Gynecol.* **213**, S115–S122 (2015).
- Jauniaux, E. & Burton, G. J. Placenta accreta spectrum: a need for more research on its aetiopathogenesis. *BJOG* **125**, 1449–1450 (2018).
- Apps, R., Gardner, L. & Moffett, A. A critical look at HLA-G. *Trends Immunol.* **29**, 313–321 (2008).
- Apps, R. et al. Human leucocyte antigen (HLA) expression of primary trophoblast cells and placental cell lines, determined using single antigen beads to characterize allotype specificities of anti-HLA antibodies. *Immunology* **127**, 26–39 (2009).
- Sharkey, A. M. et al. Killer Ig-like receptor expression in uterine NK cells is biased toward recognition of HLA-C and alters with gestational age. *J. Immunol.* **181**, 39–46 (2008).
- Parham, P. & Moffett, A. Variable NK cell receptors and their MHC class I ligands in immunity, reproduction and human evolution. *Nat. Rev. Immunol.* **13**, 133–144 (2013).
- Moffett, A. & Colucci, F. Co-evolution of NK receptors and HLA ligands in humans is driven by reproduction. *Immunol. Rev.* **267**, 283–297 (2015).
- Zheng, G. X. Y. et al. Massively parallel digital transcriptional profiling of single cells. *Nat. Commun.* **8**, 14049 (2017).
- Picelli, S. et al. Full-length RNA-seq from single cells using Smart-seq2. *Nat. Protocols* **9**, 171–181 (2014).
- Burton, G. J. & Watson, A. L. The structure of the human placenta: implications for initiating and defending against virus infections. *Rev. Med. Virol.* **7**, 219–228 (1997).

- Tsang, J. C. H. et al. Integrative single-cell and cell-free plasma RNA transcriptomics elucidates placental cellular dynamics. *Proc. Natl Acad. Sci. USA* **114**, E7786–E7795 (2017).
- Liu, Y. et al. Single-cell RNA-seq reveals the diversity of trophoblast subtypes and patterns of differentiation in the human placenta. *Cell Res.* **28**, 819–832 (2018).
- Madigan, J. et al. Chemokine scavenger D6 is expressed by trophoblasts and aids the survival of mouse embryos transferred into allogeneic recipients. *J. Immunol.* **184**, 3202–3212 (2010).
- Mariathasan, S. et al. TGF β attenuates tumour response to PD-L1 blockade by contributing to exclusion of T cells. *Nature* **554**, 544–548 (2018).
- Maltepe, E. & Fisher, S. J. Placenta: the forgotten organ. *Annu. Rev. Cell Dev. Biol.* **31**, 523–552 (2015).
- Bolnick, J. M. et al. Altered biomarkers in trophoblast cells obtained noninvasively prior to clinical manifestation of perinatal disease. *Sci. Rep.* **6**, 32382 (2016).
- Lucas, E. S. et al. Reconstruction of the decidual pathways in human endometrial cells using single-cell RNA-seq. Preprint at <https://www.biorxiv.org/content/early/2018/07/13/368829> (2018).
- Muñoz-Fernández, R. et al. Human predecidual stromal cells have distinctive characteristics of pericytes: cell contractility, chemotactic activity, and expression of pericyte markers and angiogenic factors. *Placenta* **61**, 39–47 (2018).
- Gamliel, M. et al. Trained memory of human uterine NK cells enhances their function in subsequent pregnancies. *Immunity* **48**, 951–962 (2018).
- Kozuki, N. et al. The associations of parity and maternal age with small-for-gestational-age, preterm, and neonatal and infant mortality: a meta-analysis. *BMC Public Health* **13**, S2 (2013).
- Cichocki, F. et al. ARID5B regulates metabolic programming in human adaptive NK cells. *J. Exp. Med.* **215**, 2379–2395 (2018).
- Hanna, J. et al. Decidual NK cells regulate key developmental processes at the human fetal–maternal interface. *Nat. Med.* **12**, 1065–1074 (2006).
- Jokhi, P. P., King, A., Boocock, C. & Loke, Y. W. Secretion of colony stimulating factor-1 by human first trimester placental and decidual cell populations and the effect of this cytokine on trophoblast thymidine uptake in vitro. *Hum. Reprod.* **10**, 2800–2807 (1995).
- Hamilton, G. S., Lysiak, J. J., Watson, A. J. & Lala, P. K. Effects of colony stimulating factor-1 on human extravillous trophoblast growth and invasion. *J. Endocrinol.* **159**, 69–77 (1998).
- Sato, Y. et al. Trophoblasts acquire a chemokine receptor, CCR1, as they differentiate towards invasive phenotype. *Development* **130**, 5519–5532 (2003).
- Böttcher, J. P. et al. NK cells stimulate recruitment of cDC1 into the tumor microenvironment promoting cancer immune control. *Cell* **172**, 1022–1037 (2018).
- Sotiropoulou, G. & Pampalakis, G. Kallikrein-related peptidases: bridges between immune functions and extracellular matrix degradation. *Biol. Chem.* **391**, 321–331 (2010).
- Takenaka, M. C., Robson, S. & Quintana, F. J. Regulation of the T cell response by CD39. *Trends Immunol.* **37**, 427–439 (2016).
- Vijayan, D., Young, A., Teng, M. W. L. & Smyth, M. J. Targeting immunosuppressive adenosine in cancer. *Nat. Rev. Cancer* **17**, 709–724 (2017).
- Smith, G. C. S. First-trimester determination of complications of late pregnancy. *J. Am. Med. Assoc.* **303**, 561–562 (2010).
- Pavličev, M. et al. Single-cell transcriptomics of the human placenta: inferring the cell communication network of the maternal–fetal interface. *Genome Res.* **27**, 349–361 (2017).
- Camp, J. G. et al. Multilineage communication regulates human liver bud development from pluripotency. *Nature* **546**, 533–538 (2017).
- Puram, S. V. et al. Single-cell transcriptomic analysis of primary and metastatic tumor ecosystems in head and neck cancer. *Cell* **171**, 1611–1624 (2017).
- Skelly, D. A. et al. Single-cell transcriptional profiling reveals cellular diversity and intercommunication in the mouse heart. *Cell Reports* **22**, 600–610 (2018).
- Pardoll, D. M. The blockade of immune checkpoints in cancer immunotherapy. *Nat. Rev. Cancer* **12**, 252–264 (2012).
- Bulmer, J. N., Morrison, L., Longfellow, M., Ritson, A. & Pace, D. Granulated lymphocytes in human endometrium: histochemical and immunohistochemical studies. *Hum. Reprod.* **6**, 791–798 (1991).
- King, A., Wellings, V., Gardner, L. & Loke, Y. W. Immunocytochemical characterization of the unusual large granular lymphocytes in human endometrium throughout the menstrual cycle. *Hum. Immunol.* **24**, 195–205 (1989).

Acknowledgements We thank G. Graham, J. Shilts, A. Lopez, N. Reuter, S. Orchard and P. Porras for discussions on CellPhoneDB; D. Dixon, D. Popescu, J. Fletcher, O. Chazara, L. Mamanova, A. Jinat, C. I. Mazzeo, D. McDonald and D. Bulmer for experimental help; A. Hupalowska for help with the illustrations; S. Lindsay, A. Farnworth, the HDBR, P. Ayuk and the Newcastle Uteroplacental Tissue Bank for providing samples; R. Rostom, D. McCarthy, V. Svensson, M. Hemberg and T. Gomes for computational discussions. We are indebted to the donors for participating in this research. This project was supported by ERC grants (ThDEFINE, ThSWITCH) and an EU

FET-OPEN grant (MRG-GRAMMAR no. 664918) and Wellcome Sanger core funding (no. WT206194). R.V.-T. is supported by an EMBO and HFSP Long-Term Fellowship and J.-E.P. by an EMBO Long-Term Fellowship; M.Y.T. holds a Royal Society Dorothy Hodgkin Fellowship and A.M. has a Wellcome Trust Investigator award. The human embryonic and fetal material was provided by the Joint MRC/Wellcome Trust (MR/R006237/1) HDBR.

Reviewer information *Nature* thanks B. Treutlein and the other anonymous reviewer(s) for their contribution to the peer review of this work.

Author contributions R.V.-T. and S.A.T. conceived the study. Sample and library preparation was performed by R.V.-T. with contributions from M.Y.T., J.-E.P., E.S. and S.L.; FACS experiments were performed by R.V.-T., R.A.B., A.F., A.M.S., R.P.P. and M.A.I.; histology staining was performed by J.N.B., L.G., R.V.-T., M.Y.T., B.M., B.I., S.H., D.H.R. and A.W.-C.; M.E. and R.V.-T. analysed and interpreted the data with contributions from M.V.-T., M.J.T.S., L.W., G.J.W., A.G., A.Z., J.H., K.B.M.,

K.P., M.H., A.M. and S.A.T.; R.V.-T., A.M. and S.A.T. wrote the manuscript with contributions from M.H., M.E., K.B.M. and M.Y.T.; M.H., A.M. and S.A.T. co-directed the study. All authors read and accepted the manuscript.

Competing interests The authors declare no competing interests.

Additional information

Extended data is available for this paper at <https://doi.org/10.1038/s41586-018-0698-6>.

Supplementary information is available for this paper at <https://doi.org/10.1038/s41586-018-0698-6>.

Reprints and permissions information is available at <http://www.nature.com/reprints>.

Correspondence and requests for materials should be addressed to M.H., A.M. or S.A.T.

Publisher's note: Springer Nature remains neutral with regard to jurisdictional claims in published maps and institutional affiliations.

METHODS

No statistical methods were used to predetermine sample size. The experiments were not randomized and investigators were not blinded to allocation during experiments and outcome assessment.

Patient samples. All tissue samples used for this study were obtained with written informed consent from all participants in accordance with the guidelines in The Declaration of Helsinki 2000 from multiple centres.

Human embryo, fetal and decidual samples were obtained from the MRC and Wellcome-funded Human Developmental Biology Resource (HDBR⁴³, <http://www.hdb.org>), with appropriate maternal written consent and approval from the Newcastle and North Tyneside NHS Health Authority Joint Ethics Committee (08/H0906/21+5). The HDBR is regulated by the UK Human Tissue Authority (HTA; www.hta.gov.uk) and operates in accordance with the relevant HTA Codes of Practice. Decidual tissue for smFISH (Extended Data Fig. 7c) was also covered by this ethics protocol.

Peripheral blood from women undergoing elective terminations was collected under appropriate maternal written consent and with approvals from the Newcastle Academic Health Partners (reference NAHPB-093) and HRA NHS Research Ethics committee North-East-Newcastle North Tyneside 1 (REC reference 12/NE/0395)

Decidual tissue for immunohistochemistry (Fig. 3b, c, Extended Data Figs. 7a, 9c, d) and flow cytometry staining for granule proteins was obtained from elective terminations of normal pregnancies at Addenbrooke's Hospital (Cambridge) between 6 and 12 weeks gestation, under ethical approval from the Cambridge Local Research Ethics Committee (04/Q0108/23).

Decidual tissue for smFISH (Fig. 3d, Extended Data Fig. 6b, 7b) was obtained from the Newcastle Uteroplacental Tissue Bank. Ethics numbers are: Newcastle and North Tyneside Research Ethics Committee 1 Ref:10/H0906/71 and 16/NE/0167.

Isolation of decidual, placental and blood cells. Decidual and placental tissue was washed in Ham's F12 medium, macroscopically separated and then washed for at least 10 min in RPMI or Ham's F12 medium, respectively, before processing.

Decidual tissues were chopped using scalpels into approximately 0.2-mm³ cubes and enzymatically digested in 15 ml 0.4 mg/ml collagenase V (Sigma, C-9263) solution in RPMI 1640 medium (Thermo Fisher Scientific, 21875-034)/10% FCS (Biosera, FB-1001) at 37°C for 45 min. The supernatant was diluted with medium and passed through a 100-µm cell sieve (Corning, 431752) and then a 40-µm cell sieve (Corning, 431750). The flow-through was centrifuged and resuspended in 5 ml of red blood cell lysis buffer (Invitrogen, 00-4300) for 10 min.

Each first-trimester placenta was placed in a Petri dish and the placental villi were scraped from the chorionic membrane using a scalpel. The stripped membrane was discarded and the resultant villous tissue was enzymatically digested in 70 ml 0.2% trypsin 250 (Pan Biotech P10-025100P)/0.02% EDTA (Sigma E9884) in PBS with stirring at 37°C for 9 min. The disaggregated cell suspension was passed through sterile muslin gauze (Winware food grade) and washed through with Ham's F12 medium (Biosera SM-H0096) containing 20% FBS (Biosera FB-1001). Cells were pelleted from the filtrate by centrifugation and resuspended in Ham's F12. The undigested gelatinous tissue remnant was retrieved from the gauze and further digested with 10–15 ml collagenase V at 1.0 mg/ml (Sigma C9263) in Ham's F12 medium/10% FBS with gentle shaking at 37°C for 10 min. The disaggregated cell suspension from collagenase digestion was passed through sterile muslin gauze and the cells pelleted from the filtrate as before. Cells obtained from both enzyme digests were pooled together and passed through a 100-µm cell sieve (Corning, 431752) and washed in Ham's F12. The flow-through was centrifuged and resuspended in 5 ml of red blood cell lysis buffer (Invitrogen, 00-4300) for 10 min.

Blood samples were carefully layered onto a Ficoll–Paque gradient (Amersham) and centrifuged at 2,000 r.p.m. for 30 min without breaks. Peripheral blood mononuclear cells from the interface between the plasma and the Ficoll–Paque gradient were collected and washed in ice-cold phosphate-buffered saline (PBS), followed by centrifugation at 2,000 r.p.m. for 5 min. The pellet was resuspended in 5 ml of red blood cell lysis buffer (Invitrogen, 00-4300) for 10 min.

Assignment of fetal developmental stage. Up to eight post-conception weeks, embryos are staged using the Carnegie staging method⁴⁴. At fetal stages beyond eight post-conception weeks, age was estimated from measurements of foot length and heel-to-knee length. These were compared with a standard growth chart⁴⁵.

Flow cytometry staining, cell sorting and single-cell RNA-seq. Decidual and blood cells were incubated at 4°C with 2.5 µl of antibodies in 1% FBS in DPBS without calcium and magnesium (Thermo Fisher Scientific, 14190136). DAPI was used for live versus dead discrimination. We used an antibody panel designed to enrich for certain populations for single-cell sorting and scRNA-seq. Cells were sorted using a Becton Dickinson (BD) FACS Aria Fusion with 5 excitation lasers (355 nm, 405 nm, 488 nm, 561 nm and 635 nm red), and 18 fluorescent detectors, plus forward and side scatter. The sorter was controlled using BD FACS DIVA software (version 7). The antibodies used are listed in Supplementary Table 10.

For single-cell RNA-seq using the plate-based Smart-seq2 protocol, we created overlapping gates that comprehensively and evenly sampled all immune-cell

populations in the decidua (Extended Data Fig. 1). B cells (CD19⁺ or CD20⁺) were excluded from our analysis, owing to their absence in decidua⁴⁶. Single cells were sorted into 96-well full-skirted Eppendorf plates chilled to 4°C, prepared with lysis buffer consisting of 10 µl of TCL buffer (Qiagen) supplemented with 1% β-mercaptoethanol. Single-cell lysates were sealed, vortexed, spun down at 300g at 4°C for 1 min, immediately placed on dry ice and transferred for storage at –80°C. The Smart-seq2 protocol was performed on single cells as previously described^{11,47}, with some modifications⁴⁸. Libraries were sequenced, aiming at an average depth of 1 million reads per cell, on an Illumina HiSeq 2000 with version 4 chemistry (paired-end, 75-bp reads).

For the droplet scRNA-seq methods, blood and decidual cells were sorted into immune (CD45⁺) and non-immune (CD45[–]) fractions. B cells (CD19⁺ or CD20⁺) were excluded from blood analysis, owing to their absence in decidua⁴⁶. Only viable cells were considered. Placental cells were stained for DAPI and only viable cells were sorted. To improve trophoblast trajectories, an additional enrichment of EPCAM⁺ and HLA-G⁺ was performed for selected samples (Fig. 2 only). Cells were sorted into an Eppendorf tube containing PBS with 0.04% BSA. Cells were immediately counted using a Neubauer haemocytometer and loaded in the 10x-Genomics Chromium. The 10x-Genomics v2 libraries were prepared as per the manufacturer's instructions. Libraries were sequenced, aiming at a minimum coverage of 50,000 raw reads per cell, on an Illumina HiSeq 4000 (paired-end; read 1: 26 cycles; i7 index: 8 cycles, i5 index: 0 cycles; read 2: 98 cycles).

Flow cytometry staining for granule proteins. For intracellular staining of granule proteins, dNKs were surface-stained for 30 min in FACS buffer with antibodies (listed in Supplementary Table 10). Cells were washed with FACS buffer followed by staining with dead cell marker (DCM Aqua) and streptavidin Qdot605. dNKs were then treated with FIX & PERM (Thermo Fisher Scientific) and stained for granule proteins. Samples were run on an LSRFortessa FACS analyser (BD Biosciences) and data analysed using FlowJo (Tree Star). dNKs were gated as CD3[–]CD14[–]CD19[–] live cells; CD56⁺NKG2A⁺ and then KIR⁺ and KIR[–] subsets were generated using Boolean functions with the gates for all the different KIRs stained (KIR⁺), and their inverse gates (KIR[–]). Wilcoxon test was used to compare granule protein staining between paired dNK subsets from the same donor. A *P* value < 0.05 was considered to be statistically significant.

Immunohistochemistry. Four-micrometre tissue sections from formalin-fixed, paraffin-wax-embedded human decidual and placental tissues were dewaxed with Histoclear, cleared in 100% ethanol and rehydrated through gradients of ethanol to PBS. Sections were blocked with 2% serum (of species in which the secondary antibody was made) in PBS, incubated with primary antibody overnight at 4°C and slides were washed in PBS. Biotinylated horse anti-mouse or goat anti-rabbit secondary antibodies were used, followed by Vectastain ABC-HRP reagent (Vector, PK-6100) and developed with di-aminobenzidine (DAB) substrate (Sigma, D4168). Sections were counterstained with Carazzi's haematoxylin and mounted in glycerol and gelatin mounting medium (Sigma, GG1-10). Primary antibody was replaced with equivalent concentrations of mouse or rabbit IgG for negative controls. See Supplementary Table 10 for antibody information. Tissue sections were imaged using a Zeiss Axiovert Z1 microscope and Axiovision imaging software SE64 version 4.8.

smFISH. Samples were fixed in 10% NBF, dehydrated through an ethanol series and embedded in paraffin wax. Five-millimetre samples were cut, baked at 60°C for 1 h and processed using standard pre-treatment conditions, as per the RNAScope multiplex fluorescent reagent kit version 2 assay protocol (manual) or the RNAScope 2.5 LS fluorescent multiplex assay (automated). TSA-plus fluorescein, Cy3 and Cy5 fluorophores were used at 1:1,500 dilution for the manual assay or 1:300 dilution for the automated assay. Slides were imaged on different microscopes: Hamamatsu Nanoscope S60 (Extended Data Fig. 7c). Zeiss Cell Discoverer 7 (Fig. 4d, Extended Data Figs. 6, 7c). Filter details were as follows. DAPI: excitation 370–400, BS 394, emission 460–500; FITC: excitation 450–488, BS 490, emission 500–55; Cy3: excitation 540–570, BS 573, emission 540–570; Cy5: excitation 615–648, BS 691, emission 662–756. The camera used was a Hamamatsu ORCA-Flash4.0 V3 sCMOS camera.

Whole-genome sequencing. Tissue DNA and RNA were extracted from fresh-frozen samples using the AllPrep DNA/RNA/miRNA kit (Qiagen), following the manufacturer's instructions. Short insert (500-bp) genomic libraries were constructed, flowcells were prepared and 150-bp paired-end sequencing clusters generated on the Illumina HiSeq X platform, according to Illumina no-PCR library protocols, to an average of 30× coverage. Genotype information is provided in Supplementary Table 1.

Single cell RNA-seq data analysis. Droplet-based sequencing data were aligned and quantified using the Cell Ranger Single-Cell Software Suite (version 2.0, 10x Genomics)¹³ against the GRCh38 human reference genome provided by Cell Ranger. Cells with fewer than 500 detected genes and for which the total mitochondrial gene expression exceeded 20% were removed. Mitochondrial genes and genes that were expressed in fewer than three cells were also removed.

SmartSeq2 sequencing data were aligned with HISAT2⁴⁹, using the same genome reference and annotation as the 10x Genomics data. Gene-specific read counts were calculated using HTSeq-count⁵⁰. Cells with fewer than 1,000 detected genes and more than 20% mitochondrial gene expression content were removed. Furthermore, mitochondrial genes and genes expressed in fewer than three cells were also removed. To remove batch effects due to background contamination of cell free RNA, we also removed a set of genes that had a tendency to be expressed in ambient RNA (*PAEP*, *HBG1*, *HBA1*, *HBA2*, *HBM*, *AHSP* and *HBG2*).

Downstream analyses—such as normalization, shared nearest neighbour graph-based clustering, differential expression analysis and visualization—were performed using the R package Seurat⁵¹ (version 2.3.3). Droplet-based and SmartSeq2 data were integrated using canonical correlation analysis, implemented in the Seurat alignment workflow⁵². Cells, the expression profile of which could not be well-explained by low-dimensional canonical correlation analysis compared to low-dimensional principal component analysis, were discarded, as recommended by the Seurat alignment tutorial. Clusters were identified using the community identification algorithm as implemented in the Seurat 'FindClusters' function. The shared nearest neighbour graph was constructed using between 5 and 40 canonical correlation vectors as determined by the dataset variability; the resolution parameter to find the resulting number of clusters was tuned so that it produced a number of clusters large enough to capture most of the biological variability. UMAP analysis was performed using the RunUMAP function with default parameters. Differential expression analysis was performed based on the Wilcoxon rank-sum test. The *P* values were adjusted for multiple testing using the Bonferroni correction. Clusters were annotated using canonical cell-type markers. Two clusters of peripheral blood monocytes represented the same cell type and were therefore merged.

We further removed contaminating cells: (i) maternal stromal cells that were gathered in the placenta for one of the fetuses; (ii) a shared decidua-placental cluster with fetal cells mainly present in two fetuses (which we think is likely to be contaminating cells from other fetal tissues due to the surgical procedure). This can occur owing to the source of the tissue and the trauma of surgery. We also removed a cluster for which the top markers were genes associated with dissociation-induced effects⁵³. Each of the remaining clusters contained cells from multiple different fetuses, indicating that the cell types and states we observed are not affected by batch effects.

We found further diversity within the T cell clusters, as well as the clusters of endothelial, epithelial and perivascular cells, which we then reanalysed and partitioned separately, using the same alignment and clustering procedure.

The trophoblast clusters (clusters 1, 9, 20, 13 and 16 from Fig. 1d) were taken from the initial analysis of all cells and merged with the enriched EPCAM⁺ and HLA-G⁺ cells. The droplet-based and Smart-seq2 datasets were integrated and clustered using the same workflow as described above. Only cells that were identified as trophoblast were considered for trajectory analysis.

Trajectory modelling and pseudotemporal ordering of cells was performed with the monocle 2 R package⁵⁴ (version 2.8.0). The most highly variable genes were used for ordering the cells. To account for the cell-cycle heterogeneity in the trophoblast subpopulations, we performed hierarchical clustering of the highly variable genes and removed the set of genes that cluster with known cell-cycle genes such as *CDK1*. Genes which changed along the identified trajectory were identified by performing a likelihood ratio test using the function differentialGeneTest in the monocle 2 package.

Network visualization was done using Cytoscape (version 3.5.1). The decidua network was created considering only edges with more than 30 interactions. The networks layout was set to force-directed layout.

KIR typing. Polymerase chain reaction sequence-specific primer was performed to amplify the genomic DNA for presence or absence of 12 KIR genes (*KIR2DL1*, *KIR2DL2*, *KIR2DL3*, *KIR2DL5* (both *KIR2DL5A* and *KIR2DL5B*), *KIR3DL1*, *KIR2DS1*, *KIR2DS2*, *KIR2DS3*, *KIR2DS4*, *KIR2DS5* and *KIR3DS1*) and the pseudo-gene *KIR2DP1*. *KIR2DS4* alleles were also typed as being either full-length or having the 22-bp deletion that prevents cell-surface expression. Two pairs of primers were used for each gene, selected to give relatively short amplicons of 100–800 bp, as previously described⁵⁵. Extra KIR primers were designed using sequence information from the IPD-KIR database (release 2.4.0) to detect rare alleles of *KIR2DS5* and *KIR2DL3* (*KIR2DS5*, 2DS5rev2: TCC AGA GGG TCA CTG GGA and *KIR2DL3*, 2DL3rev3: AGA CTC TTG GTC CAT TAC CG)⁵⁶. KIR haplotypes were defined by matrix subtraction of gene copy numbers using previously characterized common and contracted KIR haplotypes using the KIR Haplotype Identifier software (www.bioinformatics.cimr.cam.ac.uk/haplotypes).

Inferring maternal or fetal origin of single cells from droplet-based scRNA-seq using whole-genome sequencing variant calls. To match the processing of the whole-genome sequencing datasets, droplet-based sequencing data from decidua and placenta samples were realigned and quantified against the GRCh37 human reference genome using the Cell Ranger Single-Cell Software Suite (version 2.0)¹³. The fetal or maternal origin of each barcoded cell was then determined using the

tool demuxlet⁵⁷. In brief, demuxlet can be used to deconvolve droplet-based scRNA-seq experiments in which cells are pooled from multiple genetically distinct individuals. Given a set of genotypes corresponding to these individuals, demuxlet infers the most likely genetic identity of each droplet by estimating the likelihood of observing scRNA-seq reads from the droplet overlapping known single nucleotide polymorphisms. Demuxlet inferred the identities of cells in this study by analysing each Cell Ranger-aligned BAM file from decidua and placenta in conjunction with a VCF file, containing the high-quality whole-genome-sequence variant calls from the corresponding mother and fetus. Each droplet was assigned to be maternal, fetal or unknown in origin (ambiguous or a potential doublet), and these identities were then linked with the transcriptome-based cell clustering data to confirm the maternal and fetal identity of each annotated cell type.

T cell receptor analysis by TraCeR. The T cell receptor sequences for each single T cell were assembled using TraCeR⁵⁸, which allowed the reconstruction of the T cell receptors from scRNA-seq data and their expression abundance (transcripts per million), as well as identification of the size, diversity and lineage relation of clonal subpopulations. In total, we obtained the T cell receptor sequences for 1,482 T cells with at least one paired productive $\alpha\beta$ or $\gamma\delta$ chain. Cells for which more than two recombinants were identified for a particular locus were excluded from further analysis.

Whole-genome sequencing alignment and variant calling. Maternal and fetal whole-genome sequencing data were mapped to the GRCh37.p13 reference genome using BWA-MEM version 0.7.15⁵⁹. The SAMtools⁶⁰ fixmate utility (version 1.5) was used to update read-pairing information and mate-related flags. Reads near known indels from the Mills⁶¹ and 1000G⁶² gold standard reference set for hg19/GRCh37 were locally realigned using GATK IndelRealigner version 3.7⁶¹. Base-calling assessment and base-quality scores were adjusted with GATK BaseRecalibrator and PrintReads version 3.7^{60,63}. PCR duplicates were identified and removed using Picard MarkDuplicates version 2.14.1^{63,64}. Finally, bcftools mpileup and call version 1.6⁶⁵ were used to produce genotype likelihoods and output called variants at all known biallelic single nucleotide polymorphism sites that overlap protein-coding genes. For each sample, variants called with phred-scale quality score ≥ 200 , at least 20 supporting reads and mapping quality ≥ 60 were retained as high-quality variants.

Quantification of KIR gene expression by KIRid. The KIR locus is highly polymorphic in terms of both numbers of genes and alleles¹¹. Including a single reference sequence for each gene can lead to reference bias for donors that happen to better match the reference sequence. To address these issues, we used a tailored approach in which we first built a total cDNA reference by concatenating the Ensembl coding and non-coding transcript sequences, excluding transcripts belonging to the KIR genes (GRCh38, version 90), and the full set of known KIR cDNAs sequences from the IPD-KIR database⁶⁶ (release 2.7.0). For each donor, we removed transcript sequences for KIR genes determined to be absent in that individual, which decreases the extent of multi-mapping and quantification. The single-cell reads of each donor were then mapped to the corresponding donor-specific reference using Kallisto⁶⁷ (version 0.43.0 with default options). Expression levels were quantified using the multi-mapping deconvolution tool MMSEQ⁶⁸, and gene-level estimates were obtained by aggregating over different alleles for each KIR gene.

Cell-cell communication analysis. To enable a systematic analysis of cell-cell communication molecules, we developed CellPhoneDB, a public repository of ligands, receptors and their interactions. Our repository relies on the use of public resources to annotate receptors and ligands. We include subunit architecture for both ligands and receptors, to accurately represent heteromeric complexes.

Ligand-receptor pairs are defined based on physical protein-protein interactions (see sections of 'CellPhoneDB annotations'). We provide CellPhoneDB with a user-friendly web interface at www.CellPhoneDB.org, where the user can search for ligand-receptor complexes and interrogate their own single-cell transcriptomics data.

To assess cellular crosstalk between different cell types, we used our repository in a statistical framework for inferring cell-cell communication networks from single-cell transcriptome data. We derived enriched receptor-ligand interactions between two cell types based on expression of a receptor by one cell type and a ligand by another cell type, using the droplet-based data. To identify the most relevant interactions between cell types, we looked for the cell-type specific interactions between ligands and receptors. Only receptors and ligands expressed in more than 10% of the cells in the specific cluster were considered.

We performed pairwise comparisons between all cell types. First, we randomly permuted the cluster labels of all cells 1,000 times and determined the mean of the average receptor expression level of a cluster and the average ligand expression level of the interacting cluster. For each receptor-ligand pair in each pairwise comparison between two cell types, this generated a null distribution. By calculating the proportion of the means which are 'as or more extreme' than the actual mean, we obtained a *P* value for the likelihood of cell-type specificity of a given receptor-ligand

complex. We then prioritized interactions that are highly enriched between cell types based on the number of significant pairs, and manually selected biologically relevant ones. For the multi-subunit heteromeric complexes, we required that all subunits of the complex are expressed (using a threshold of 10%), and therefore we used the member of the complex with the minimum average expression to perform the random shuffling.

CellPhoneDB annotations of membrane, secreted and peripheral proteins. Secreted proteins were downloaded from Uniprot using KW-0964 (secreted). Secreted proteins were annotated as cytokines (KW-0202), hormones (KW-0372), growth factors (KW-0339) and immune-related using Uniprot keywords and manual annotation. Cytokines, hormones, growth factors and other immune-related proteins were annotated as 'secreted highlight' proteins in our lists.

Plasma membrane proteins were downloaded from Uniprot using KW-1003 (cell membrane). Peripheral proteins from the plasma membrane were annotated using the Uniprot Keyword SL-9903, and the remaining proteins were annotated as transmembrane proteins. We completed our lists of plasma transmembrane proteins by doing an extensive manual curation using literature mining and Uniprot description of proteins with transmembrane and immunoglobulin-like domains.

Plasma membrane proteins were annotated as receptors and transporters. Transporters were defined by the Uniprot keyword KW-0813. Receptors were defined by the Uniprot keyword KW-0675. The list of receptors was extensively reviewed and new receptors were added based on Uniprot description and bibliography revision. Receptors involved in immune-cell communication were carefully annotated.

Protein lists are available at <https://www.cellphonedb.org/downloads>. Three columns indicate whether the protein has been manually curated: 'tags', 'tags_description', 'tags_reason'.

The tags column is related to the manual curation of a protein, and contains three options: (i) 'N/A', which indicates that the protein has not been manually curated; (ii) 'To_add', which indicates that secreted and/or plasma membrane protein annotation has been added; and (iii) 'To_comment', which indicates that the protein is either secreted (KW-0964) or membrane-associated (KW-1003) but that we manually added a specific property of the protein (that is, the protein is annotated as a receptor).

tags_reason is related to the protein properties, and contains five options: (i) 'extracellular_add', which indicates that the protein is manually annotated as plasma membrane; (ii) 'peripheral_add', which indicates that the protein is manually annotated as a peripheral protein instead of plasma membrane; (iii) 'secreted_add', which indicates that the protein is manually annotated as secreted; (iv) 'secreted_high', which indicates that the protein is manually annotated as secreted highlight. For cytokines, hormones, growth factors and other immune-related proteins; option (v) 'receptor_add' indicates that the protein is manually annotated as a receptor.

tags_description is a brief description of the protein, function or property related to the manually curated protein.

CellPhoneDB annotations of heteromeric receptors and ligands. Heteromeric receptors and ligands (that is, proteins that are complexes of multiple gene products) were annotated by reviewing the literature and Uniprot descriptions. Cytokine complexes, TGF family complexes and integrin complexes were carefully annotated.

If heteromers are defined in the RCSB Protein Data Bank (<http://www.rcsb.org/>), structural information is included in our CellPhoneDB annotation. Heteromeric complex lists are available at www.cellphonedb.org.

CellPhoneDB annotations of interactions. The majority of ligand-receptor interactions were manually curated by reviewing Uniprot descriptions and PubMed information on membrane receptors. Cytokine and chemokine interactions are annotated following the International Union of Pharmacology annotation⁶⁹. Other groups of cell-surface proteins the interactions of which were manually reviewed include the TGF family, integrins, lymphocyte receptors, semaphorins, ephrins, Notch and TNF receptors.

In addition, we considered interacting partners as: (i) binary interactions annotated by IUPHAR (<http://www.guidetopharmacology.org/>) and (ii) cytokines, hormones and growth factors interacting with receptors annotated by the iMEX consortium (<https://www.imexconsortium.org/>)⁷⁰.

We excluded from our analysis transporters and a curated list of proteins including: (i) co-receptors; (ii) nerve-specific receptors such as those related to ear-binding, olfactory receptors, taste receptors and salivary receptors, (iii) small molecule receptors, (iv) immunoglobulin chains, (v) pseudogenes and (vi) viral and retroviral proteins, pseudogenes, cancer antigens and photoreceptors. These proteins are annotated as 'others' in the protein list. We also excluded from our analysis a list of interacting partners not directly involved in cell-cell communication. The 'remove_interactions' list is available in <https://www.cellphonedb.org/downloads>.

Lists of interacting protein chains are available from <https://www.cellphonedb.org/downloads>. The column labelled 'source' indicates the curation source. Manually curated interactions are annotated as 'curated', and the bibliography used to annotate the interaction is stored in 'comments_interaction'. 'Uniprot' indicates that the interaction has been annotated using UniProt descriptions.

Linking Ensembl and Uniprot identification. We assigned to the custom-curated interaction list all the Ensembl gene identifications by matching information from Uniprot and Ensembl by the gene name.

Database structure. Information is stored in a PostgreSQL relational database (www.postgresql.org). SQLAlchemy (www.sqlalchemy.org) and Python 3 were used to build the database structure and the query logic. All the code is open source and uploaded to the webserver.

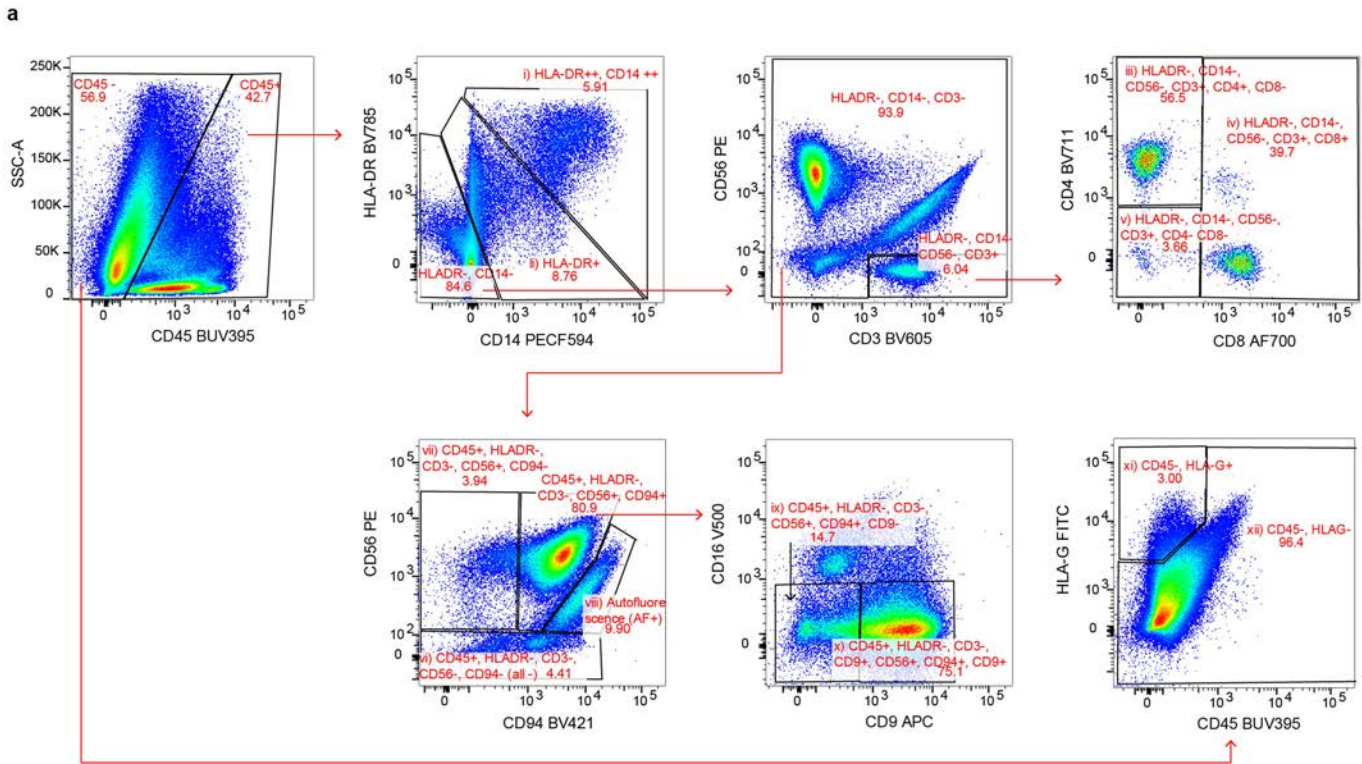
Code availability. CellPhoneDB code is available in <https://github.com/Teichlab/cellphonedb>. The code can also be downloaded from <https://cellphonedb.org/downloads>. KIRid can be downloaded from <https://github.com/Teichlab/KIRid>.

Reporting summary. Further information on research design is available in the Nature Research Reporting Summary linked to this paper.

Data availability

Our expression data for different tissues are also available for user-friendly interactive browsing online at <http://data.teichlab.org> (maternal-fetal interface). The raw sequencing data, expression-count data with cell classifications and the whole-genome sequencing data are deposited at ArrayExpress, with experiment codes E-MTAB-6701 (for droplet-based data), E-MTAB-6678 (for Smart-seq2 data) and E-MTAB-7304 (for the whole-genome sequencing data). Our CellPhoneDB repository is available at www.CellPhoneDB.org.

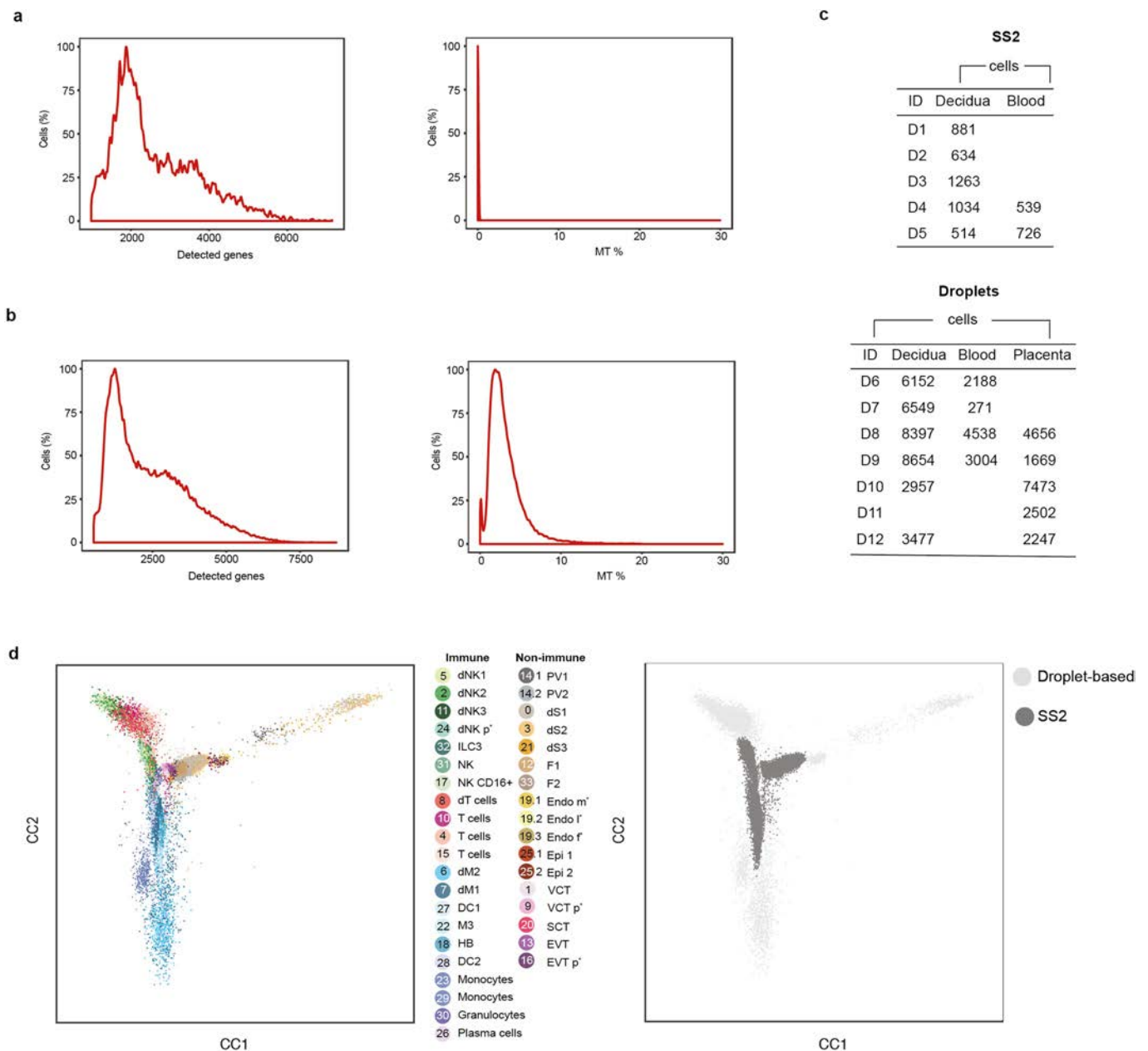
- Gerrelli, D., Lisgo, S., Copp, A. J. & Lindsay, S. Enabling research with human embryonic and fetal tissue resources. *Development* **142**, 3073–3076 (2015).
- O'Rahilla, R. & Muller, F. *Human Embryology and Teratology* (Wiley-Liss, New York, 1992).
- Hern, W. M. Correlation of fetal age and measurements between 10 and 26 weeks of gestation. *Obstet. Gynecol.* **63**, 26–32 (1984).
- Bulmer, J. N., Williams, P. J. & Lash, G. E. Immune cells in the placental bed. *Int. J. Dev. Biol.* **54**, 281–294 (2010).
- Trombetta, J. J. et al. Preparation of single-cell RNA-seq libraries for next generation sequencing. *Curr. Protoc. Mol. Biol.* **107**, 4.22.1–4.22.17 (2014).
- Villani, A.-C. et al. Single-cell RNA-seq reveals new types of human blood dendritic cells, monocytes, and progenitors. *Science* **356**, eaah4573 (2017).
- Kim, D., Langmead, B. & Salzberg, S. L. HISAT: a fast spliced aligner with low memory requirements. *Nat. Methods* **12**, 357–360 (2015).
- Anders, S., Pyl, P. T. & Huber, W. HTSeq—a Python framework to work with high-throughput sequencing data. *Bioinformatics* **31**, 166–169 (2015).
- Satija, R., Farrell, J. A., Gennert, D., Schier, A. F. & Regev, A. Spatial reconstruction of single-cell gene expression data. *Nat. Biotechnol.* **33**, 495–502 (2015).
- Butler, A. & Satija, R. Integrated analysis of single cell transcriptomic data across conditions, technologies, and species. Preprint at <https://www.biorxiv.org/content/early/2017/07/18/164889> (2017).
- van den Brink, S. C. et al. Single-cell sequencing reveals dissociation-induced gene expression in tissue subpopulations. *Nat. Methods* **14**, 935–936 (2017).
- Qiu, X. et al. Reversed graph embedding resolves complex single-cell trajectories. *Nat. Methods* **14**, 979–982 (2017).
- Hiby, S. E. et al. Combinations of maternal KIR and fetal HLA-C genes influence the risk of preeclampsia and reproductive success. *J. Exp. Med.* **200**, 957–965 (2004).
- Robinson, J. et al. The IPD and IMGT/HLA database: allele variant databases. *Nucleic Acids Res.* **43**, D423–D431 (2015).
- Kang, H. M. et al. Multiplexed droplet single-cell RNA-sequencing using natural genetic variation. *Nat. Biotechnol.* **36**, 89–94 (2018).
- Stubbington, M. J. T. et al. T cell fate and clonality inference from single-cell transcriptomes. *Nat. Methods* **13**, 329–332 (2016).
- Li, H. Aligning sequence reads, clone sequences and assembly contigs with BWA-MEM. Preprint at <https://arxiv.org/abs/1303.3997> (2013).
- Li, H. et al. The Sequence Alignment/Map format and SAMtools. *Bioinformatics* **25**, 2078–2079 (2009).
- Mills, R. E. et al. Natural genetic variation caused by small insertions and deletions in the human genome. *Genome Res.* **21**, 830–839 (2011).
- 1000 Genomes Project Consortium. A map of human genome variation from population-scale sequencing. *Nature* **467**, 1061–1073 (2010).
- Van der Auwera, G. A. et al. From FastQ data to high confidence variant calls: the Genome Analysis Toolkit best practices pipeline. *Curr. Protoc. Bioinformatics* **43**, 11.10.1–11.10.33 (2013).
- Broad Institute. *Picard tools* <https://broadinstitute.github.io/picard/> (Broad Institute, 2018).
- Li, H. A statistical framework for SNP calling, mutation discovery, association mapping and population genetical parameter estimation from sequencing data. *Bioinformatics* **27**, 2987–2993 (2011).
- Robinson, J., Mistry, K., McWilliam, H., Lopez, R. & Marsh, S. G. E. IPD—the Immuno Polymorphism Database. *Nucleic Acids Res.* **38**, D863–D869 (2010).
- Bray, N. L., Pimentel, H., Melsted, P. & Pachter, L. Near-optimal probabilistic RNA-seq quantification. *Nat. Biotechnol.* **34**, 525–527 (2016).
- Turro, E. et al. Haplotype and isoform specific expression estimation using multi-mapping RNA-seq reads. *Genome Biol.* **12**, R13 (2011).
- Bachelier, F. et al. International Union of Basic and Clinical Pharmacology. LXXXIX. Update on the extended family of chemokine receptors and introducing a new nomenclature for atypical chemokine receptors. *Pharmacol. Rev.* **66**, 1–79 (2013).
- Orchard, S. et al. Protein interaction data curation: the International Molecular Exchange (iMEX) consortium. *Nat. Methods* **9**, 345–350 (2012).



Extended Data Fig. 1 | Gating strategy for Smart-seq2 data.

a, Gating strategy for a panel of 14 antibodies to analyse immune cells in decidual samples by Smart-seq2 (CD3, CD4, CD8, CD9, CD14, CD16, CD19, CD20, CD34, CD45, CD56, CD94, DAPI, HLA-DR and HLA-G). Cells isolated for Smart-seq2 data were gated on live; CD19- and CD20-negative, singlets and the following cell types were sorted: (i) CD45⁺CD14^{high}HLA-DR^{high}; (ii) CD45⁺HLA-DR⁺; (iii) CD45⁺HLA-DR⁻CD56⁻CD3⁺CD4⁺CD8⁻; (iv) CD45⁺HLA-DR⁻CD56⁻CD3⁺CD8⁺; (v) CD45⁺HLA-DR⁻CD56⁻CD3⁺CD4⁻CD8⁻; (vi) CD45⁺HLA-DR⁻

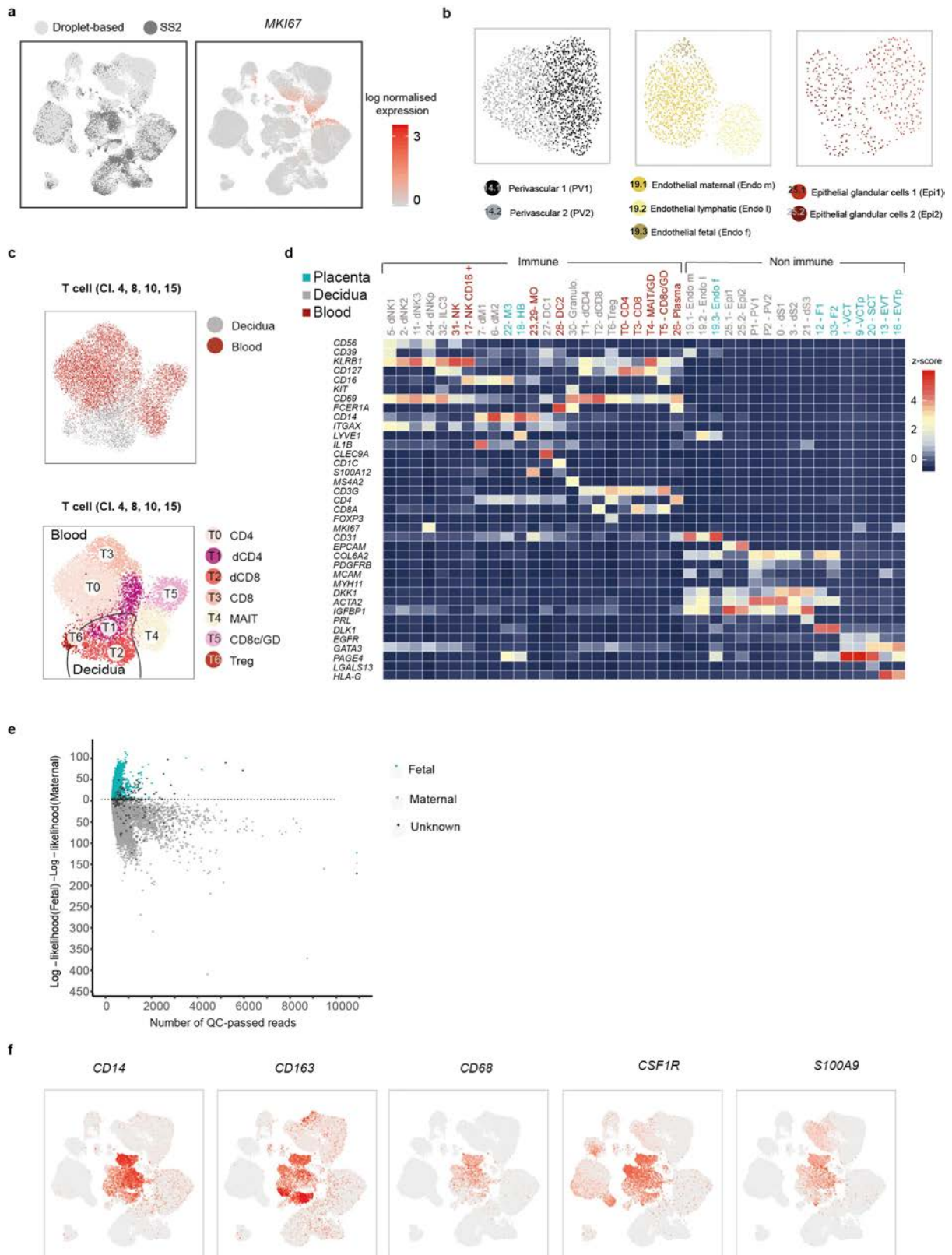
CD3⁻CD56⁻CD94⁻ (labelled 'all -' on the figure); (vii) CD45⁺HLA-DR⁻CD3⁻CD56⁺CD94⁻; (viii) autofluorescence; (ix) CD45⁺HLA-DR⁻CD3⁻CD56⁺CD94⁺CD9⁻; (x) CD45⁺HLA-DR⁻CD3⁻CD56⁺CD94⁺CD9⁺; (xi) CD45⁻HLA-G⁺; (xii) CD45⁻HLA-G⁻. Sample F9 is shown as an example. Cells from different gates were sorted in different plates: myeloid cells (gates (i) and (ii)); T cells (gates (iii), (iv) and (v)); natural killer cells (gates (vi), (vii), (viii), (ix) and (x)); CD45⁻ (gates (xi) and (xii)). Antibody information is provided in Supplementary Table 10.



* p =proliferative; m = maternal; l = lymphatic; f = fetal

Extended Data Fig. 2 | Quality control of droplet and Smart-seq2 datasets. **a**, Histograms show the distribution of the cells from the Smart-seq2 dataset ordered by number of detected genes and mitochondrial gene expression content. **b**, Histograms show the distribution of the cells from the droplet-based dataset ordered by number of detected genes and mitochondrial gene expression content. **c**, Total numbers of cells that passed the quality control, processed by Smart-seq2 and droplet scRNA-

seq. Each row is a separate donor. **d**, Canonical correlation vectors (CC1 and CC2) of integrated analysis of decidual and placental cells from the Smart-seq2 ($n = 5$ deciduas, $n = 2$ peripheral blood samples) and droplet-based datasets ($n = 5$ placentas, $n = 6$ deciduas and $n = 4$ blood samples), coloured on the basis of their assignment to clusters and the technology that was used for scRNA-seq.

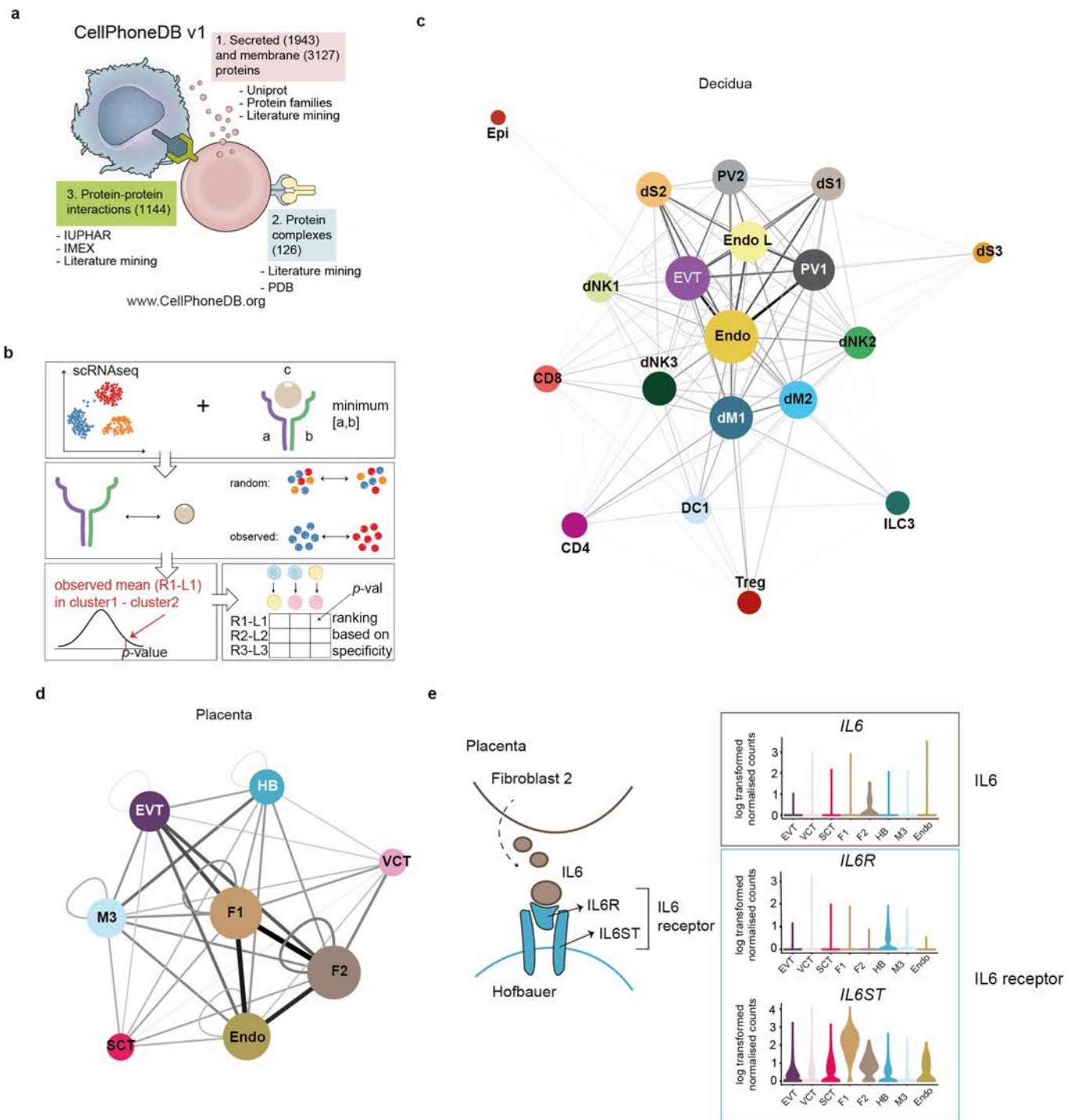


Extended Data Fig. 3 | See next page for caption.

Extended Data Fig. 3 | Overview of droplet and Smart-seq2 datasets.

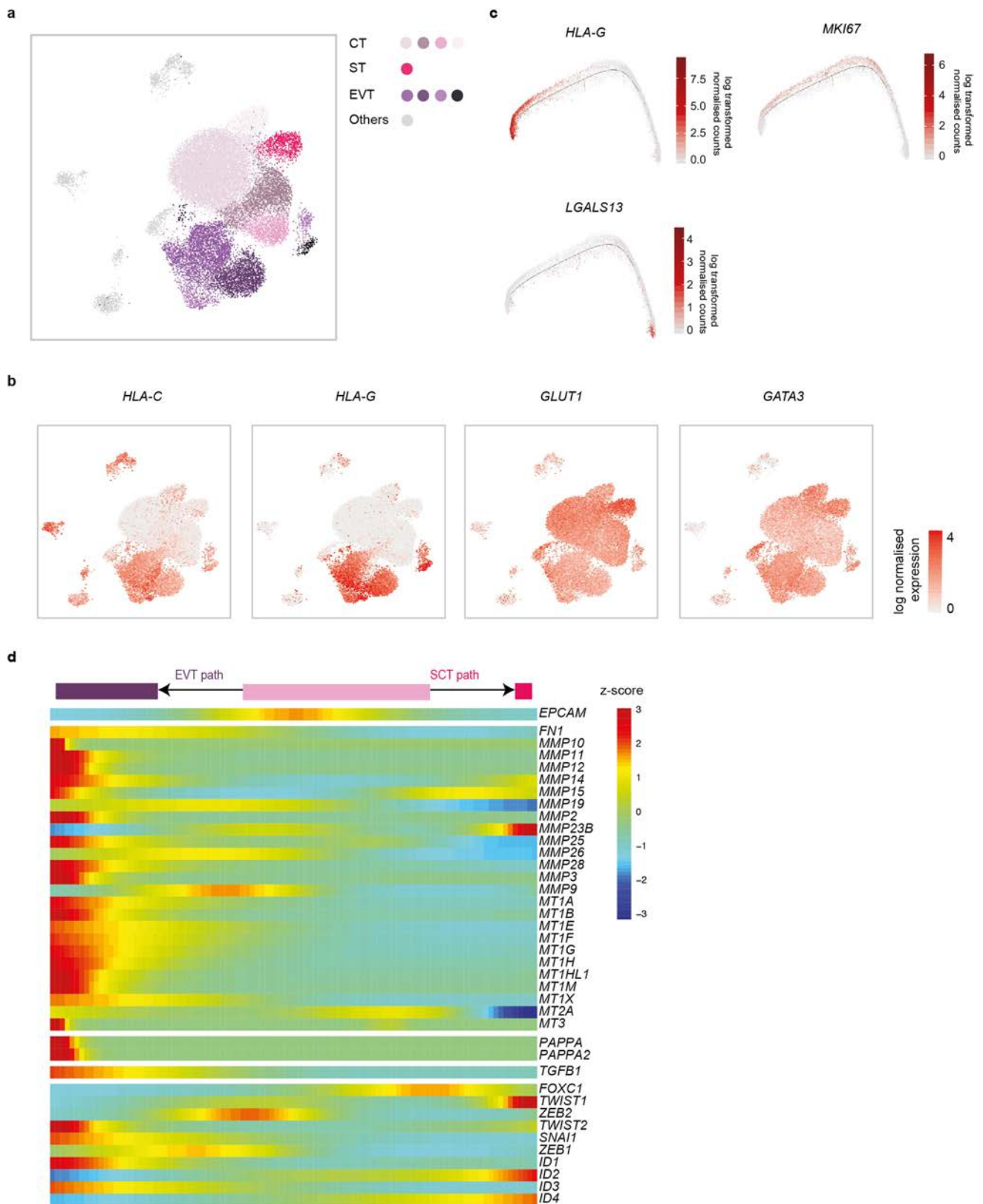
a, UMAP plot showing the integration of the Smart-seq2 and droplet-based dataset and the log-transformed expression of *MKI67* (which marks proliferating cells). **b**, UMAP plots showing the separate and more-detailed integration analysis of the cells from cluster 14 (perivascular cells), cluster 19 (endothelial cells) and cluster 25 (epithelial cells). Clusters are labelled as in Fig. 1c. **c**, UMAP visualization of T cell clusters obtained by integrating Smart-seq2 and droplet-based T cells subpopulations (clusters 4, 8, 10 and 15) from Fig. 1c. Cells are coloured by the tissue of origin (top) and the identified clusters (bottom). **d**, Heat map showing the *z*-score of the mean log-transformed, normalized counts for each cluster of selected marker genes used to annotate clusters. For a more extensive

set of genes, see Supplementary Table 2. Adjusted *P* value < 0.1; Wilcoxon rank-sum test with Bonferroni correction. NK, natural killer cells; NKp, proliferating natural killer cells; MO, monocytes; Granulo, granulocytes; T_{reg}, regulatory T cells; GD, $\gamma\delta$ T cells; CD8c, cytotoxic CD8⁺ T cells; Plasma, plasma cells. **e**, log-likelihood differences between assignment to fetal versus assignment to maternal origin of cells, on the basis of single nucleotide polymorphism calling from the droplet RNA-seq data. Cells are coloured by their assignment as determined by demuxlet. For this figure, we used *n* = 5 placentas, *n* = 6 deciduas and *n* = 4 blood individuals. **f**, UMAP visualization of the log-transformed, normalized expression of selected marker genes of the M3 subpopulation.



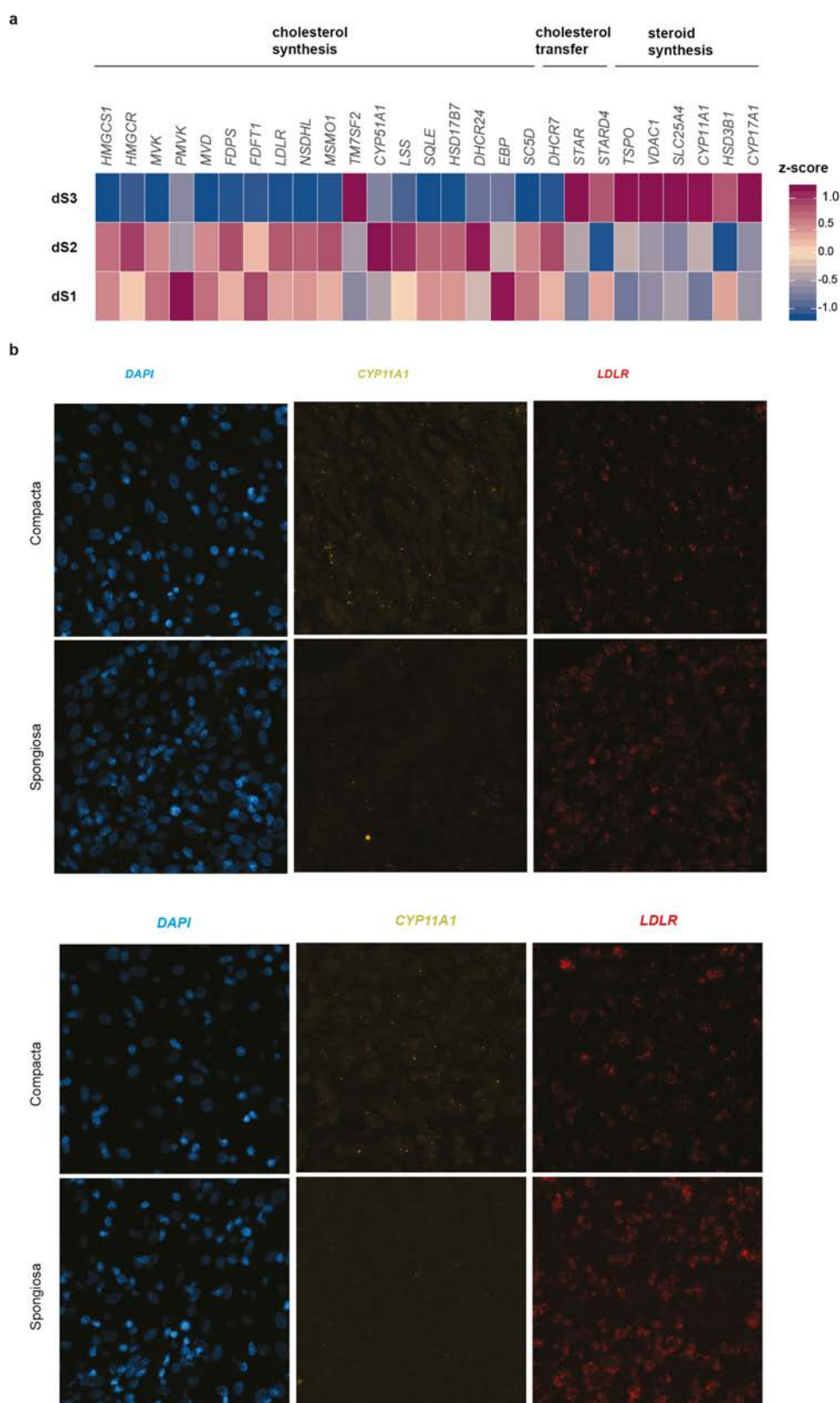
Extended Data Fig. 4 | Cell-cell communication networks in the maternal-fetal interface using CellPhoneDB. **a**, Information aggregated within www.CellPhoneDB.org. **b**, Statistical framework used to infer ligand-receptor complex specific to two cell types from single-cell transcriptomics data. Predicted *P* values for a ligand-receptor complex across two cell clusters are calculated using permutations, in which cells are randomly re-assigned to clusters (see Methods) **c**, Networks visualizing potential specific interactions in the decidua, in which nodes are clusters (cell types) and edges represent the number of significant ligand-receptor pairs. The network was created for edges with more than 30 interactions and the network layout was set to force-directed layout. Only droplet

data were considered for the CellPhoneDB analysis ($n = 6$ deciduas). **d**, Networks visualizing potential specific interactions in the placenta, in which nodes are clusters and edges represent the number of significant ligand-receptor pairs. The network layout was set to force-directed layout. Only droplet data were considered for the analysis ($n = 5$ placentas). **e**, An example of significant interactions identified by CellPhoneDB. Violin plots show log-transformed, normalized expression levels of the components of the IL6-IL6R complex in placental cells. IL6 expression is enriched in the fibroblast 2 cluster (F2; dark brown in **d**) and the two subunits of the IL6 receptors (IL6R and IL6ST) are co-expressed in Hofbauer cells.



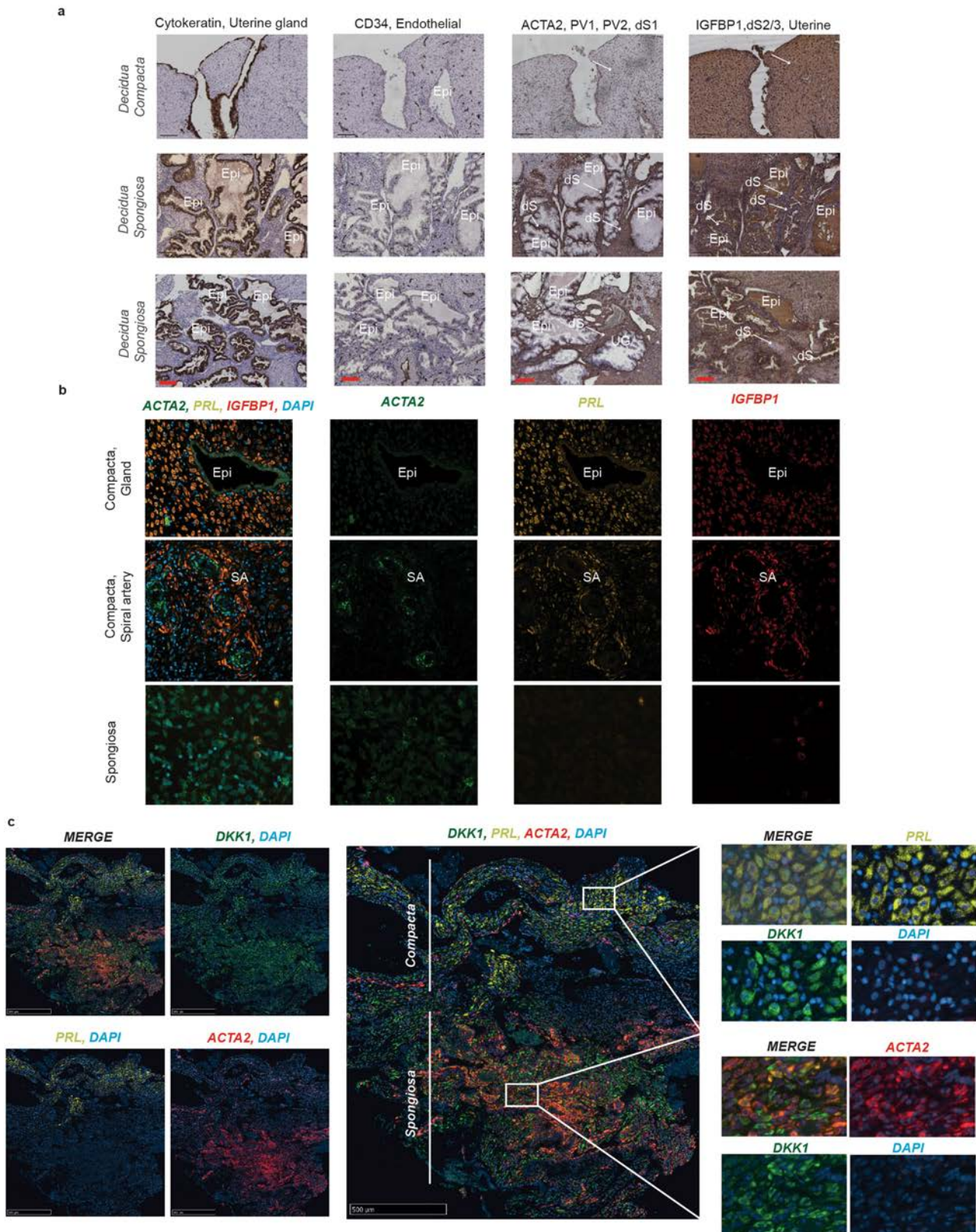
Extended Data Fig. 5 | Trophoblast analysis. **a**, UMAP visualization of the integrated analysis of the trophoblast subpopulations that were used for pseudotime analysis, including the enriched *EPCAM*⁺ and *HLA-G*⁺ cells (see Methods). Cells that were excluded from the pseudotime analysis are coloured in grey ($n = 5$ placentas, $n = 11$ deciduas). **b**, UMAP visualization of the log-transformed, normalized expression of selected

canonical trophoblast marker genes ($n = 5$ placentas). **c**, Visualization of log-transformed, normalized expression of *HLA-G*, *MKI67* and *LGALS13* across trophoblast differentiation. **d**, Heat map showing genes that are involved in the epithelial–mesenchymal transition, identified as varying significantly as EVT differentiate (q value < 0.1 , likelihood ratio test, P values were adjusted for the false discovery rate).



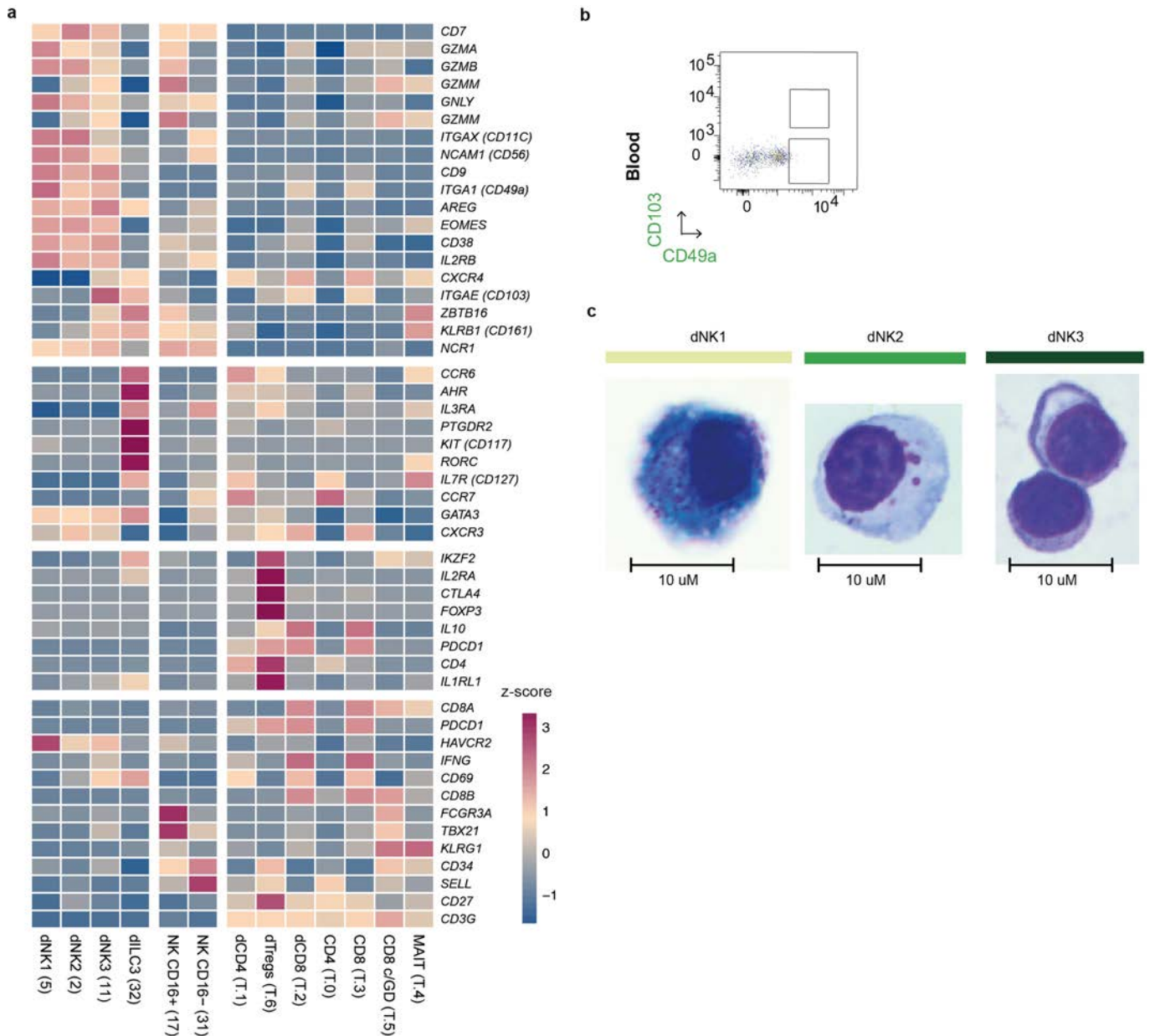
Extended Data Fig. 6 | Steroid synthesis. a, Heat map showing relative expression of enzymes involved in cholesterol and steroid synthesis in the three stromal subsets ($n = 11$ deciduas). **b,** Multiplexed smFISH in two decidua parietalis sections from two different individuals, showing

an enrichment of CYP11A1 expression in the decidua compacta. Section stained by CYP11A1, LDLR and DAPI. Images are shown at $40\times$ magnification. A high resolution is needed to detect differences between the sections ($n = 2$ individuals).



Extended Data Fig. 7 | In situ staining for the different stromal cells.
a, Immunohistochemistry of decidual serial sections stained for cytokeratin (uterine glands), CD34 (endothelial cells), ACTA2 (perivascular populations and dS1) and IGFBP1 (stromal cells and glandular secretions) ($n = 2$ biological replicates). ACTA2⁺ stromal cells are confined to the stromal cells of the deeper decidua spongiosa, whereas stromal cells in the decidua compacta are ACTA2⁻. IGFBP1⁺ stromal cells are enriched in the decidua compacta, whereas stromal cells around the glands in the decidua spongiosa are IGFBP1⁻. Glandular secretions are

IGFBP1⁺. **b**, Multiplexed smFISH for a decidua parietalis section showing the two decidual layers. ACTA2, dS1 population confined to decidua spongiosa; IGFBP1 and PRL, dS2 and dS3 populations confined to decidua compacta. Samples shown are from a different individual than samples shown in Fig. 4d ($n = 2$ biological replicates). **c**, Multiplexed smFISH for a decidua parietalis section showing the two decidual layers. DKK1, decidual stromal marker; ACTA2, dS1 population confined to decidua spongiosa; PRL, dS3 population confined to decidua compacta ($n = 1$ biological replicate).

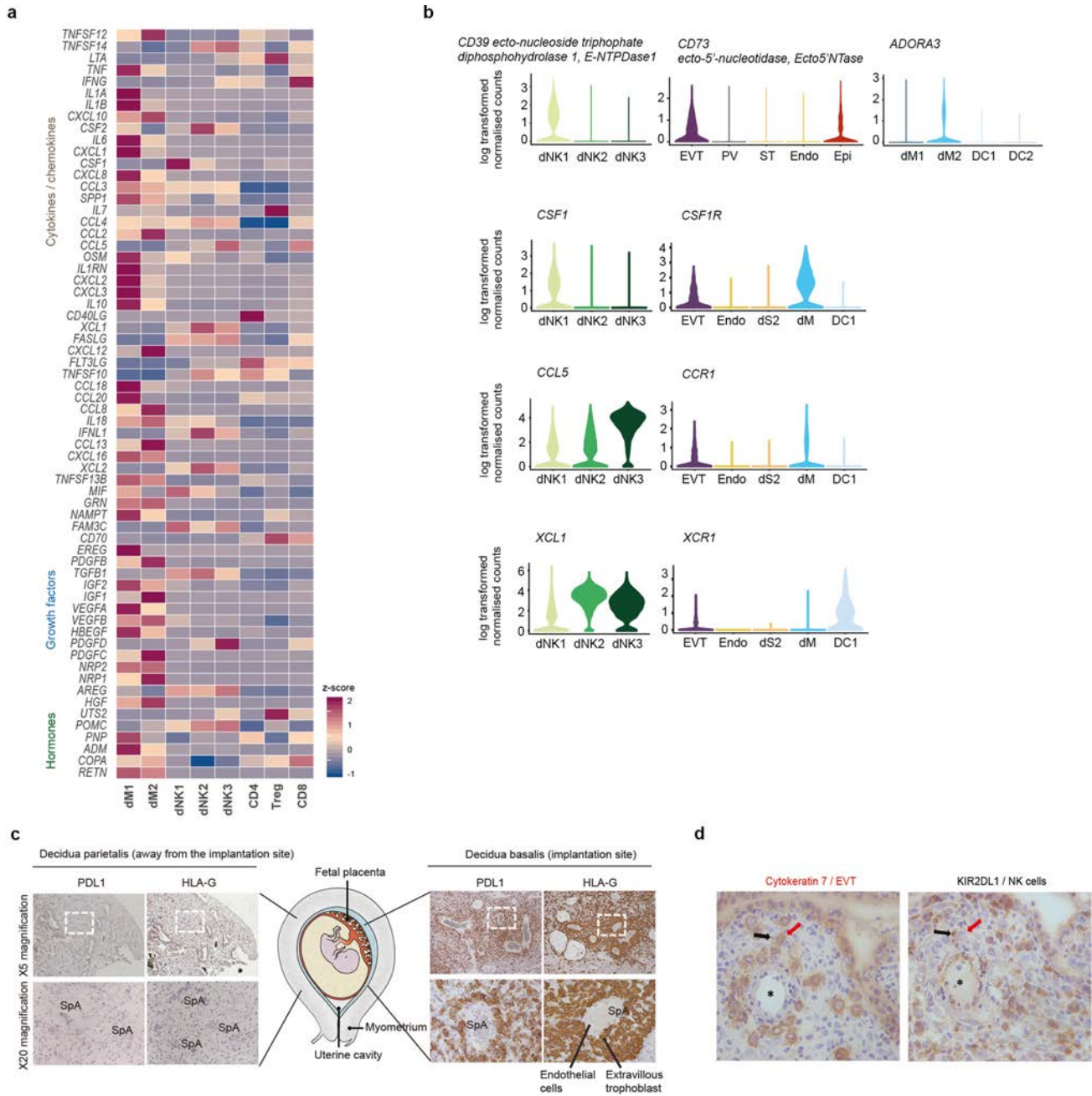


Extended Data Fig. 8 | Lymphocyte populations in the decidua.

a, Heat map showing z-scores of the mean log-transformed, normalized expression of selected genes in the lymphocyte populations. Proliferating dNK cells (dNKp) are excluded from the analysis ($n = 11$ deciduas).

b, FACS gating strategy in Fig. 5 applied in matched blood. Matched blood

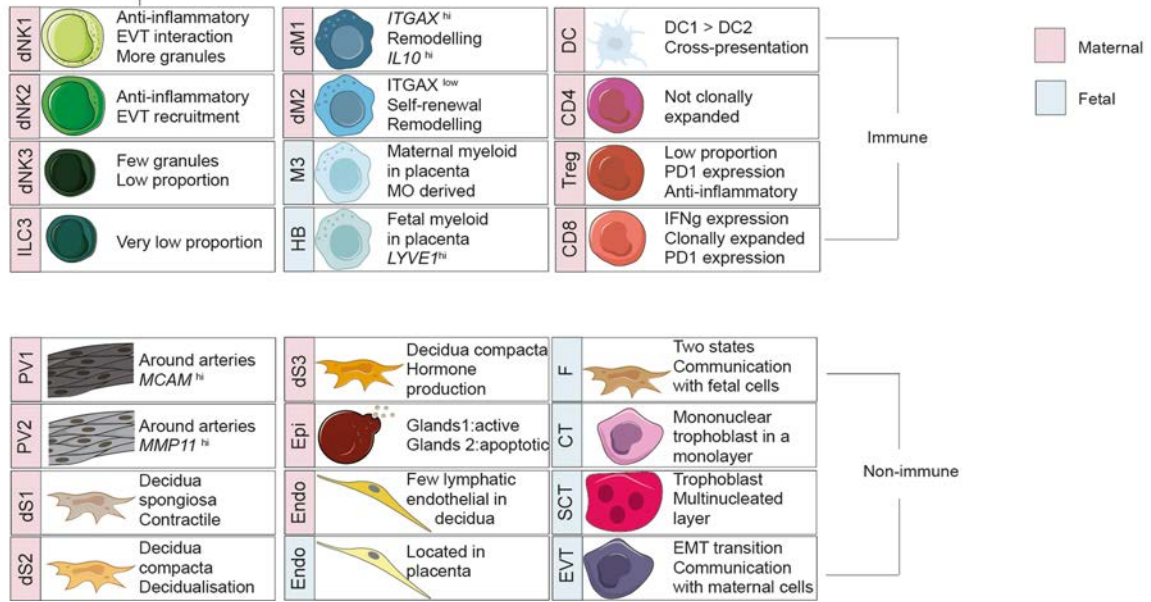
for the sample shown in Fig. 5 ($n = 2$ biological replicates). **c**, Morphology of dNK1, dNK2 and dNK3 subsets by Giemsa-Wright stain after cytopspin (representative data from 1 of $n = 2$ biological replicates are shown). Scale bar, 10 μm .



Extended Data Fig. 9 | Expression of ligands and receptors at the maternal–fetal interface. a, Heat map showing z-scores of the mean log-transformed, normalized expression of genes annotated as cytokines, growth factors, hormones and angiogenic factors with a log-mean > 0.1 in the selected decidual immune populations ($n = 11$ deciduas). **b**, Violin plots showing log-transformed, normalized expression levels of selected ligands expressed in the three dNK cells and their corresponding receptors expressed on other decidual cells and EVT (*CD39*, *CD73*, *ADORA3*, *CSF1*, *CSF1R*, *CCL5*, *CCR1*, *XCL1* and *XCR1*; $n = 11$ deciduas, $n = 5$ placentas). **c**, Immunohistochemistry images of serial decidual sections stained for the EVT marker HLA-G and the inhibitory ligand PDL1. Bottom panels

shown the areas in white boxes in the top panels at higher power. HLA-G⁺ cells are only present at the site of placentation (decidua basalis) and are absent elsewhere (decidua parietalis). SpA, spiral arteries. The EVT is strongly PDL1⁺. We show representative data from one individual of $n = 5$ biological replicates. **d**, Immunohistochemistry images of decidual serial sections of the decidual implantation site (at 10 weeks of gestation), stained for the trophoblast cell marker, cytokeratin-7 (red arrow) and the inhibitory receptor KIR2DL1 on a natural killer cell (black arrow). The asterisk marks the lumen of a spiral artery that supplies the conceptus. We show representative data from one individual of $n = 5$ samples).

a



Extended Data Fig. 10 | Encyclopaedia of cells at the maternal–fetal interface. a, Summary of populations from our scRNA-seq data. Blue, fetal; red, maternal.

Reporting Summary

Nature Research wishes to improve the reproducibility of the work that we publish. This form provides structure for consistency and transparency in reporting. For further information on Nature Research policies, see [Authors & Referees](#) and the [Editorial Policy Checklist](#).

Statistical parameters

When statistical analyses are reported, confirm that the following items are present in the relevant location (e.g. figure legend, table legend, main text, or Methods section).

n/a Confirmed

- The exact sample size (n) for each experimental group/condition, given as a discrete number and unit of measurement
- An indication of whether measurements were taken from distinct samples or whether the same sample was measured repeatedly
- The statistical test(s) used AND whether they are one- or two-sided
Only common tests should be described solely by name; describe more complex techniques in the Methods section.
- A description of all covariates tested
- A description of any assumptions or corrections, such as tests of normality and adjustment for multiple comparisons
- A full description of the statistics including central tendency (e.g. means) or other basic estimates (e.g. regression coefficient) AND variation (e.g. standard deviation) or associated estimates of uncertainty (e.g. confidence intervals)
- For null hypothesis testing, the test statistic (e.g. F , t , r) with confidence intervals, effect sizes, degrees of freedom and P value noted
Give P values as exact values whenever suitable.
- For Bayesian analysis, information on the choice of priors and Markov chain Monte Carlo settings
- For hierarchical and complex designs, identification of the appropriate level for tests and full reporting of outcomes
- Estimates of effect sizes (e.g. Cohen's d , Pearson's r), indicating how they were calculated
- Clearly defined error bars
State explicitly what error bars represent (e.g. SD, SE, CI)

Our web collection on [statistics for biologists](#) may be useful.

Software and code

Policy information about [availability of computer code](#)

Data collection

Software used include: R, Python 3, SQLAlchemy, PostgreSQL, HISAT2, 10X Genomics' Cell Ranger, Seurat, Monocle 2, Cytoscape, Demuxlet, HTSeq-count, Samtools, GATK, BWA, Picard, bcftools, TraCeR, Kallisto, MMSEQ, BD FACS DIVA software, Axiovision and ZEN software (zeiss), Graphpad, Photoshop, Illustrator. Detailed parameters of each of the methods are mentioned in relevant sections in Methods.

Data analysis

Software used include: R, Python 3, SQLAlchemy, PostgreSQL, HISAT2, 10X Genomics' Cell Ranger, Seurat, Monocle 2, Cytoscape, Demuxlet, HTSeq-count, Samtools, GATK, BWA, Picard, bcftools, TraCeR, Kallisto, MMSEQ, Graphpad, Axiovision and ZEN software (zeiss), FlowJo, Photoshop, Illustrator. Detailed parameters of each of the methods are mentioned in relevant sections in Methods.

For manuscripts utilizing custom algorithms or software that are central to the research but not yet described in published literature, software must be made available to editors/reviewers upon request. We strongly encourage code deposition in a community repository (e.g. GitHub). See the Nature Research [guidelines for submitting code & software](#) for further information.

Data

Policy information about [availability of data](#)

All manuscripts must include a [data availability statement](#). This statement should provide the following information, where applicable:

- Accession codes, unique identifiers, or web links for publicly available datasets
- A list of figures that have associated raw data
- A description of any restrictions on data availability

Data is uploaded to ArrayExpress:

Experiment: E-MTAB-6701, E-MTAB-6678, E-MTAB-7304

Field-specific reporting

Please select the best fit for your research. If you are not sure, read the appropriate sections before making your selection.

Life sciences Behavioural & social sciences Ecological, evolutionary & environmental sciences

For a reference copy of the document with all sections, see [nature.com/authors/policies/ReportingSummary-flat.pdf](https://www.nature.com/authors/policies/ReportingSummary-flat.pdf)

Life sciences study design

All studies must disclose on these points even when the disclosure is negative.

Sample size	No statistical methods were used to predetermine sample size. We followed standards in the field and Human Cell Atlas criteria.
Data exclusions	No exclusion was applied to the uploaded raw data in ArrayExpress. For the final count matrix, we excluded cells based on pre-established criteria for single-cells: we excluded low quality samples and contaminating cells (i.e. - cells with low number of detected genes and high mitochondria content) - exclusion criteria for each case are comprehensively detailed in the relevant Methods section.
Replication	We did scRNAseq and flow cytometry analysis on 11 deciduas, 5 placentas and 6 matched peripheral blood from 6-14 gestational weeks. Additional samples were used for the validation experiments: (a) Immunohistochemistry: staining of perivascular populations was performed in two independent individuals (Fig. 3b); ACTA2 staining of decidual stromal cells was performed in three independent individuals (Fig. 3c; Extended Data Figure 7a), staining of PDL1 was performed in five independent individuals (Extended Data Figure 9c); (b) smFISH: staining of stromal populations was performed in two independent individuals (Fig. 3d, Extended Data Figure 6b, Extended Data Figure 7b), staining of stromal population in Extended Data Figure 7c was performed in one individual; (c) Flow cytometry: flow cytometry for Figure 4d was performed in 6 of the deciduas sequenced and dNK for two of them were isolated and stained with Giemsa-Wright stain after cytopsin 8c; seven to ten independent individuals were additionally used for flow cytometry analysis on Figure 4f. Any replication experiment was excluded.
Randomization	Only healthy individuals were considered in our analysis. Therefore, any further randomization protocol was required.
Blinding	Only healthy individuals were considered in our analysis. Therefore, no blinding was performed

Reporting for specific materials, systems and methods

Materials & experimental systems

n/a	Involvement in the study
<input checked="" type="checkbox"/>	<input type="checkbox"/> Unique biological materials
<input type="checkbox"/>	<input checked="" type="checkbox"/> Antibodies
<input checked="" type="checkbox"/>	<input type="checkbox"/> Eukaryotic cell lines
<input checked="" type="checkbox"/>	<input type="checkbox"/> Palaeontology
<input checked="" type="checkbox"/>	<input type="checkbox"/> Animals and other organisms
<input type="checkbox"/>	<input checked="" type="checkbox"/> Human research participants

Methods

n/a	Involvement in the study
<input checked="" type="checkbox"/>	<input type="checkbox"/> ChIP-seq
<input type="checkbox"/>	<input checked="" type="checkbox"/> Flow cytometry
<input checked="" type="checkbox"/>	<input type="checkbox"/> MRI-based neuroimaging

Antibodies

Antibodies used

Antibody Company Catalog number Clone Use Dilution (Supplementary table 10)
 CD45-BUV395 BD Bioscience 563791 Clone HI30 (RUO) Flow cytometry - index data; Fig. 5d 2.5ul:100ul
 CD94-BV421 BD Bioscience 743948 HP-3D9 (RUO) Flow cytometry - index data 2.5ul:100ul

CD16-BV500 BD Bioscience 561394 3GH Flow cytometry - index data; Fig. 5d 2.5ul:100ul
 CD3-BV605 Biolegend 344836 SK7 Flow cytometry - index data; Fig. 5d 2.5ul:100ul
 CD4-BV711 Biolegend 300558 RPA-T4 Flow cytometry - index data 2.5ul:100ul
 HLA-DR BV786 Biolegend 307642 L243 Flow cytometry - index data 2.5ul:100ul
 HLA-G FITC BioRad MCA2044 MEM-G/9 Flow cytometry - index data 2.5ul:100ul
 CD56-PE Miltenyi 130-100-622 REA196 Flow cytometry - index data; Fig 5d 2.5ul:100ul
 CD14-PECF594 BD Bioscience 562334 PE-CF594 Flow cytometry - index data 2.5ul:100ul
 CD9-APC BD Bioscience 341638 M-L13 Flow cytometry - index data 2.5ul:100ul
 CD8-AF700 Biolegend 300920 HIT8a Flow cytometry - index data 2.5ul:100ul
 CD19-APCCy7 BioLegend 302217 HIB19 Flow cytometry - index data 2.5ul:100ul
 CD20-APCCy7 BioLegend 302313 2H7 Flow cytometry - index data 2.5ul:100ul
 Cytokeratin 7 Dako MA5-11986 OV-TL 12/30 Immunocytochemistry Dilution:1:200; antigen retrieval buffer:Citrate
 PD-L1 Cell Signaling Technology 13684 E13LN Immunocytochemistry Dilution:1:400; antigen retrieval buffer:TRIS/EDTA
 HLA-G Biorad MCA2043 MEM-G1 Immunocytochemistry Dilution:1:25; antigen retrieval buffer:Citrate
 CD146 / MCAM Abcam ab75769 EPR3208 Immunocytochemistry Dilution:1:2500; antigen retrieval buffer:Citrate
 Smooth Muscle Actin Dako M0851 1A4 Immunocytochemistry Dilution:1:100 antigen retrieval buffer:TRIS/EDTA
 NKG2A - Viobright Miltenyi 130-105-646 REA110 Flow cytometry - Fig 5f Dilution: 1:100 in cocktail
 KIR2DL2/3/S2 - PE-Cy5.5 Beckman Coulter A66900 GL183 Flow cytometry - Fig 5f Dilution: 1:50 in cocktail
 KIR2DS4 - APC Miltenyi 130-114-773 REA860 Flow cytometry - Fig 5f Dilution: 1:50 in cocktail
 GzmB - AF700 BD Biosciences 560213 GB11 Flow cytometry - Fig 5f Dilution: 1:100 in intracellular cocktail
 KIR2DL1 - APC-Vio770 Miltenyi 130-103-937 REA284 Flow cytometry - Fig 5f Dilution: 1:25 in cocktail
 Perforin - BV421 Biolegend 308122 DG9 Flow cytometry - Fig 5f Dilution: 1:100 in intracellular cocktail
 CD3 - BV510 BioLegend 317332 OKT3 Flow cytometry - Fig 5f Dilution: 1:100 in cocktail
 CD14 - BV510 BioLegend 301842 M5E2 Flow cytometry - Fig 5f Dilution: 1:100 in cocktail
 CD19 - BV510 BioLegend 302242 HIB19 Flow cytometry - Fig 5f Dilution: 1:100 in cocktail
 LIVE/DEAD™ Fixable Aqua Dead Cell Stain Kit ThermoFisher L34957 N/A Flow cytometry - Fig 5f Dilution: 1:100 in secondary cocktail (from 200ul dilution of stock powder)
 KIR2DL3 biotin - biotin Miltenyi 130-100-126 REA147 Flow cytometry - Fig 5f Dilution: 1:100 in cocktail
 streptavidin Qdot605 (detection of KIR2DL3)- Q605 ThermoFisher Q10103MP N/A Flow cytometry - Fig 5f Dilution: 1:250 in secondary cocktail
 Granulysin - PE Biolegend 348003 DH2 Flow cytometry - Fig 5f Dilution: 1:200 in intracellular cocktail
 CD56-PE-Dazzle BioLegend 318348 HCD56 Flow cytometry - Fig 5f Dilution: 1:200 in intracellular cocktail
 GzmA - PE-Cy7 ebioscience/Thermo Fischer 25-9177-42 CB9 Flow cytometry - Fig 5f Dilution: 1:100 in intracellular cocktail
 CD49a-BV421 Bd Bioscience 742357 SR84 (RUO) Flow cytometry - Fig 5d 2.5ul:100ul
 CD14- BV605 Bd Bioscience 564054 M5E2 (RUO) Flow cytometry - Fig 5d 2.5ul:100ul
 CD19-BV605 Bd Bioscience 740394 HIB19 (RUO) Flow cytometry - Fig 5d 2.5ul:100ul
 CD20-BV605 Bd Bioscience 747736 2H7 (RUO) Flow cytometry - Fig 5d 2.5ul:100ul
 CD103-PerCP-Cy5.5 Biolegend 350225 Ber-ACT8 Flow cytometry - Fig 5d 2.5ul:100ul
 KIR2DL1 - PeVio770 MACS - Miltenyi Biotec 130-103-936 REA284 Flow cytometry - Fig 5d 2.5ul:100ul
 CD18 (ITGB2) - APC BioLegend 366307 CBR LFA-1/2 Flow cytometry - Fig 5d 2.5ul:100ul
 CD39 - APC Cy7 BioLegend 328225 A1 Flow cytometry - Fig 5d 2.5ul:100ul

Validation

Antibody Validation (Supplementary table 10)
 CD45-BUV395 Flow cytometry (Routinely Tested) . Flow cytometric analysis of CD45 expression on human peripheral blood lymphocytes (website).
 CD94-BV421 Flow cytometry (Qualified) (website)
 CD16-BV500 Flow cytometry (Routinely Tested). Flow cytometric analysis of CD16 expression on human peripheral blood lymphocytes. (Website)
 CD3-BV605 Flow cytometry. Human peripheral blood lymphocytes were stained with CD3 (clone SK7) Brilliant Violet 605™ (website)
 CD4-BV711 Flow cytometry. Human peripheral blood lymphocytes were stained with CD4 (clone RPA-T4) Brilliant Violet 711™ (filled histogram) (website)
 HLA-DR BV786 Flow cytometry. Human peripheral blood lymphocytes were stained with HLA-DR (clone L243) Brilliant Violet 785™. (website)
 HLA-G FITC Evaluation of HLA-G expression on transfected cells by flow cytometry (website)
 CD56-PE REAfinity clone is tested against different known clones, in a blocking experiment, to identify whether they recognize completely overlapping (++), partially overlapping (+), or completely different epitopes (-). In a blocking experiment, cells are incubated with an excess of purified unconjugated REAfinity clone followed by staining with conjugated form of the other known clones (website).
 CD14-PECF594 Flow cytometry (Routinely Tested). Flow cytometric analysis of CD14 expression on human peripheral blood monocytes (webpage)
 CD9-APC Flow cytometry (Routinely Tested) (website). ImmunogenHuman C-ALL Cells.
 CD8-AF700 quality control tested by immunofluorescent staining with flow cytometric analysis (website)
 CD19-APCCy7 quality tested by flow cytometry (website)
 CD20-APCCy7 quality tested by flow cytometry (website)
 Cytokeratin 7 Tested in Immunocytochemistry (ICC), Immunofluorescence (IF), Immunohistochemistry (Paraffin) (IHC (P)) and Western Blot (WB)
 PD-L1 Tested in Western Blotting, Immunoprecipitation, IHC-Leica® Bond™, Immunohistochemistry (Paraffin), Flow Cytometry (website)
 HLA-G Tested in Immunohistochemistry (Paraffin), Western Blotting (website)
 CD146 / MCAM Tested in immunofluorescence, immunohistochemistry, Western Blotting, Flow Cytometry (website)
 Smooth Muscle Actin Tested in Western Blotting, Immunofluorescence, ELISA, Immunohistochemistry (website)
 NKG2A - Viobright Flow cytometry. Human peripheral blood and decidual NK cells used for titration.
 KIR2DL2/3/S2 - PE-Cy5.5 Tested by FACS of cell line transfected with gene target
 KIR2DS4 - APC Flow cytometry. Human peripheral blood and decidual NK cells used for titration.

GzmB - AF700 Flow cytometry. Human peripheral blood and decidual NK cells used for titration.
 KIR2DL1 - APC-Vio770 Tested by FACS of cell line transfected with gene target
 Perforin - BV421 Flow cytometry. Human peripheral blood and decidual NK cells used for titration.
 CD3 - BV510 Flow cytometry. Human peripheral blood lymphocytes used for titration.
 CD14 - BV510 Flow cytometry. Human peripheral blood lymphocytes used for titration.
 CD19 - BV510 Flow cytometry. Human peripheral blood lymphocytes used for titration.
 Amine reactive dye Flow cytometry. Human peripheral blood lymphocytes used for titration of each batch since diluted aliquotes are stored frozen.
 KIR2DL3 biotin - biotin REAfinity clone is tested against different known clones, in a blocking experiment, to identify whether they recognize completely overlapping (++), partially overlapping (+), or completely different epitopes (-). In a blocking experiment, cells are incubated with an excess of purified unconjugated REAfinity clone followed by staining with conjugated form of the other known clones (website).
 streptavidin Qdot605 (detection of KIR2DL3)- Q605 Flow cytometry. Human peripheral blood lymphocytes used for titration.
 Granulysin - PE Flow cytometry. Human peripheral blood and decidual NK cells used for titration.
 CD56-PE-Dazzle Flow cytometry. Human peripheral blood and decidual NK cells used for titration.
 GzmA - PE-Cy7 Flow cytometry. Human peripheral blood and decidual NK cells used for titration.
 CD49a-BV421 Flow cytometry (Qualified) (website)
 CD14- BV605 Human (QC Testing). Flow cytometric analysis of CD14 expression on human peripheral blood monocytes (website)
 CD19-BV605 Human (Tested in Development) (website)
 CD20-BV605 Human (Tested in Development) (website)
 CD103-PerCP-Cy5.5 Flow cytometry (Quality tested) (website)
 KIR2DL1 - PeVio770 REAfinity clone is tested against different known clones, in a blocking experiment, to identify whether they recognize completely overlapping (++), partially overlapping (+), or completely different epitopes (-). In a blocking experiment, cells are incubated with an excess of purified unconjugated REAfinity clone followed by staining with conjugated form of the other known clones (website).
 CD18 (ITGB2)- APC Flow cytometry (Quality tested) (website)
 CD39 -APC Cy7 Flow cytometry (Quality tested) (website)

Human research participants

Policy information about [studies involving human research participants](#)

Population characteristics

Fetal, decidual samples and peripheral blood samples were collected from woman undergoing elective terminations. All participants in the study were healthy pregnant woman (6-14 gestational weeks) without any exclusion.

Recruitment

Samples were taken in UK. Ethnicity was not recorded but is expected to be primary caucasian. This is not expected to affect the composition of cells in the maternal–fetal interface during early pregnancy.
 All tissue samples used for this study were obtained with written informed consent from all participants in accordance with the guidelines in The Declaration of Helsinki 2000 from multiple centres.
 Human embryo, fetal and decidual samples were obtained from the MRC/WellcomeTrust funded Human Developmental Biology Resource (HDBR36, <http://www.hnbr.org>) with appropriate maternal written consent and approval from the Newcastle and North Tyneside NHS Health Authority Joint Ethics Committee (08/H0906/21+5). HDBR is regulated by the UK Human Tissue Authority (HTA; www.hta.gov.uk) and operates in accordance with the relevant HTA Codes of Practice. Decidual tissue for smFISH (Extended Data Figure 7c-d) was also covered by this ethics.
 Peripheral blood from woman undergoing elective terminations were under appropriate maternal written consent and approvals from the Newcastle Academic Health Partners (reference NAHPB-093) and HRA NHS Research Ethics committee North-East- Newcastle North Tyneside 1 (REC reference 12/NE/0395)
 Decidual tissue for immunohistochemistry (Figure 3b,c and Extended Data Figure 9c) were obtained from elective terminations of normal pregnancies at Addenbrooke's Hospital between 6 and 12 weeks gestation, under ethical approval from the Cambridge Local Research Ethics Committee (04/Q0108/23).
 Decidual tissue for smFISH (Figure 3d and Extended Data Figure 6b and Extended Data Figure 7b) were obtained from the Newcastle Uteroplacental Tissue Bank and Ethics numbers are Newcastle and North Tyneside Research Ethics Committee 1 Ref:10/H0906/71 and 16/NE/0167.

Flow Cytometry

Plots

Confirm that:

- The axis labels state the marker and fluorochrome used (e.g. CD4-FITC).
- The axis scales are clearly visible. Include numbers along axes only for bottom left plot of group (a 'group' is an analysis of identical markers).
- All plots are contour plots with outliers or pseudocolor plots.
- A numerical value for number of cells or percentage (with statistics) is provided.

Methodology

Sample preparation

Decidual and blood cells were incubated at 4°C with 2.5ul of antibodies in 1% FBS in DPBS without Calcium and Magnesium (ThermoFisher Scientific, 14190136). DAPI was used for live/dead discrimination.
 For intracellular staining of granule proteins, dNK were surface stained for 30 mins in FACS buffer with antibodies. Cells were

	washed with FACS buffer followed by staining with dead cell marker (DCM Aqua) and strepavidinQ605. dNK were then treated with FIX & PERM (Thermofisher) and stained for granule proteins.
Instrument	Becton Dickinson (BD) FACS Aria Fusion. For granule experiment we used LSRFortessa FACS analyser (BD Biosciences)
Software	Becton Dickinson (BD) FACS Aria Fusion was controlled using BD FACS DIVA software (version 7) and FlowJo v10.3 was used for analysis.
Cell population abundance	<i>Describe the abundance of the relevant cell populations within post-sort fractions, providing details on the purity of the samples and how it was determined.</i>
Gating strategy	<p>Gating strategy for a panel of 14 antibodies to analyse immune cells in decidual samples by SS2 (CD3, CD4, CD8, CD9, CD14, CD16, CD19, CD20, CD34, CD45, CD56, CD94, DAPI, HLA-DR, HLA-G). Cells isolated for SS2 data were gated on: live; CD19/20-ve, singlets, and the following cell types sorted: i) CD45+, HLA-DR++; ii) CD45+, HLA-DR+; iii) CD45+, HLA-DR-, CD56-, CD3+, CD4+; CD8- iv) CD45+, HLA-DR-, CD56-, CD3+, CD8+; v) CD45+, HLA-DR-, CD56-, CD3+, CD4-, CD8-; vi) CD45+, HLA-DR-, CD3-, CD56-, CD94- (all -); vii) CD45+, HLA-DR-, CD3-, CD56+, CD94-; viii) CD45+, HLA-DR-, CD3, CD56+, CD94+, CD9-; ix) CD45+, HLA-DR-, CD3, CD56+, CD94+, CD9+; x) CD45-, HLA-G+; xi) CD45-, HLA-G-.</p> <p>For the isolation of the three dNK subsets, dNK cells were gated on live, single-cell, LIN- (CD3, CD14, CD19, CD20), CD56+, CD16-, CD49a+. dNK3 were additionally gated on CD103 and ITGB2. dNK1 were additionally gated on CD39 and ITGB2. dNK2 were additionally gated on CD103 and ITGB2.</p> <p>For the detection of granule molecules dNK were gated as CD3-CD14-CD19-, live cells then CD56+NKG2A+ and then KIR+ and KIR- subsets generated using Boolean functions with the gates for all the different KIRs stained (KIR+), and its inverse gate (KIR-).</p>

Tick this box to confirm that a figure exemplifying the gating strategy is provided in the Supplementary Information.